学位論文

U-based itinerant ferromagnets investigated by field-angle-resolved measurements

(磁場角度回転実験によるウラン系遍歴強磁性体の研究)

平成29年12月博士（理学）申請

東京大学大学院理学系研究科
物理学専攻

中村　翔太

Abstract

The itinerant ferromagnet URhGe is well known to be a ferromagnetic superconductor, in which ferromagnetism and superconductivity coexist. Ferromagnetism in URhGe is unique in that the Curie temperature can be tuned to zero by applying a magnetic field along the b axis, perpendicular to the easy c axis. In particular, this compound has attracted much interest because it shows a re-entrant superconductivity (RSC) in high magnetic field of $\mu_0 H \sim 12$ T, which is much higher than the Pauli limit ($\sim$ 1 T in URhGe), when a magnetic field is applied along the b axis. A first-order spin-reorientation transition occurs near RSC in URhGe, and the nature of the transition changes form a first-order transition to a second-order transition at a tricritical point (TCP) with increasing temperature. The position of TCP is under substantial debate in this system, because magnetic fluctuations near TCP associated with the moment reorientation are expected to play an essential role in RSC.

In order to determine the position of TCP, we have performed an experimental study of the wing structure (first-order transition plane) of URhGe in three-dimensional H_c- H_b-T phase diagram by means of dc magnetization, specific heat and magneto-caloric effect (MCE) measurements at low temperatures, where H_c and H_b are magnetic fields applied along the c and b axes of URhGe. Beginning at TCP in the three-dimensional phase diagram, the wing structure appears in a narrow field-angle range near the b axis. Owing to a strong magnetic anisotropy of URhGe, field-angle resolved in-situ measurements are needed to determine the position of TCP and to investigate the details of the wing structure. In order to perform field-angle resolved in-situ measurements, two-axis rotation device, which can work at low temperature, has been developed. The detail of the device is shown in Chapter 3. The main results of these measurements are summarized in Chapters 5 and 6. The theoretical and experimental backgrounds are introduced in Chapter 1.

Experimental methods used in the present work are described in Chapters 2. Dc magnetization and magnetic torque measurements have been performed by means

of a capacitively-detected Faraday-force method. Specific heat has been measured by standard relaxation method, and MCE has been obtained by the change of the sample temperature with increasing-field and decreasing-field sweeps. After the explanation of the principle of the method, newly developed magnetometer and specific-heat cell are introduced. These cell have been developed to reduce torque contribution and mis-alignment of the magnetic-field-angle.

In Chapter 3, the details of the newly-developed two-axis rotation device are described. The orientation of the sample is precisely controlled within an accuracy of less than 0.01° using the device. The device consists of a piezo-stepper-driven goniometer (ϕ rotation) and a home-made tilting stage (θ rotation). The available angle ranges are $-3^\circ \leq \phi \leq 3^\circ$ and $-10^\circ \leq \theta \leq 10^\circ$, where the ϕ and θ axes are perpendicular to each other. The capacitive transducer and the specific heat cell can be mounted on a stage of the piezo-stepper-driven goniometer. The device allows us to perform high-precision angle resolved measurements. It is expected to greatly contribute to a clarification of strange phenomena in heavy electron systems, which usually have strong anisotropy. Chapter 4 deals with the performance evaluation of the two-axis rotation device by measuring angular dependences of a metamagnetic transition of $CeRu_2Si_2$ by means of dc magnetization measurements.

In Chapter 5, we have examined high-precision angle-resolved dc magnetization and magnetic torque studies on a single-crystalline sample of URhGe. This material is an orthorhombic Ising ferromagnet with the c axis being the magnetization easy axis, and this measurements have performed in order to investigate the phase diagram around the ferromagnetic (FM) spin-reorientation transition in a magnetic field near the b axis. We have clearly observed first-order transition in both the magnetization and the magnetic torque at low temperatures, and determined detailed profiles of the wing structure of the three-dimensional T-H_b-H_c phase diagram, where H_c and H_b are the field components along the c and the b axes, respectively. The positions of quantum wing critical points are at $\mu_0 H_c \sim \pm 1.1$ T and $\mu_0 H_b \sim 13.5$ T. Two second-order transition lines at the boundaries of the wing structure rapidly tend to approach with each other with increasing temperature up to $\sim$ 3 K. Just at the zero conjugate field ($H_c = 0$), however, a signature of the first-order transition can still be seen in the field derivative of the magnetization at $\sim$ 4 K, indicating that TCP locates in a rather high temperature region above 4 K. This feature of the wing plane structure is consistent with the theoretical expectation that three second-order transition lines merge tangentially at TCP.

In Chapter 6, angle-resolved specific heat and magneto-caloric effect measurements in URhGe have been performed, in order to decide the location of TCP and

investigate the wing structure in other thermodynamic quantity measurement. A feature of the first order transition is observed in the temperature range up to 2-3 K by MCE measurements in a magnetic field applied along the *b* axis. The critical field of the transition obtained by MCE is almost the same as the ones decided by present magnetization and specific-heat measurements. The result of MCE measurements supports the conclusion that TCP locates above 4 K.

Contents

Abstract **i**

1 Introduction **1**

1.1 Quantum Phase Transition 1

1.2 Ising ferromagnet in a transverse magnetic field 2

1.3 Wing structure and tricritical point 3

1.4 Ferromagnetic superconductors 7

1.5 Purpose of the present work 9

2 Experimental methods **11**

2.1 Magnetization measurements 11

2.1.1 Capacitively-detected Faraday method 11

2.1.2 Improvement of the capacitive transducer reducing the torque contribution 15

2.1.3 Thermometer for magnetization measurements 17

2.2 Heat capacity and magneto-caloric effect measurements 18

2.2.1 Method of specific heat measurements 18

2.2.2 Method of magneto-caloric effect measurements 21

2.2.3 newly-developed specific-heat cell for measurements of a high-torque sample 24

2.2.4 Thermometer for specific heat measurements 24

3 Development of a two-axis rotation device **25**

3.1 Introduction 25

3.2 The schematic view of the Device 26

3.3 Mechanical issues of the magnetization measurements with two-axis rotation device 29

3.3.1 Influence of tiling transducer on the sensitivity 29

3.3.2 Misalignment of the magnetic field caused by the application of a field gradient . . . 29

4 Performance evaluation of the newly developed rotation device 31
4.1 Introduction for $CeRu_2Si_2$ . . . 31
4.2 Motivation . . . 34
4.3 Experimental Procedure . . . 35
4.4 Results and Discussion . . . 36
4.4.1 Adjustment of angles . . . 36
4.4.2 Magnetization of $CeRu_2Si_2$ in magnetic field along the [001] direction with in-situ alignment . . . 42
4.5 Summary of the performance evaluation . . . 44

5 Magnetization measurements in URhGe 45
5.1 Introduction of URhGe . . . 45
5.2 Experimental Procedures . . . 50
5.3 Results . . . 54
5.3.1 Torque component . . . 54
5.3.2 Magnetization . . . 57
5.4 Discussion . . . 63
5.5 Summary . . . 69

6 Specific heat and magneto-caloric effect measurements in URhGe 71
6.1 Motivation . . . 71
6.2 Experimental procedure . . . 71
6.3 Results and Discussion . . . 73
6.3.1 adjustment of magnetic filed angle . . . 73
6.3.2 specific heat and magneto-caloric effect measurements . . . 75
6.4 Summary . . . 82

7 Conclusion 83

Appendix 84

A 85
A.1 Temperature variation of the magnetization curves of URhGe at several θ . . . 85

A.2 Angular θ variation of the magnetization curves of URhGe at several temperature 88
A.3 Angular θ variation of the magneto-caloric effect of URhGe at several temperature 92

B **99**
B.1 Gnuplot source code for simulating the sample temperature change in magneto-caloric effect measurements 99

Publications **105**

References **107**

Bibliography **107**

Acknowledgments **113**

Chapter 1

Introduction

1.1 Quantum Phase Transition

A quantum phase transition has attracted a lot of interest because it drives various anomalous behaviors in observable physical quantities. The quantum phase transition is a transition, which occurs at zero temperature, and the critical point of the transition is a quantum critical point (QCP). When a control parameter, e.g. magnetic field and pressure etc., is applied, a quantum phase transition is often induced. Generally, fluctuation becomes larger near the critical point of a second order transition, and quantum fluctuations increase near QCP. Figure 1.1 shows an example of the temperature vs. control parameter phase diagram of a quantum phase transition. Anomalous behaviors, i.e. non-Fermi liquid, unconventional superconductivity (SC) etc., are observed near QCP and quantum critical regime, which is located between ordered and disordered phases.

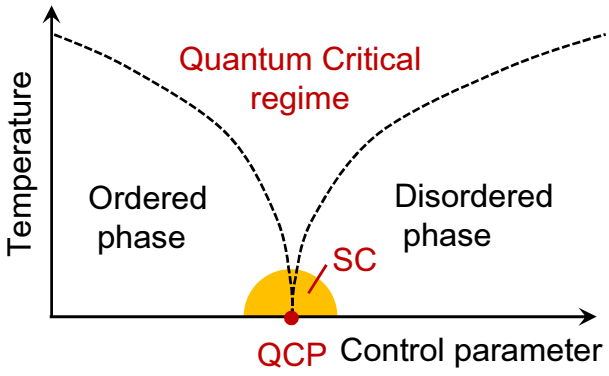

Figure 1.1: An example of temperature vs. control parameter phase diagram of quantum phase transition.

1.2 Ising ferromagnet in a transverse magnetic field

The transverse Ising model, which is an Ising model in a transverse magnetic field, is one of the most extensively studied quantum model [1–4]. The Hamiltonian of this model is written as

$$\mathscr{H} = -\sum_{<i,j>} J_{i,j}\sigma_i^z\sigma_j^z - \Gamma\sum_i \sigma_i^x, \tag{1.1}$$

where σ_i^z, etc., are Pauli spin operators, Γ indicates a transverse field, and $J_{i,j}$ is a coupling between neighboring spins (σ_i^z and σ_j^z). The sum $\sum_{<i,j>}$ is taken over the neighboring pairs. The first term of the Hamiltonian denotes the ferromagnetic interaction between neighboring spins ($J_{i,j} = J > 0$) for two- or three- dimensional lattices, where the easy axis is the z axis. The second term is the effect of the transverse field, by which the spins are aligned towards the transverse field, and the ferromagnetic order is forced to vanish. The ferromagnetic (FM) phase transition remains at a finite temperature, if the transverse field is smaller than the critical field $H_{\rm R}$. The schematic view of a quantum FM transition in the transverse Ising model is shown in Fig. 1.2. $T_{\rm Curie}$ can be tuned to zero by applying a transverse field H. The order parameter is the component of the magnetic moment along the easy axis (magnetization $M \perp H$), and the magnetic moment reorients along the field direction ($M \parallel H$) above the critical field $H_{\rm R}$; the FM quantum phase transition is called "spin reorientation".

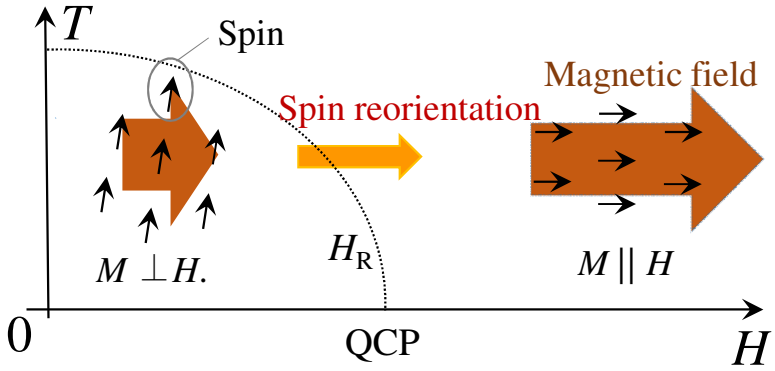

Figure 1.2: Schematic view of a quantum FM transition of Ising ferromagnet in a transverse magnetic field. The order parameter is the component of the magnetic moment along the easy axis (magnetization $M \perp H$), and the magnetic moment reorients along the field direction ($M \parallel H$) above the critical field $H_{\rm R}$; the FM quantum phase transition is called "spin reorientation".

1.3 Wing structure and tricritical point

A paramagnetic-ferromagnetic phase transition is an example of a second order phase transition in a textbook [5, 6]. However, suppressing the transition with a tuning parameter such as pressure in clean metals, the transition often becomes of first order at a tricritical point (TCP) at T_{TCP} and p_{TCP} in three dimensional T-p-H phase diagram, where H is applied along the easy axis of the magnetization [7]. A schematic view of a typical T-p-H phase diagram is shown in Fig. 1.3 [8]. The regions of ferromagnetic (FM) and paramagnetic (PM) phases are shown in this figure. The diagram also indicates the tricritical point (TCP), the quantum phase transition lines (QPT), and two quantum wing critical points (QWCPs). First order transitions occur on dashed lines and blue plates. The edges of the wing planes are second-order transition lines (red solid lines), terminating at $T = 0$ in the quantum wing critical points (QWCPs). The first order planes are symmetric with respect to $H \rightarrow -H$, so they are called "wing structure". Such a three dimensional phase diagram with the wing structure is presented schematically in phenomenological theory [7, 9–12]. Recently, the detailed profiles of the wing structure is predicted by theories as follows.

1. There is an infinite slope of the first order transition at $T = 0$ and $H = 0$ [11].

2. The wing structure is tilted in the direction of the disordered phases and is not perpendicular to the p axis [11].

3. All the transition lines merging at a TCP are tangent, implying that three second order transition lines, including the edge of the wing structure meet at TCP tangentially [8].

4. The wing structure is theoretically predicted in clean metals [10].

Figure 1.4 is schematic projections of the temperature-pressure-magnetic field (T-p-H) phase diagram on the T-p($H = 0$), H-p ($T = 0$), and T-H ($p = 0$) planes. These projections and the diagram in Fig. 1.3 satisfy the profiles 1-3. Note that the first order transition becomes a crossover in $H > H_{\mathrm{QWCP}}$, which is the outside of the wing structure.

The effect of a disorder on the wing structure has been discussed theoretically [13]. With increasing the disorder, the tricritical temperature decreases, the wing

structure shrink, and finally, a QCP is realized in zero field. When the order parameter of the transition couples to the soft mode, the disorder corresponds to a diffusion of soft mode. Figure 1.5 shows an evolution of the phase diagram of metallic quantum ferromagnet in temperature-magnetic field-control parameter (T-h-r) space with increasing disorder. Note that a pressure is the control parameter in Fig. 1.3.

Wing structure with pressure p as a tuning parameter has been experimentally determined in itinerant FM compounds, such as UGe_2 [14–16], $ZrZn_2$ [17, 18], URhAl [19], UCoGa [20], $Sr_3Ru_2O_7$ [21], CoS_2 [22], MnSi [23], and an itinerant metamagnet UCoAl [24]. In these systems, however, either high pressure (UGe_2, $ZrZn_2$, URhAl, UCoGa etc.) or negative pressure (UCoAl) is required to tune T_C to zero, making it difficult to examine the magnetization behavior near QPT. Two examples of the three dimensional phase diagram are given below. Figure 1.6 shows phase diagram of UGe_2, in which wing structure is observed in T-p-H space [14]. Gray planes are planes of first order transition, and solid (red) lines are second order lines in Fig. 1.6(b). Fig. 1.7 is the T-p-H phase diagram of $Sr_3Ru_2O_7$. In contrast to these examples, as a magnetic field H_b parallel to the b axis being the tuning parameter, URhGe provides a good opportunity to investigate the whole FM phase diagram by various means (see introduction of Chapter 5).

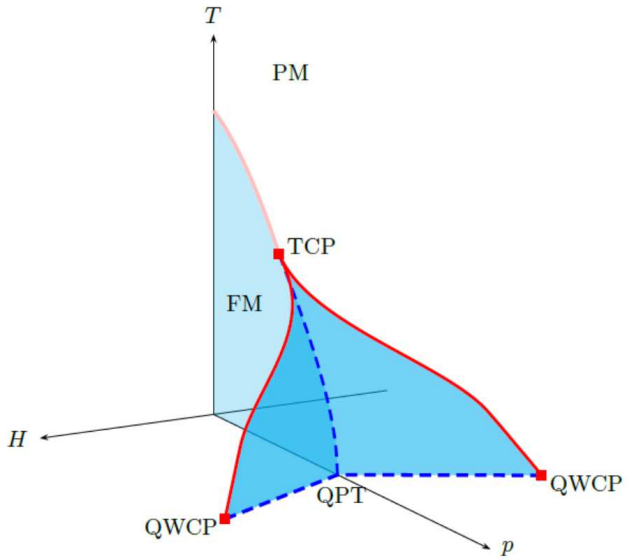

Figure 1.3: Schematic view of a typical T-p-H phase diagram, where H is applied along the easy axis of magnetization. [8]

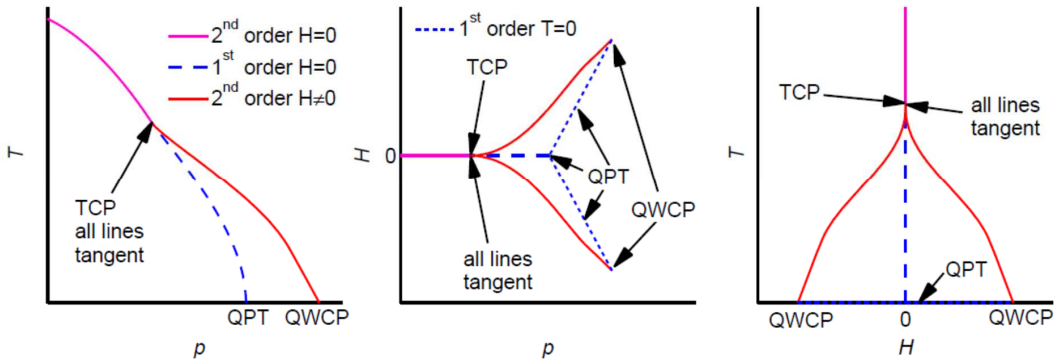

Figure 1.4: Schematic projections of the T-p-H phase diagram in the T-$p(H = 0)$, H-p ($T = 0$), and T-H ($p = 0$) planes [8].

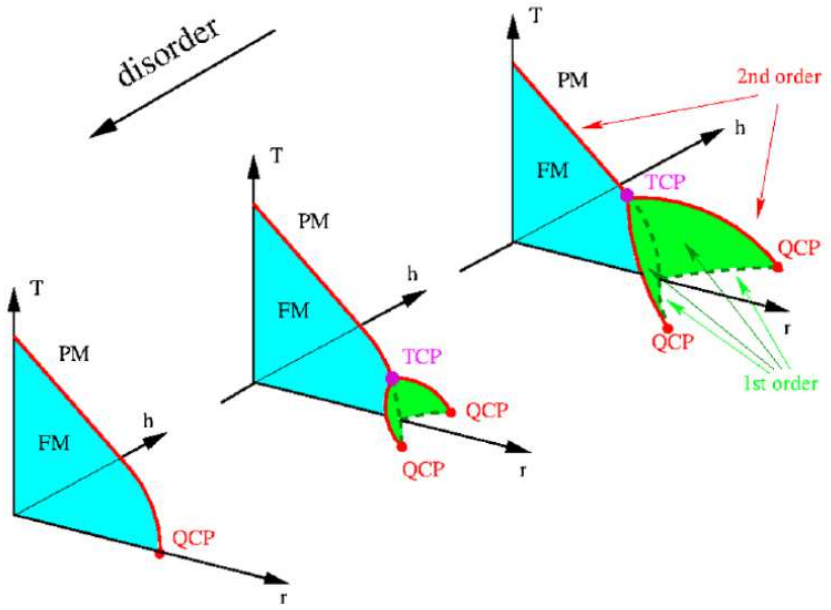

Figure 1.5: An evolution of the phase diagram of metallic quantum ferromagnet in temperature-magnetic field-control parameter (T-h-r) space with increasing disorder [13].

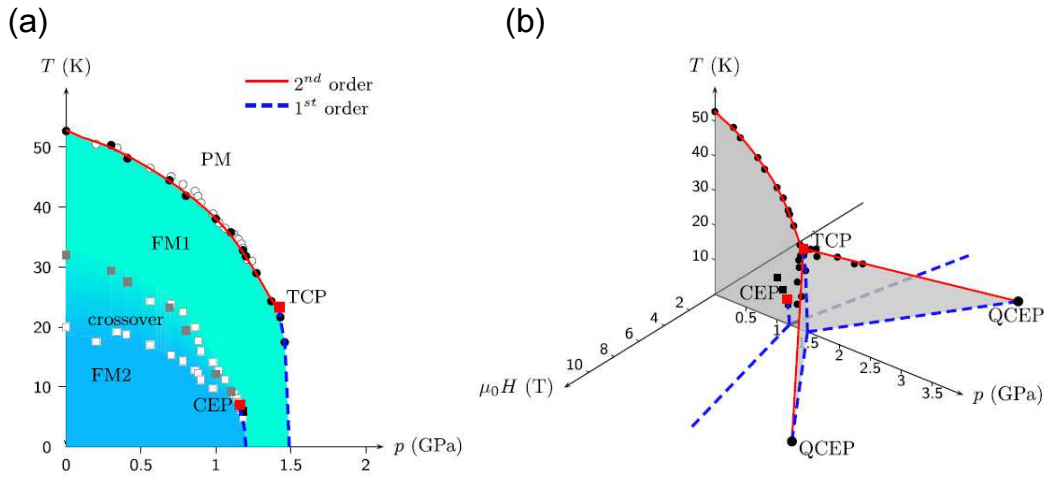

Figure 1.6: (a) T-p phase diagram of UGe_2. A tricritical point locates at $p \sim 1.5$ GPa and $T \sim 23$ K. (b) T-p-H phase diagram of UGe_2 from Ref. [14]. Gray planes are planes of first order transition, and solid (red) lines are second order lines in Fig. 1.6(b).

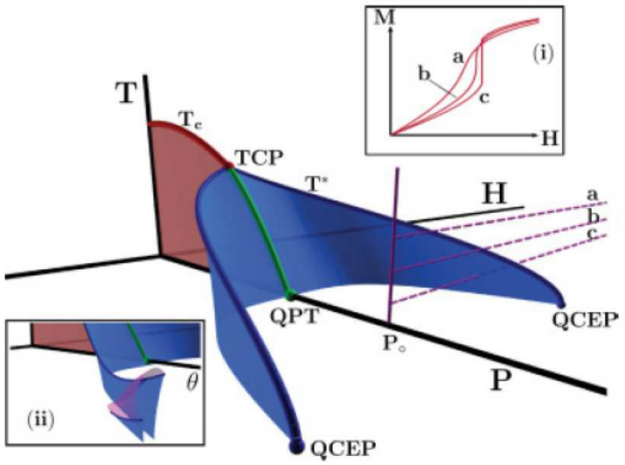

Figure 1.7: Main figure: T-p-H phase diagram of $Sr_3Ru_2O_7$ [21]. At wing plane, a magnetization jumps discontinuously [inset(i)]. In this material, QCEP, which is the terminal of the edge of the wing structure at $T = 0$ K, does not appear instead of a nematic phase, and the edge is tuned by a field-angle θ [inset (ii)].

1.4 Ferromagnetic superconductors

The coexistence of ferromegnetism and superconductivity (SC) have been studied both in theory and experiment since 1950's. Ferromagnetism had been thought to compete with SC, because a large internal magnetic field easily destroys the Cooper pairs of ordinary superconductivity. Actually, $(Ce_{1-x}Gd_x)Ru_2$, $RuSr_2GdCu_2O_8$, $ErRh_4B_4$, and $HoMo_6S_8$ were known as ferromagnetic (FM) superconductors [25–28], but electrons causing SC are different in orbits and atoms from those playing a role of FM in these systems.

Meanwhile, a result overturning the conventional wisdom was reported by the group of Cambridge University in 2000. They claimed that UGe_2, which is a ferromagnet below 50 K, becomes superconducting by applying pressure at 0.8 K while maintaining the ferromagnetic state. The discovery of the uranium-based FM superconductor UGe_2 have had a great impact [29], because the origin of ferromagnetism and superconductivity is thought to be due to the same 5f electrons of uranium in this material. Up to now, uranium-based FM superconductors URhGe [30] and UCoGe [31] have been newly discovered, and these compounds exhibit superconductivity in the FM state at an ambient pressure. Interestingly, the crystal structure of the three FM superconductors have a zigzag chain of uranium atoms.

The superconducting properties in the above three uranium-based superconductors are extremely extraordinary, such as the microscopic coexistence of superconductivity and ferromagnetism [32–35], possible occurrence of an odd-parity pairing [29–31], the huge enhancement of H_{c2} exceeding the Pauli-limiting field in UGe_2 [36] and UCoGe [31, 37], and re-entrant superconductivity (RSC) in URhGe [38]. These anomalous behavior appear around FM quantum phase transition, and hence magnetic quantum fluctuations are considered to be responsible for the emergence of such unusual superconducting states [32, 39, 40]. Figure 1.8 shows the field-temperature phase diagrams of these three uranium compounds [41]. The H_{c2} curve displays unusual S-shape in UGe_2, when the magnetic field along the magnetization easy a axis and a hydrostatic pressure of 1.35 GPa are applied. With increasing field, the ground state is switched from FM1 to FM2 phases, and the S-shape of H_{c2} is due to this switching. The value of H_{c2} at 0 K exceeds the Pauli limiting field expected by T_{SC} at zero field, $H_P(T = 0) = 1.854T_{SC}(H = 0)$, on basis with the weak coupling scheme with $g = 2$, suggesting the spin triplet state. Similar huge enhancements of H_{c2},unusual S-shape of H_{c2} and field-reentrant superconductivity (RSC), are also observed in UCoGe and URhGe.

Figure 1.9 shows the H-T phase diagram of URhGe and UCoGe, together with

$T_{\mathrm{Curie}}(H)$ [41]. T_{Curie} is suppressed with the transverse field, where the field is applied perpendicular to the magnetization easy axis (see Section 1.2). In URhGe, RSC appears between $\sim$ 9 and $\sim$ 13.5 T, near $T_{\mathrm{Curie}}(H)$. Surprisingly, the critical temperature of RSC ($\sim$ 0.4 K at 12.5 T) is higher than the transition temperature at zero field, suggesting that the superconductivity in URhGe is reinforced by the magnetic field along the *b* axis. A similar behavior, S-shape of H_{c2}, is observed in UCoGe.

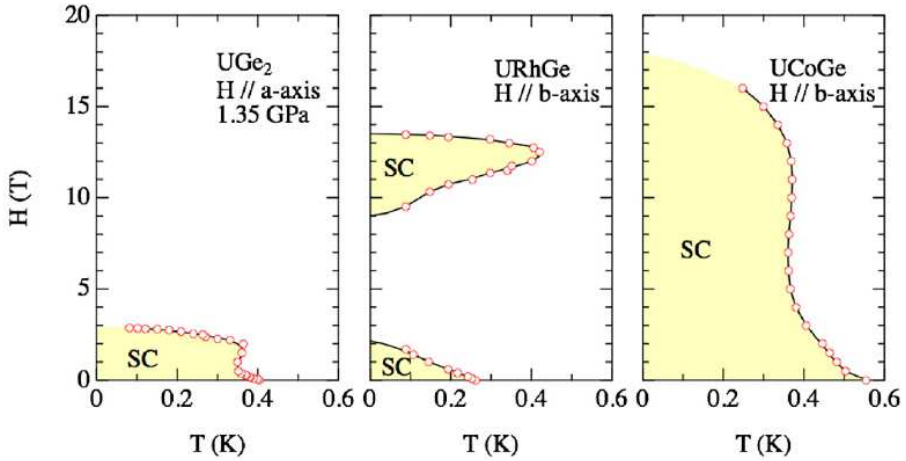

Figure 1.8: *H-T* phase diagram of UGe_2, URhGe, and UCoGe. The magnetic field is applied along the magnetization easy *a* axis in UGe_2, but the field direction is parallel to the *b* axis, which is not the easy axis, in URhGe, and UCoGe [41].

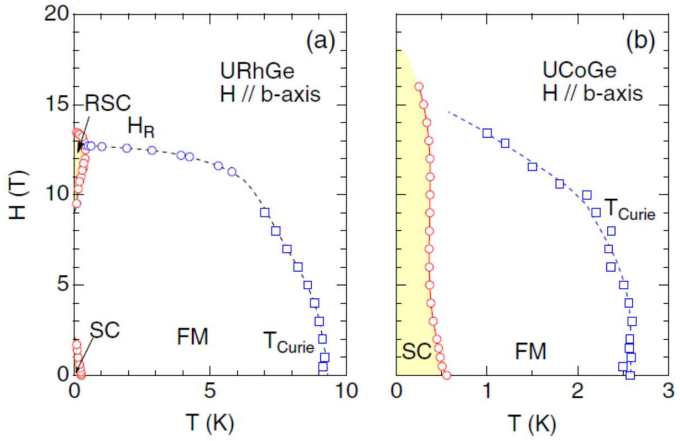

Figure 1.9: *H-T* phase diagram of URhGe and UCoGe, together with T_{Curie} [41].

1.5 Purpose of the present work

Whereas much theoretical work has been conducted, experiments on a wing structure phase diagram have so far been performed to much less extent because a high pressure is normally required to access a ferromagnetic (FM) quantum phase transition. By contrast, as a magnetic field perpendicular to the magnetic easy axis being the tuning parameter, URhGe provides a good opportunity to investigate the whole FM phase diagram, in particular the wing structure as well as TCP. In this dissertation, an experimental study of the wing structure (first-order transition plane) of the itinerant ferromagnet URhGe in the H_c- H_b-T three-dimensional phase diagram has been performed by means of dc magnetization, magnetic torque, specific heat and magneto-caloric effect (MCE) measurements at low temperatures, where H_c and H_b are magnetic fields applied along the c and b axes of URhGe. The purpose of the present work is to directly investigate the details of the wing structure close to the tricritical point (TCP) in the three dimensional phase diagram with in-situ high-precision alignment of the magnetic field, which could be of relevance to the mechanism of the reentrant superconductivity (RSC). As described in the introduction of Chapter 5, the region of the wing structure, on which magnetic fluctuations are enhanced, is well coincides with the region of RSC [39]. A possible explanation is that the fluctuations associated with a quantum TCP may play an essential role of RSC in URhGe [38]. In this scenario, TCP is needed to locate at lower temperature near RSC. The position of TCP has been, however, controversial [42, 43]. We plan to observe the wing structure precisely, and determine the location of TCP. The main results of these measurements are summarized in Chapters 5 and 6.

In order to investigate the wing structure of URhGe, two-axis rotation device, which can work at low temperatures, has been developed. The detail of the device is shown in Chapter 3. Dc magnetization measurement has been performed by means of capacitively-detected Faraday method, and experimental methods used in the present work are described in Chapter 2. The device allows us to perform in-situ angle resolved measurements, and it is expected to greatly contribute to the elucidation of physics in heavy electron systems, which generally have strong anisotropy. In Chapter 4, we have checked the performance of the two-axis rotation device by measuring the angular dependence of the dc magnetization curves of $CeRu_2Si_2$, the heavy fermion system that shows a metamagnetic crossover in a [001] magnetic field.

Chapter 2

Experimental methods

2.1 Magnetization measurements

2.1.1 Capacitively-detected Faraday method

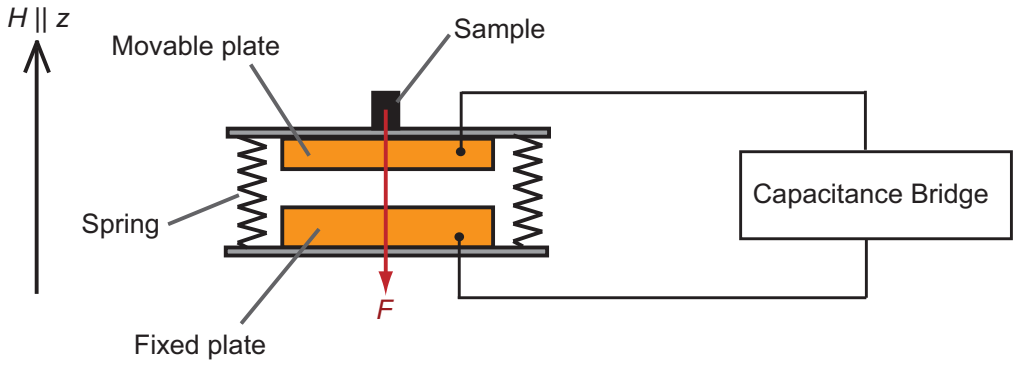

Figure 2.1: Principle of the magnetization measurement. The magnetic force $\boldsymbol{F}$ exerted on a sample situated in an inhomogeneous field is detected as a capacitance change of parallel-plate variable capacitor, whose movable plate is suspended by elastic springs.

Dc magnetization in high magnetic fields was measured by means of capacitively-detected Faraday method [44]. Compared with the usual dc magnetization measurement mothod using superconducting quantum interference device (SQUID), this method is well known as one of the best method for the dc magnetization measurements at very low temperature since the capacitance measurement produces no heat. Moreover, since the capacitance measurement is not affected by a magnetic field, this method is suitable for high-sensitive magnetization measurements even

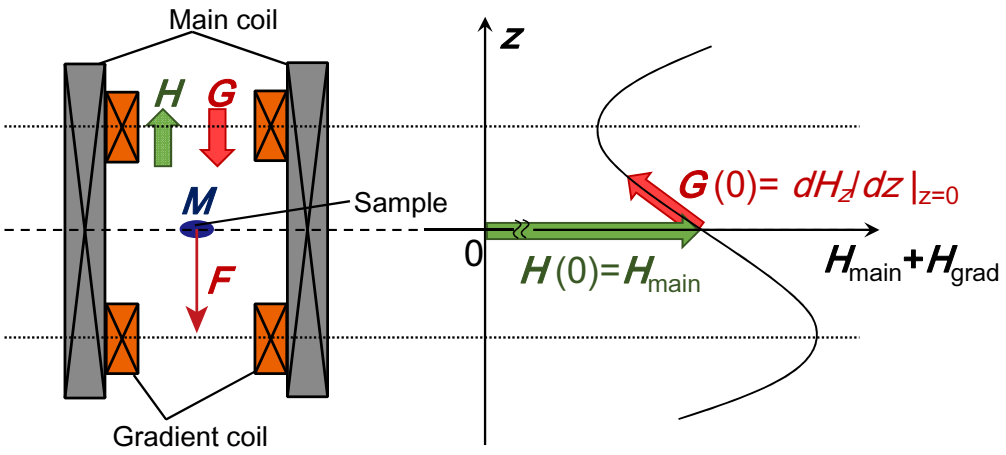

Figure 2.2: Schematic of a superconducting magnet for a capacitively-detected Faraday method. H_{main} is a magnetic field of main coil, and H_{grad}, which produces the field gradient G, is that from a set of gradient coils.

at very high fields. In a Faraday method, the magnetization $\boldsymbol{M}$ of a sample can be obtained by measuring the force caused by $\boldsymbol{M}$. When $\boldsymbol{M}$ of the sample is placed in an inhomogeneous magnetic field $\boldsymbol{H}$, the force is

$$\boldsymbol{F} = (\boldsymbol{M} \cdot \boldsymbol{\nabla})\boldsymbol{H}, \tag{2.1}$$

which is proportional to the magnetization of the sample. Figure 2.1 schematically shows the principle of the magnetization measurement. The magnetometer is made of a parallel-plate variable capacitor, whose movable plate is suspended by elastic springs. The sample is mounted on the movable plate, and is electrically insulated from the plate. The movable plate is moved by $\boldsymbol{F}$ until the restoring force of the springs balances with $\boldsymbol{F}$. The restoring force of the spring is proportional to the displacement of plate, and $\boldsymbol{F}$ can be detected as a capacitance change ΔC.

The magnetic field is generated by a main solenoid coil and a set of field gradient coils. Figure 2.2 shows the schematic view of the main coil and the gradient coils together with the sample. The main coil produces magnetic fields $\boldsymbol{H}_{\mathrm{main}}$ up to 17 T, and the gradient coils, which are mounted inside the mail coil, can provide a vertical gradient field $\boldsymbol{G}$ up to 10 T/m. The power supply for the gradient coils are independent from the one of the main coil. When the sample is located at the symmetry center $z = 0$ of the main coil and the gradient coils, the magnetic force F will be expressed as

$$F = MG, \tag{2.2}$$

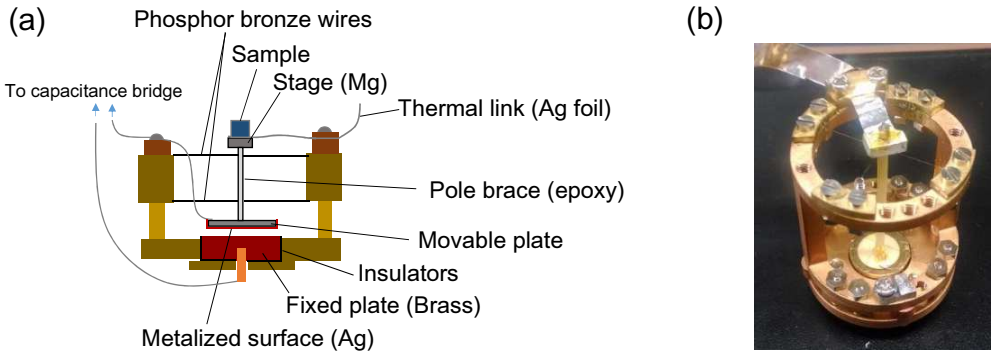

Figure 2.3: (a) A cross-sectional view of a capacitive transducer. The movable plate is suspended by four phosphor bronze wires, which are spanned from orthogonal directions in a horizontal plane. (b) A photo of the capacitive transducer used in the magnetization measurements of URhGe.

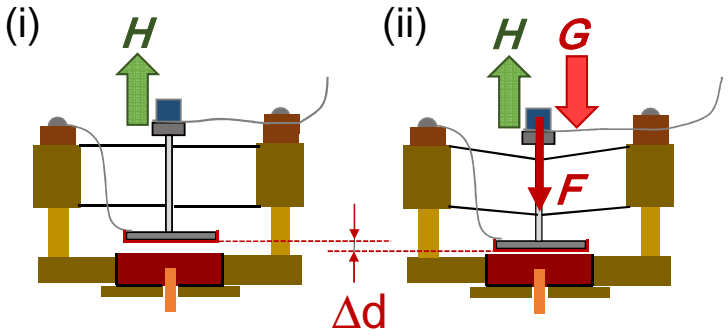

Figure 2.4: A change of the gap Δd between fixed and movable electrodes in the magnetometer with (i) zero and (ii) a finite gradient of the magnetic field.

assuming that $M_z \sim M$ is much larger than M_r, and neglecting terms proportional to $\frac{\partial H_z}{\partial r}$, where r denotes the lateral direction perpendicular to the z axis.

Figure 2.3(a) shows a cross-sectional view of a capacitive transducer, which transforms the magnetic force F into a change of the capacitance C. A photo of the capacitive transducer using in the magnetization measurements of URhGe (Chapter 5) is given in Fig. 2.3(b). A movable plate is attached at the bottom of a pole brace hung by the crossed wires, and can be moved in proportion to an applied force. The fixed plate is isolated from the surrounding part. The sample is mounted on the top of the pole brace, which is thermally linked by a silver foil with a mixing chamber of a refrigerator.

Magnetization of the sample is measured by the following two steps in the capacitively-detected Faraday method.

1. Measure the capacitance with zero gradient field, $C_{G=0}$, as schematically shown in Fig. 2.4(i). In this case, the force of the gravitational weight and a magnetic torque $\boldsymbol{\tau} = M \times H$ of the sample is dominant in the signal of the capacitance.

2. Measure the capacitance with a finite gradient field, $C_{G\neq 0}$, as schematically shown in Fig. 2.4(ii). In this case, not only the forces in case 1 but also the magnetic force (Eq. 2.2) contributes to a change in the capacitance. Note that the output also includes the magnetization of the movable plate, pole brace, and the stage (M_{bg}).

Using these measured capacitance data, a change of the gap of electrodes Δd shown in Fig. 2.4 can be expressed as

$$\Delta d = \varepsilon_0 S \left(\frac{1}{C_{G=0}} - \frac{1}{C_{G\neq 0}} \right), \tag{2.3}$$

where ε_0 is the permittivity of vacuum, and S is the area of electrode of capacitance. When the spring constant of the wires is defined as k, the balance of the forces is expressed by the following equation.

$$(M + M_{\mathrm{bg}})G = k\Delta d. \tag{2.4}$$

Finally, the magnetization of the sample can be obtained by Eqs. 2.3 and 2.4 as follows.

$$M = \frac{\varepsilon_0 k S}{G} \left(\frac{1}{C_{G=0}} - \frac{1}{C_{G\neq 0}} \right) - M_{\mathrm{bg}}. \tag{2.5}$$

M_{bg} can be given by an independent measurement without the sample. The value of the spring constant k, which is of order $1 \times 10^5 dyn/cm$, is estimated by a dc bias method; an electrostatic force $C^2 {V_{\mathrm{bias}}}^2/(2\varepsilon_0 S)$ can be induced to the electrodes by applying a dc bias voltage of $V_{\mathrm{bias}} = 30 - 50$ V, and k is calculated by an equation of the barance of the electrostatic force and the restoring force of the spring. More accurate magnetization value can be calibrated by comparing the measured data at a certain temperature, e.g., the liquid-helium temperature 4.2 K, with those obtained by a reference magnetometer such as MPMS, a SQUID. Figure 2.5 shows an example of the data processing, in which the raw capacitance (C) data of $CeRu_2Si_2$ obtained at 0.12 K in magnetic fields along the [001] axis, with the field gradient $G = 0$ and 2 T/m. The magnetization curve (solid squares) is obtained by Eq. 2.5. In this measurement, the $G = 0$ data is almost constant without any torque contribution, and the $G = 2$ data is predominantly arising from the magnetization.

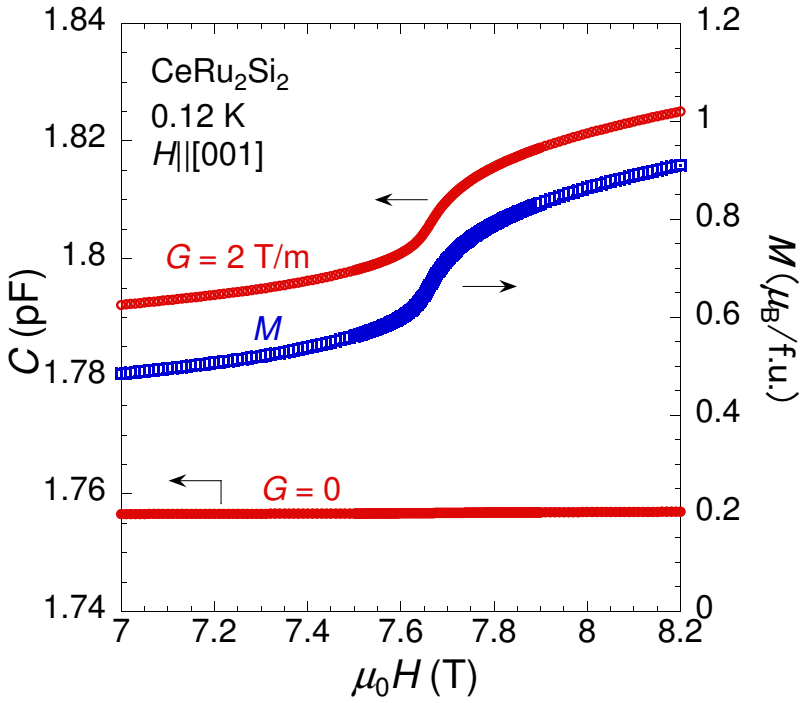

Figure 2.5: Example of the raw capacitance (C) data (solid circles) of $CeRu_2Si_2$ obtained at 0.12 K in magnetic fields along the [001] axis, with the field gradient G = 0 and 2 T/m. Applying Eq. 2.5 to these data yields the magnetization curve (open squares).

2.1.2 Improvement of the capacitive transducer reducing the torque contribution

Figure 2.6 shows a picture of the transducers for the capacitively-detected Faraday method. The transducer on the left hand side is a normal one, and that on the right hand side is a newly-developed one. Cross-sectional view of the normal and the new capacitive transducers are shown in Figs. 2.7(a) and 2.7(b), respectively. The new transducer has been developed in order to investigate materials which have strong anisotropy and therefore exhibit a large torque in a tilted magnetic field. It has been designed as much less sensitive to the torque. The difference between these transducers are as follows.

1. Spring constant of wires of the new one is twice larger than that of the normal one.

2. Pole brace is three times longer than that of the normal one.

We note that the basic structure of the new one is the same as the normal one.

In this new transducer, Mg (60 mg) of 6N purity is used for a sample stage to compensate diamagnetic components which comes from a movable plate and a pole brace made from quartz grass (15 mg) and Stycast1266 (epoxy; 30.5 mg), respectively. In order to suppress de Haas-van Alphen ocillations of Mg metal, a small mount of Al (2 %) is melted into Mg ingot. Mg is particularly suitable for this use, because natural abundance ratio of ^{25}Mg, which has a nuclear magnetic moment ($M_{\mathrm{Nuc}} = -0.85545\mu_N$ per atom [45]) , is only 10 %, and Mg does not exhibit superconductivity [46].

Figure 2.6: Pictures of the transducers for the capacitively-detected Faraday method. Transducer on the left hand side is a normal one, and that on the right hand side is the newly-developed one for reducing torque contribution.

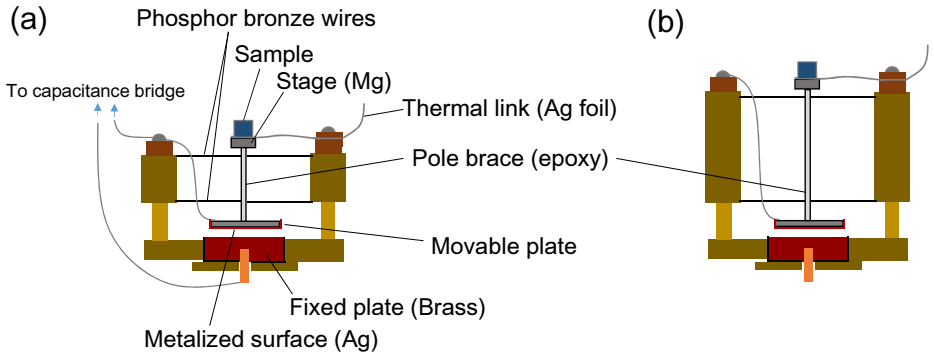

Figure 2.7: Cross-sectional view of the capacitive transducers in Fig. 2.6; (a) normal and (b) newly-developed ones.

2.1.3 Thermometer for magnetization measurements

We have used a ruthenium-oxide thermometer (Model RO-600, Scientific Instrument, Inc.) for reading the temperature. The thermometer is set near the sample, which is connected with a silver thermal link. The temperature is calibrated in a magnetic field by using a universal batch-calibration table for Model RO-600, in which a temperature error is less than 1.6% from 36 mK to 4.2 K in a magnetic field up to 16 T [47].

2.2 Heat capacity and magneto-caloric effect measurements

2.2.1 Method of specific heat measurements

Specific heat is designed by the ratio of the heat added to a material to the resulting temperature change. According to this definition, the specific heat can be obtained by $C = \Delta Q/\Delta T$, where ΔQ is the applied heat, and ΔT is the temperature rise under adiabatic conditions. Figure 2.8 shows a schematic view of a setting for the specific heat measurements. In reality, however, it is difficult to satisfy the adiabatic condition, so that the specific heat is generally measured under conditions in which the sample system is weakly coupled to the thermal bath [48]. Under these conditions (Fig. 2.8; $\kappa \neq 0$), the heat flow equation is as follows:

$$P(t) - \kappa(T(t) - T_0) = C\frac{dT}{dt}, \tag{2.6}$$

where $T(t)$ denote the sample temperature, T_0 is the bath temperature, and $P(t)$ is the heat transfered to the system per unit time. Here, we assume that $C(T)$ and $\kappa(T)$ are constant. Taking the limit of $t \to \infty$ and $P(t)$ being a constant P_0, the input heat flow becomes equal to the one escaping to the bath. Under this condition, the right hand side of the Eq. 2.6 becomes zero, and the following relational expression is obtained;

$$\kappa = \frac{P_0}{T(t=\infty) - T_0} \quad \left(= \frac{P_0}{\Delta T^{\mathrm{sat}}}\right). \tag{2.7}$$

Note that $T(\infty) = T_0 + \Delta T^{\mathrm{sat}}$ and $T(0) = T_0$. Solving the differential equation 2.6, the sample temperature change $T(t)$ of the heating process is given as follows;

$$T(t) = T_0 + \Delta T^{\mathrm{sat}}\left[1 - \exp(-t/\tau)\right] \quad (\tau = C/\kappa)\,, \tag{2.8}$$

where τ is the thermal relaxation time. When the heat pulse P_0 is applied to the sample in an interval $0 \leq t \leq t_0$, the temperature rise at t_0 is estimated by Eq. 2.8;

$$\Delta T = \Delta T^{\mathrm{sat}}\left[1 - \exp(-t_0/\tau)\right]. \tag{2.9}$$

The sample temperature change in the cooling process $T_{\mathrm{cool}}(t)$ is derived by Eq. 2.6 with $P = 0$;

$$T_{\mathrm{cool}}(t) = \Delta T \exp\left[(-(t - t_0)/\tau\right] + T_0. \tag{2.10}$$

This equation indicates that $T_{\mathrm{cool}}(t)$ decreases in the relaxation time τ. Here, $T_{\mathrm{cool}}(t_0) = \Delta T + T_0$ and $T_{\mathrm{cool}}(\infty) = T_0$. In this thesis, the specific-heat measurements are mainly performed by means of the relaxation method, because the short relaxation time $\tau = C/\kappa$ makes it difficult to estimate ΔT correctly. In particular, this method is applicable in the case that the relaxation time becomes as short as a few seconds. In this method, C can be obtained as $C = \kappa\tau$ in Eq. 2.8, where κ and τ are estimated from Eq. 2.7 in the heating process and fittings of the heating (cooling) curve with Eq. 2.8 (Eq. 2.10). The accuracy of the relaxation method may be slightly worse than that of (quasi-) adiabatic method because it contains the multiple fitting process.

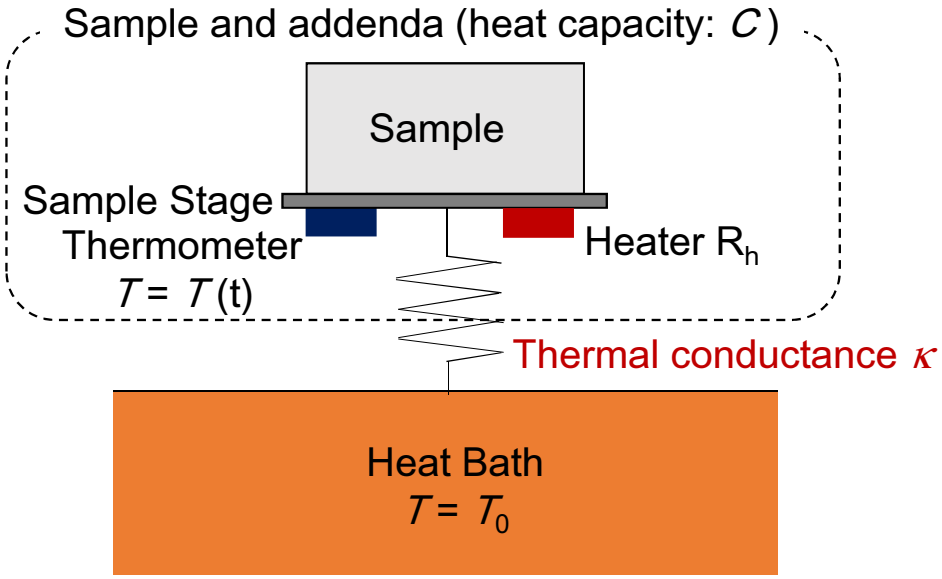

Figure 2.8: A schematic view of a setting for the specific heat measurements.

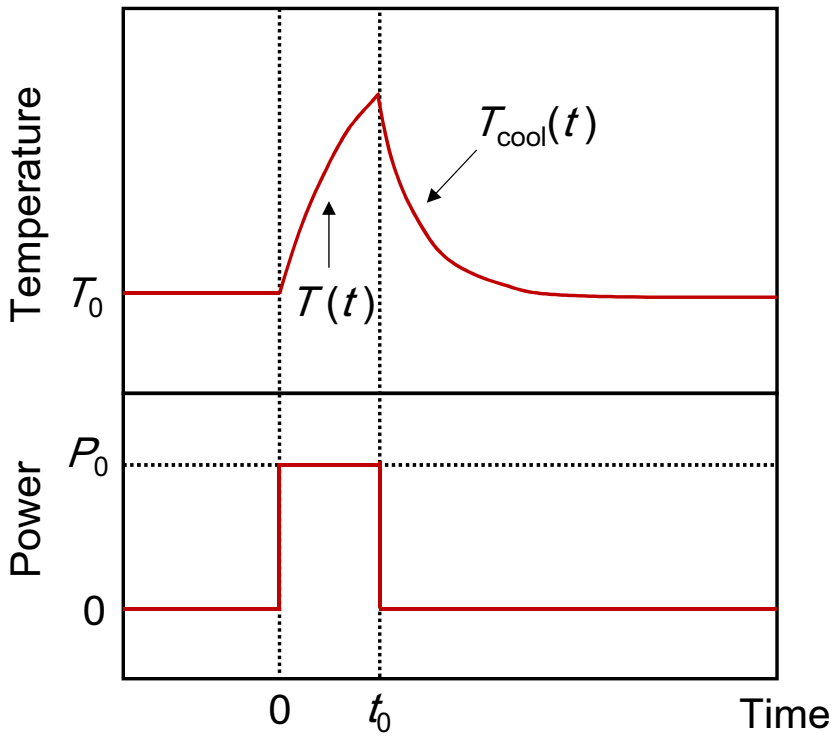

Figure 2.9: Time dependence of the sample temperature $T(t)$ (upper panel) by application of the heat pulse P_0 in an interval of $0 \leq t \leq t_0$ from the addenda heater (lower panel) (Fig. 2.8).

2.2.2 Method of magneto-caloric effect measurements

The magneto-caloric effect (MCE) is a magneto-thermodynamic phenomenon in which exposing a sample to a changing magnetic field causes a temperature change of the sample. Figure 2.10 shows a schematic view of a setting for MCE measurements. The only difference from setting for the specific-heat measurements is that no sample heater is needed for MCE, implying that the same addenda can be used for the both measurements. The basic equation for MCE is expressed as follows [49].

$$\left(\frac{\partial S}{\partial H}\right)_T = -\frac{C}{T_{\rm S}}\left(\frac{dT_S}{dH}\right) - \frac{\kappa(T_{\rm S} - T_{\rm bath})}{T_{\rm S}\dot{H}}, \tag{2.11}$$

where S is the entropy, C is the specific heat of the sample, $T_{\rm S}$ is the sample temperature, $T_{\rm bath}$ is the temperature of the heat bath, κ is the thermal conductance between the sample space and heat bath, and $\dot{H}$ is the sweep rate of the magnetic field H. MCE is a suitable method for discriminating between a second order transition and a first order transition. In the next paragraph, we simulate the behavior of $T_{\rm S}(H)$ in the cases of first order transition (FOT) and second order transition (SOT).

To simulate the behavior of $T_{\rm S}(H)$, Eq. 2.11 is solved by assuming $C(H) = const.$, and $\kappa(H) = const$. For simplicity, we adopt linear field dependences of $S(H)$ as shown in the top two panels of Fig. 2.11:

$$S_{\rm FOT}(H) = \begin{cases} A(H - H_{\rm c1}) + B(H_{\rm c1} - H_{\rm c}) + S_0, (H < H_{\rm c1}) \\ B(H - H_{\rm c}) + S_0, (H_{\rm c1} < H < H_{\rm c}) \\ S_0, (H_{\rm c} < H); \end{cases} \tag{2.12}$$

and

$$S_{\rm SOT}(H) = \begin{cases} A(H - H_{\rm c}) + S_0, (H < H_{\rm c}) \\ S_0, (H_{\rm c} < H). \end{cases} \tag{2.13}$$

In these equations, $H_{\rm c}$ and $H_{\rm c1}$ denote the critical fields of the phase transition and the onset field of the FOT, respectively, and $S_0 \sim 0$. Here, $H_{\rm c} = 11.2$ T and $H_{\rm c1} = 11$ T, and we assume $B/A = 10$ where A and B are coefficients of the slopes of $S(H)$ in the low field phase and the FOT region, respectively. In the case of $\dot{H} = \pm 0.003$ T/sec. and $\tau(= C/\kappa) = 20$ sec., $T_{\rm S}(H)$ is simulated for FOT (left hand side) and SOT (right hand side) as shown in the bottom two panels of Fig. 2.11. In these panels, both of field-up (red) and field-down (blue) sweeps are plotted. As one can see, $T_{\rm S}(H)$ is almost proportional to $-(\frac{\partial S}{\partial H})_T$, and a qualitative difference between FOT (peak in $T_{\rm S}(H)$) and SOT (step in $T_{\rm S}(H)$) is evident.

The same simulation has been performed for metamagnetic transition of URhGe in Chapter 6, and the source code of the plot, which is calculated by using Gnuplot, is given in Appendix B.

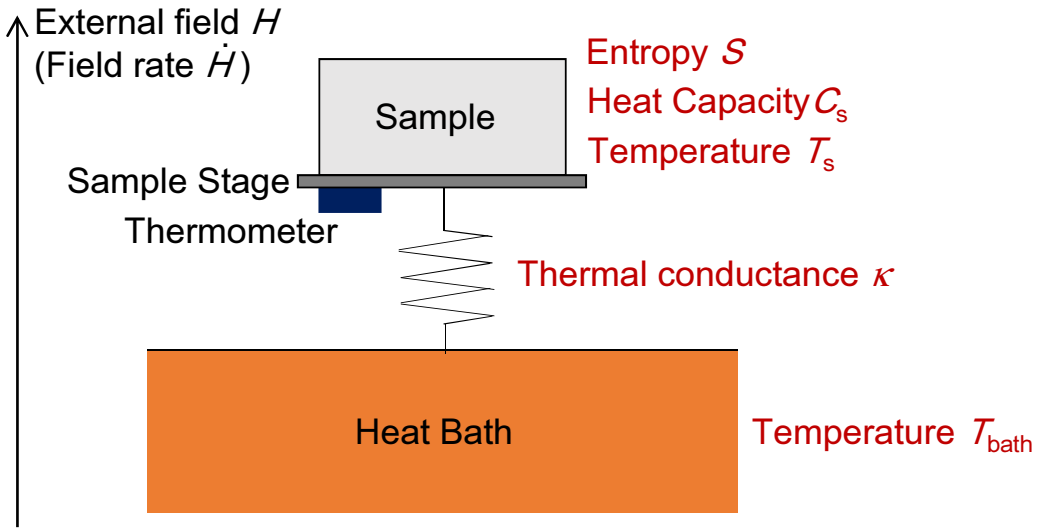

Figure 2.10: A schematic view of a setting for magneto-caloric effect measurements.

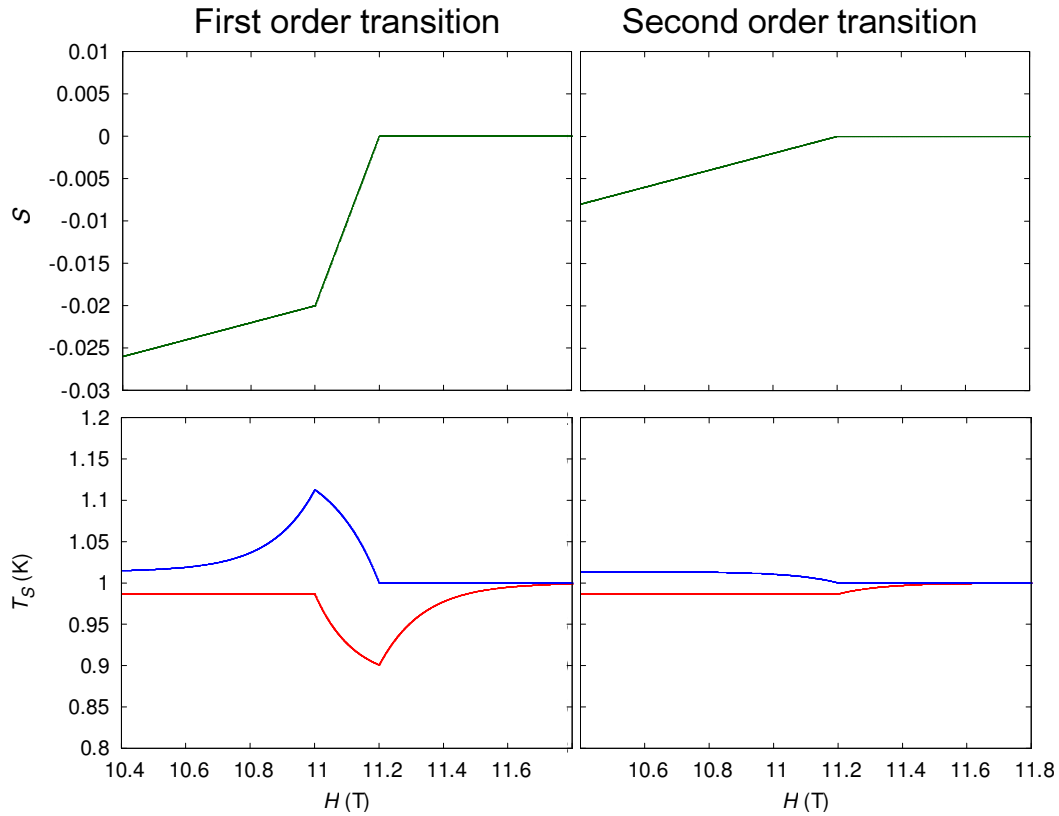

Figure 2.11: Simulated results of magneto-caloric effect measurements in the cases of a first-order transition and a second-order transition. The field dependences of the entropy, assuming linear field dependences, are shown in the top two panels of this figure. The bottom two panels are the field dependences of the sample temperature $T_S(H)$. Both of field-up (red) and field-down (blue) sweeps are plotted in these panels.

2.2.3 newly-developed specific-heat cell for measurements of a high-torque sample

Specific-heat cell has been newly developed for the measurements of a sample induces a large torque in a magnetic field. A photo of the cell is shown in Fig. 2.12. The sample is mounted on a sample stage (Ag plate) with vanish (GE7031). In order to reduce a rotation of the sample by the torque, the stage is firmly fixed by two mechanical pencil leads, which have very small heat conductivity. One end of the leads goes through a stainless pipe, that is attached on the heat bath, and the other end is fixed to the opposite side of the bath by using vanish. The pipe plays an essential role to prevent the leads from breaking by a thermal contraction. The thermometer and the heater for addenda is set on the opposite side of the stage, and those for the bath is located in the area which is indicated by the dotted white circle in this figure.

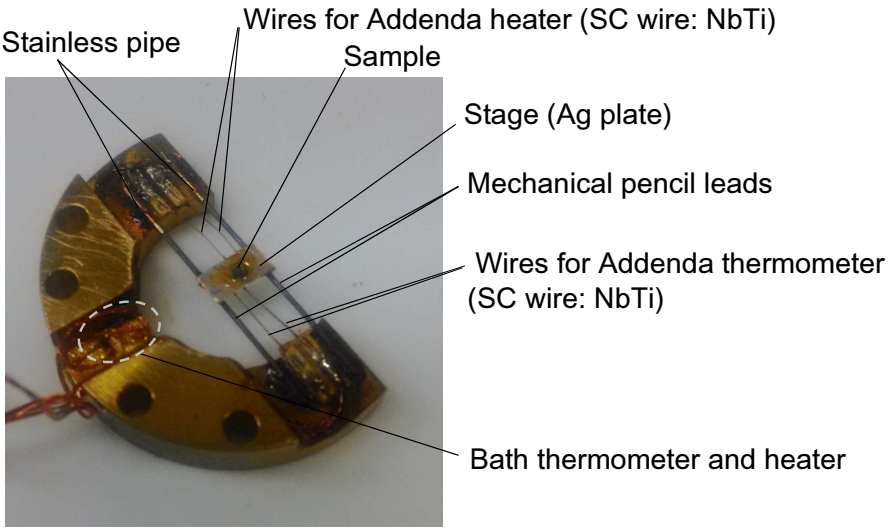

Figure 2.12: A photo of newly-developed specific-heat cell.

2.2.4 Thermometer for specific heat measurements

We have used thick-film chip resistor (KOA, Inc., RK73B-1E-202 [50]) for thermometers of bath and addenda of specific-heat cell. These resistor-thermometers are thermally cycled before using, and calibrated in a magnetic field by using ruthenium-oxide thermometer (ENTROPY, Inc., Model B020 [51]). The thermometers are directly mounted on the bath and the addenda by vanish (GE7031).

Chapter 3

Development of a two-axis rotation device

3.1 Introduction

There is continuing interest in expanding the range of experiment to lower temperatures, stronger magnetic fields, and higher pressures. Investigating heavy fermion systems, in which exotic ground states such as unconventional superconductivity, multipole order etc., are realized, often demands field-angle-resolved measurements at very low temperature ($\sim$ 100 mK) and at relatively high fields ($\sim$ 10 T), because of complex anisotropy in these systems. In particular, such an angle-resolved measurement is needed to investigate the wing structure of an Ising ferromagnet URhGe. Up to present, however, not much attempt has been done on dc magnetization measurements on this compound owing to technical difficulties.

In this thesis, we have developed the device for dc magnetization measurements with two-angle precise rotation within accuracy of less than 0.01° using a piezo-stepper-driven goniometer (ϕ rotation) [52] and a home-made tilting stage (θ rotation) [53, 54], where $-3^\circ \leqq \phi \leq 3^\circ$ and $-10^\circ \leq \theta \leq 10^\circ$. By installing this device into the Faraday magnetometer (Chapter 2), dc magnetization measurements with in-situ two-angle control of the magnetic field direction have been made at temperatures down to 0.1 K in magnetic fields up to 14.5 T.

3.2 The schematic view of the Device

The device is installed and cooled by a ^{3}He-^{4}He dilution refrigerator. Figure 3.1(a) is schematic view of ^{3}He-^{4}He dilution refrigerator, in which the newly developed two-axis rotation device is installed. The device is located at the lower end of the dilution refrigerator in the vacuum can. The capacitive transducer is mounted on the device to perform magnetization measurements by the Faraday method.

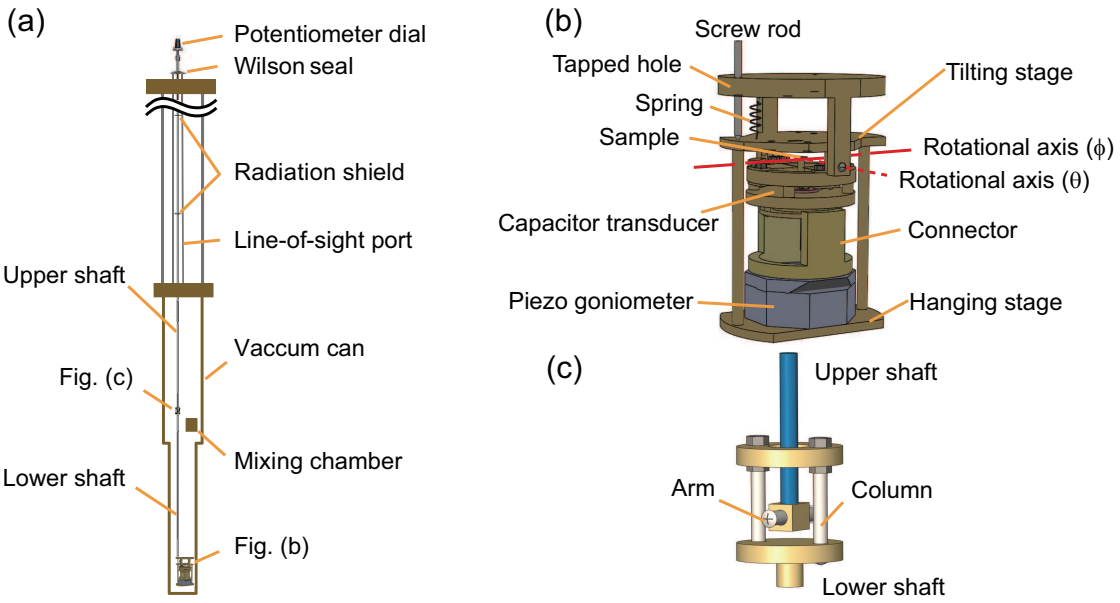

Figure 3.1: (a) Schematic view of the device for fine tuning of the magnetic field by two angles, installed in a dilution refrigerator. The device is mounted on the lower-end of the refrigerator in vacuum can, and the enlarged view is shown in Fig. 3.1(b). (b) Enlarged view of the two-angle rotation device, on which the capacitive transducer with a sample is mounted. The detail of, how the device rotates, is explained in Fig. 3.2(c). Enlarged view of the thermal isolator to cut a heat flow from room temperature region into the sample space. The direction of the magnetic field is vertical upward.

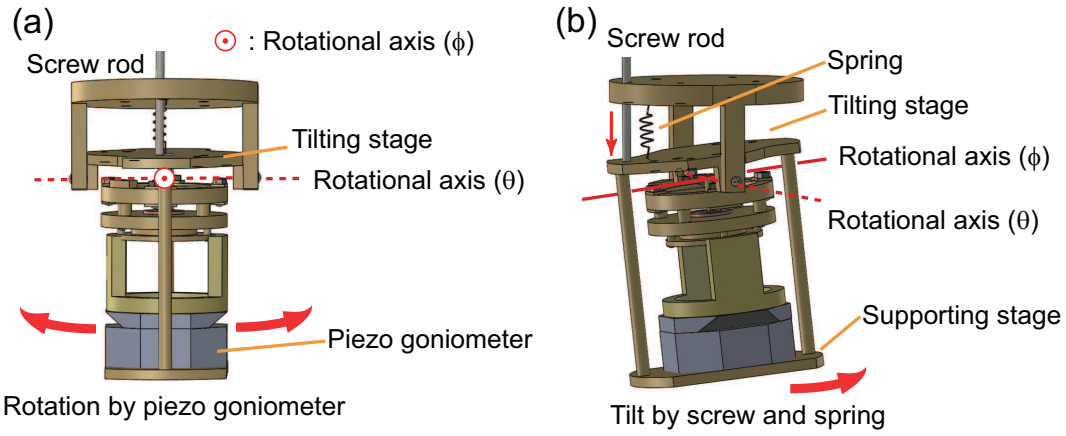

Figure 3.2: (a) A side view of the two-angle rotator. The capacitor transducer is mounted on the piezo goniometer, which is fixed on a supporting stage attached to a tilting stage. The piezo goniometer rotates the sample around the ϕ axis, as indicated by the arrows. (b) θ-rotated state of the rotational device. In this figure, the sample is rotated around the θ axis by rotating the tilting stage, as indicated by the arrows. One side of the tilting stage is pushed down by the screw rod connected to the lower shaft in Fig. 3.1(a).

The orientation of the sample is precisely controlled within an accuracy of less than 0.01° using a piezo-stepper-driven goniometer (ϕ rotation) combined with a home-made tilting stage (θ rotation) in the angle range $-3° \leq \phi \leq 3°$ and $-10° \leq \theta \leq 10°$, where the ϕ and θ axes are perpendicular to each other, intersecting at the sample position. Figure 3.1(b) shows a schematic view of the two-angle rotation device. Red lines in this figure show the rotational axes of ϕ and θ, and a sample is set on the sample stage of the capacitive transducer at the rotation center. Image of the rotation by a piezo-stepper goniometer (ANGt101, Attocube, Inc. [52]) and a movement of the tilting stage is shown in Figs. 3.2(a) and 3.2(b). The direction of the magnetic field is vertical upward. In this device, the capacitive transducer, in which the sample is mounted, is fixed on the piezo goniometer, and the piezo goniometer is hung from the tilting stage. In Fig. 3.2(a), the directions of the rotation by the piezo goniometer are shown by thick red arrows, and the rotational axis, which goes through the sample position, is perpendicular to the paper surface. Figure 3.2(b) shows the state in which the tilting stage is inclined towards thick red arrow direction. As shown in Fig. 3.2(b), one side of the tilting stage is pushed down (pulled up) by the screw rod (the spring), and the tilting angle of the stage is controlled by a rothation of the screw rod. This figure depicts the state that the screw rod pushes down the tilting stage towards the thin arrow direction, and the

piezo goniometer, the the whole assembly is tilting around the θ axis. The two-angle rotation device is made of brass, except for the piezo goniometer (mostly titanium) and the spring (ϕ0.3 copper beryllium wire).

The angle of the tilting stage is adjusted by a revolution of the screw rod from the top of the refrigerator insert by upper and lower shafts made of glass epoxy, which goes through a line-of-sight port of the refrigerator insert. The glass epoxy has low thermal conductivity and is nonmagnetic, so it is suitable as the material used for the shaft. The rotation of the screw rod is read by a potentiometer dial, which is located at the top of the refrigerator, and one revolution of the screw rod corresponds to the one revolution of the dial. The relation between the revolution number n of screw (potentiometer) and the tilting angle $\Delta\theta$ (unit: degree) from the position of $\theta = 0^\circ$ is determined by the relation below.

$$\Delta\theta = \frac{180}{\pi}\arctan\left(\frac{0.4n}{16}\right), \tag{3.1}$$

where the pitch of the screw is 0.4 mm, and the position of the screw rod from the rotation center is 16 mm. This relation implies that one revolution of the screw rod corresponds to a rotation of tilting the stage of 1.43 degree. The potentiometer has a scale that divides one rotation into 100, indicating that a scale revolution of the meter causes the rotation of 0.014 degree.

We introduce a thermal isolator between the upper and the lower shafts, as shown in Fig. 3.1(a). The upper shaft can be physically decoupled from the lower one by using this thermal isolator. An enlarged figure of the thermal isolator is shown in Fig. 3.1(c). Two arms, which extend in the horizontal direction on a straight line, are fixed at the lower edge of the upper shaft, and two columns, which is connected to lower shaft with a disk. Another upper disk, which is put on column, have a hole in the center, and upper shaft goes through the disk without touch. This upper disk is used only for keeping safety of shaft's movement. Thermal isolation is realized by a disconnection of arms and columns, which are fixed to the upper and the lower shafts, respectively. In Fig. 1(c), the upper shaft is not connected to lower one. When the potentiometer dial is rotated more than $\sim 90^\circ$, the arms of the upper shaft touch the columns of lower shaft. Tilting stage can be moved only when these shafts come in contact with each other, and these shafts are disconnected during the measurement in order to cut a heat flow from the upper part.

3.3 Mechanical issues of the magnetization measurements with two-axis rotation device

As shown in Chapter 2, the capacitance transducer experiences a magnetic force $F = (M \cdot \nabla)B$ $(= M_z dH_z/dH_z)$ in the present Faraday method. There are two mechanical issues in measuring the magnetization with the two-axis rotation device, as described below.

3.3.1 Influence of tiling transducer on the sensitivity

The capacitive transducer detects the magnetic force F, whose direction is perpendicular to the electrode surface. When the transducer is tilted by θ deg. from the original position, the sensitivity reduces as becomes $F\cos\theta$, where the F is tassumed to be vertical direction. In the present experiment, the largest θ is $\sim 10^\circ$, and the change of the sensitivity is roughly estimated to be $\cos(10^\circ) \sim 0.985$. From this estimation, the tilting of the device has a small influence on the sensitivity of the magnetization measurements in the angular range $|\theta| < 10^\circ$.

3.3.2 Misalignment of the magnetic field caused by the application of a field gradient

As described in Chapter 2, we take a difference between the capacitances value with the field gradient $G = dH_z/dz$ and without G, to obtain the magnetization value. Ideally, switching G should not affect the magnetic field orientation. If the sample is slightly off center along a lateral direction, however, the field direction may be deflected according to G. When the field gradient is applied, we expect the horizontal component of G, $dH_x/dx = dH_y/dy = -\frac{1}{2}dH_z/dz$ (in vacuum), at the magnet center from Maxwell equation div$\boldsymbol{B} = 0$. The vertical field gradient $G = 8$ T/m along the z axis thus produce a field gradient of order 4 T/m along the x and y axes. An off-center displacement of the sample of 1mm then results in a lateral field of 4 mT.

Chapter 4

Performance evaluation of the newly developed rotation device

We have checked the performance of the newly developed two-axis rotation device by measuring the angular dependence of the magnetization curves of a reference sample of $CeRu_2Si_2$.

4.1 Introduction for $CeRu_2Si_2$

$CeRu_2Si_2$ is a nonmagnetic heavy-electron paramagnet having a large electronic specific-heat coefficient $\gamma \sim 350$ mJ/mol K^2 [55]. $CeRu_2Si_2$ does not exhibit magnetic order nor superconductivity down to very low temperatures, and remains in a typical Fermi-liquid behaviors [56]. This compound crystallizes in the tetragonal $ThCr_2Si_2$ structure with a space group of $I4/mmm$, in which Ce atom locates at the position of the body-centered tetragonal lattice (Fig. 4.1). This material exhibits a metamagnetic behavior at the field of $\mu_0 H_\mathrm{m} \sim 7.7$ T along the magnetization easy c axis (the [001] direction) below 15 K [56–60]. Previously reported de Haas-van Alphen (dHvA) frequencies change discontinuously at H_m (Fig. 4.2), possibly suggesting a drastic change of the Fermi surface [61–63]. It has been proposed that an itinerant-to-localized transition occurs through H_m, accompanied by this metamagnetic transition [62]. According to the neutron-diffraction measurements [64, 65], short-range antiferromagnetic correlations appear below 60 K at low magnetic fields, and they disappear at H_m, above which paramagnetic state remains. From previous dc magnetization measurement, the metamagnetic behavior becomes sharper at low temperature region, and the magnetization reaches a relatively large value of $\sim 1.5\,\mu_B$/Ce well above the field $\mu_0 H_\mathrm{m}$ as shown in Figs. 4.3 and

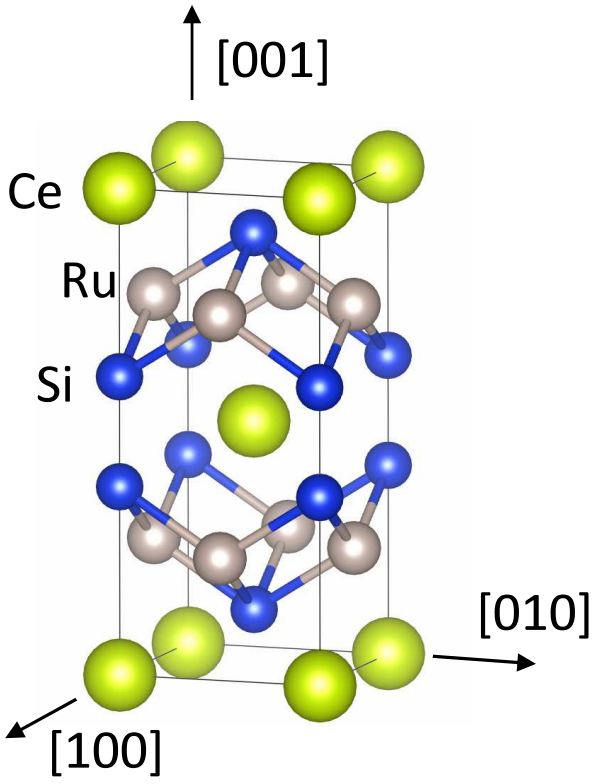

Figure 4.1: Crystal structure of the $CeRu_2Si_2$.

4.4 [66]. Even at the lowest temperature of ~ 90 mK in the previous magnetization measurements, the magnetization curve does not show a discontinuous behavior at H_m without any hysteresis, indicating the absence of first-order nature. The transition is caused by a change of Fermi surface, and such transition is normally called Lifshitz transition.

Meanwhile, the discontinuity in the previous dHvA frequencies, however, may suggest that a first-order transition exists in reality but has not been captured by magnetization measurements for the same reason such as misalignment of the magnetic field direction. In this present study, we revisit the transition by measuring the magnetization with high-precision in-situ field-alignment.

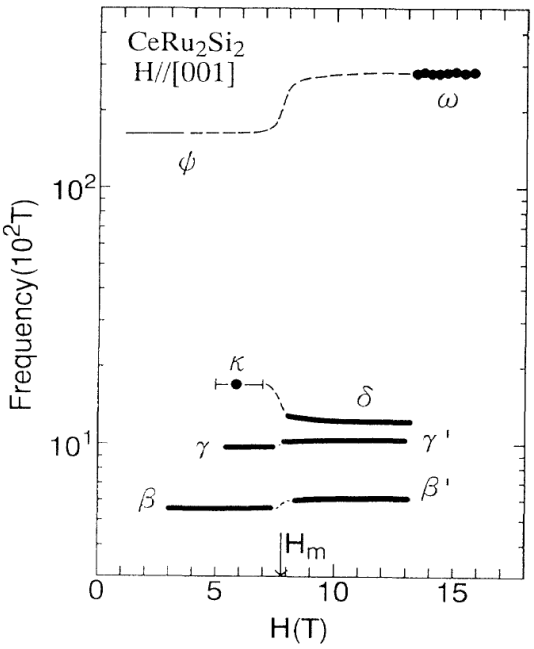

Figure 4.2: Field dependences of the dHvA frequencies of $CeRu_2Si_2$ in fields $B \parallel c$ axis ($H \parallel [001]$) [62].

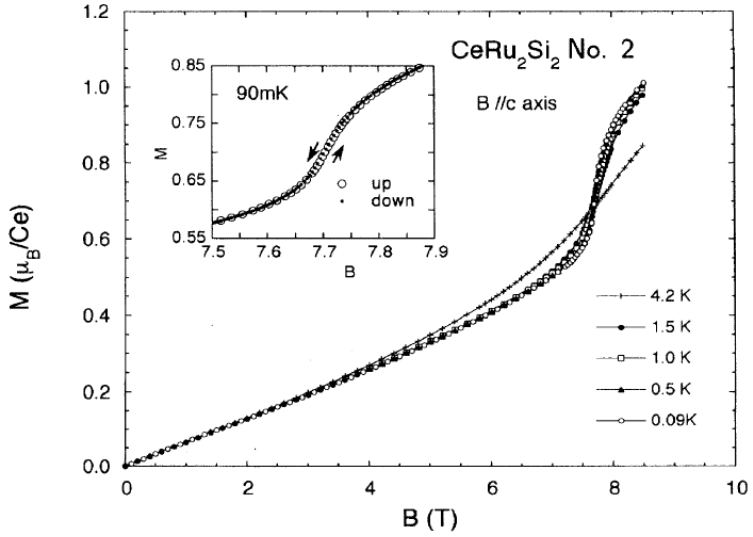

Figure 4.3: Magnetization of $CeRu_2Si_2$ in fields $B \parallel c$ axis ($H \parallel [001]$) [66].

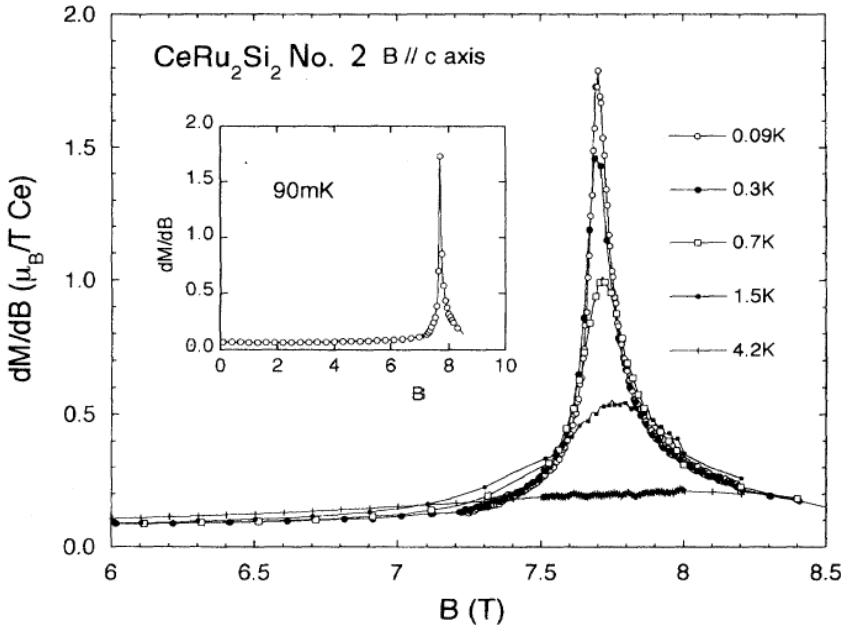

Figure 4.4: Differential susceptibility of $CeRu_2Si_2$ in fields $B \parallel c$ axis ($H \parallel [001]$) [66].

4.2 Motivation

In order to check the performance of newly-developed two-axis rotation device, we have measured the magnetization of $CeRu_2Si_2$. This compound is suitable for checking the performance of the device, because of two reasons as follows.

1. This compound shows a metamagnetic behavior at low temperature region.

2. Owing to its strong anisotoropy, only the magnetic field component along the magnetization easy c axis (the [001] direction) is relevant for the metamagneism.

We planned to check whether the transition changes from a crossover to a first order transition, which have discontinuous metamagnetic jump, in field precisely along the c axis. The newly developed two-axis rotation device is powerful for checking the field-angle dependence of the transition in systems that have strong anisotropy.

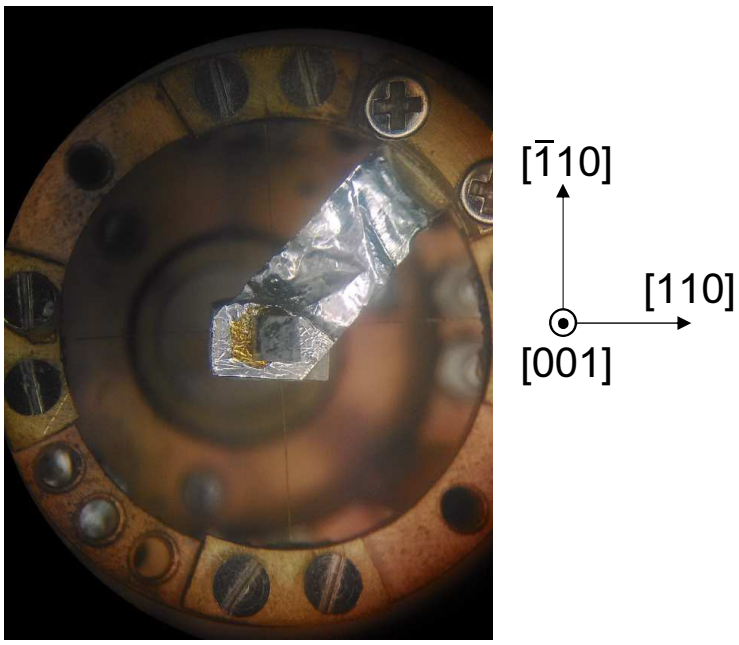

Figure 4.5: Picture of the sample mounted on the stage of the magnetometer viewed from the [001] direction, which is almost parallel to the z axis.

4.3 Experimental Procedure

The single crystalline sample of $CeRu_2Si_2$ is the same one used in the previous measurements [66], 2.95[001]×1.88[110]×2.01[$\bar{1}$10] with a weight of 77 mg. Dc magnetization measurements in the magnetic fields near the [001] direction were performed by means of a capacitively-detected Faraday magnetometer installed with two-axis rotation device, whose detail is shown in Chapter 3. A ^{3}He-^{4}He refrigerator was used for cooling the sample to low temperature range of 0.12 K $\leq T \leq$ 1 K, and static magnetic fields up to 14.5 T were applied along the z direction. Figure 4.5 shows a picture of the sample mounted on the stage of the transducer with varnish (GE7031), viewed from the [001] direction, which is almost parallel to the z axis. In-situ orientation was achieved within an accuracy of less than 0.5° in the ranges of angle $-7° \leq \theta \leq 7°$(θ : angle from the [001] direction towards the [110] direction) and $-2° \leq \phi \leq 2°$(ϕ : angle from the [001] direction towards the [$\bar{1}$10] direction).

4.4 Results and Discussion

4.4.1 Adjustment of angles

Figure 4.6 shows an example of the data processing, in which the raw capacitance (C) data of $CeRu_2Si_2$ obtained at 0.12 K in magnetic fields along the [001] axis are shown with the field gradient $G = 0$ and 2 T/m. Taking a difference of these two data yields the magnetization curve (open squares). In this measurement, the $G = 0$ data is almost constant, and the $G = 2$ data is qualitatively the same as the magnetization in the magnetic field along the [001] axis. Note that hysteresis of the magnetization curve is not observed in this measurements.

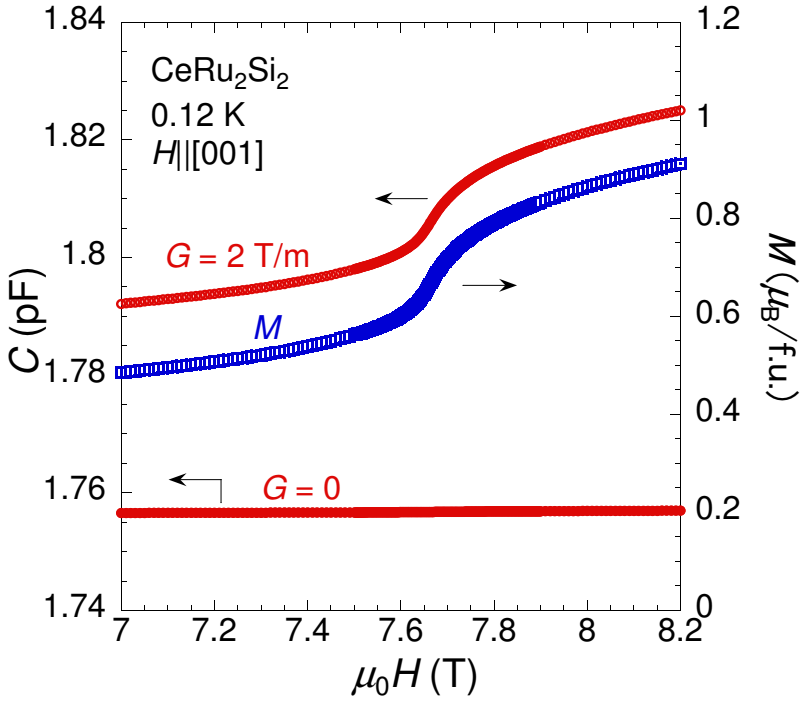

Figure 4.6: Example of the raw capacitance (C) data (solid circles) of $CeRu_2Si_2$ obtained at 0.12 K in magnetic fields along the [001] axis, with the field gradient $G = 0$ and 2 T/m. Both field increasing and decreasing sweeps are plotted. Taking a difference of these two yields the magnetization curve (open squares).

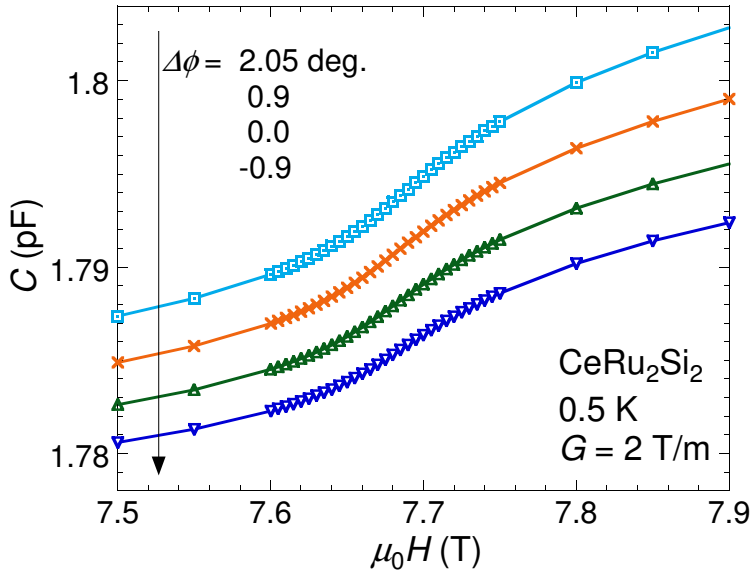

Figure 4.7: ϕ dependence of the raw capacitance curve C with $G = 2$ T/m near the metamagnetic crossover at 0.5 K at $(\Delta\theta, \Delta\phi) = (0, 2.05), (0, 0.9), (0, 0)$ and (0, -0.9), where the θ and ϕ are angles in the unit of degree from the the [001] direction towards the [110] direction and the the $[\bar{1}10]$ direction, respectively.

In order to precisely adjust the [001] direction of the sample along the magnetic field direction, we have measured the magnetization on the [001]-[110] plane. Figure 4.7 shows ϕ dependence of the raw capacitance curve $C(H)$ with $G = 2$ T/m near the metamagnetic crossover at 0.5 K at $(\Delta\theta, \Delta\phi) = (0, 2.05), (0, 0.9), (0, 0)$ and (0, -0.9), where the θ and ϕ are angles in the unit of degree from the the [001] direction towards the [110] direction and the the $[\bar{1}10]$ direction, respectively. Here, $(\Delta\theta, \Delta\phi) = (0, 0)$ denotes the initial position of the two-axis rotation device, when the device is cooling down. The field derivative of the data dC/dH and dC/dH peak position are shown in Figs. 4.8 and 4.9, respectively. The peak position was defined as the critical field H_{m} of the metamagnetic crossover. The ϕ dependence of the dC/dH peak can be fitted with a function (dotted line), $H_{\mathrm{m}}(\Delta\phi) = H_{\mathrm{m}}(0.6)/\cos(\phi + a)$, where $H_{\mathrm{m}}(0.6) = 7.68$ T and $a = 0.6$ are determined by the fitting, as shown in Fig. 4.9, suggesting that the magnetic field along the [001] direction is dominant in the critical field of the metamagnetic transition near the [001]-$[\bar{1}10]$ plane. In Fig. 4.9, the data points mirrored at $\Delta\phi = 0.6°$ are also plotted. The minimum of $H_{\mathrm{m}}(\Delta\phi)$ locates at $\Delta\phi = 0.6°$, implying that the position of $\Delta\phi = 0.6°$ is the closest to the b axis.

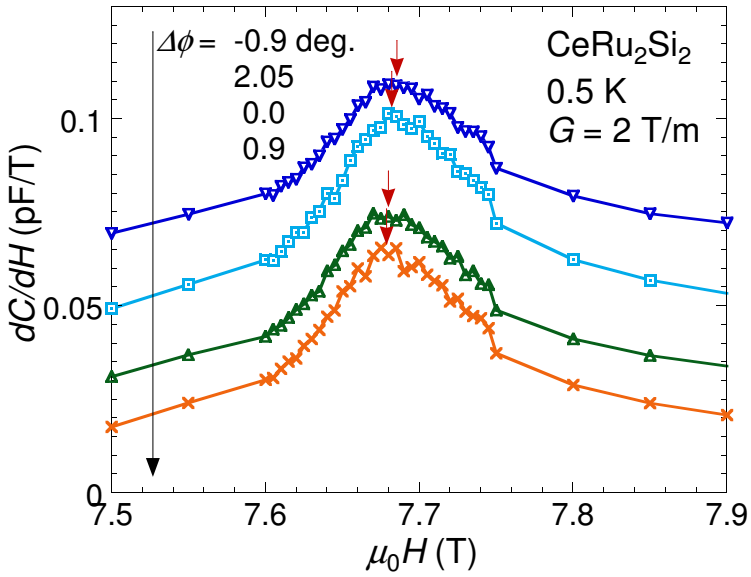

Figure 4.8: ϕ dependence of the field derivative of the capacitance data dC/dH. The red arrows are the the peak position of dC/dH.

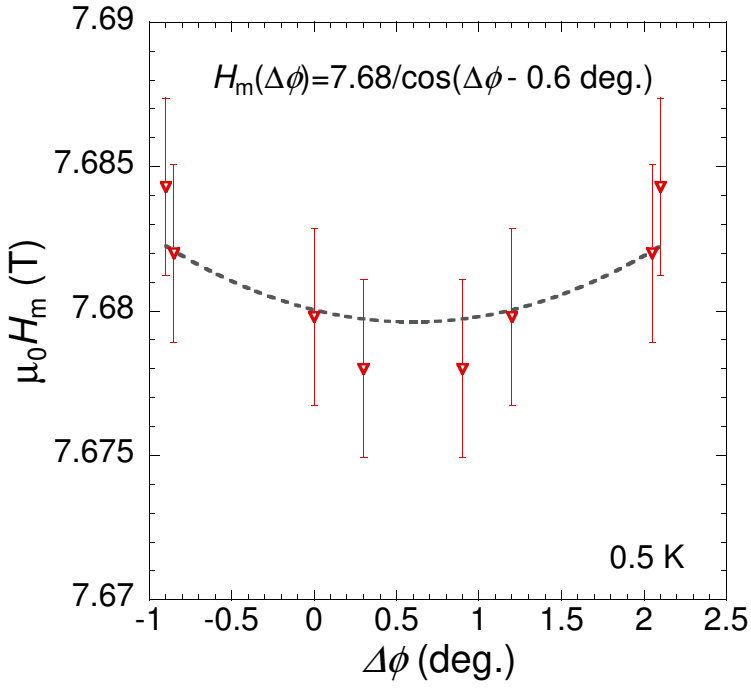

Figure 4.9: ϕ dependence of the dC/dH peak can be fitted with a function (dotted line), $H_{\mathrm{m}}(\Delta\phi) = H_{\mathrm{m}}(0.6)/\cos(\phi + a)$, $H_{\mathrm{m}}(0.6) = 7.68$ T and $a = 0.6$ are determined by the fitting. In this figure, the data points mirrored at $\Delta\phi = 0.6°$ are also plotted.

Next, in order to adjust the position of θ, we have measured the θ variation of magnetization curves under a condition that the position of ϕ is fixed at $\Delta\phi = 0.6°$. Figure 4.10 shows θ dependence of the magnetization curve at 0.15 K on $\phi = 0°$ plane, measured at $(\Delta\theta, \Delta\phi) = (4.25, 0.6), (5.68, 0.6), (7.11, 0.6)$, (8.54, 0.6) and (9.96, 0.6). The critical field of the metamagnetic crossover becomes higher with increasing $\Delta\theta$. The field derivative of the magnetization curves dM/dH and the positions of dM/dH peak, $H_{\mathrm{m}}(\Delta\theta)$, are plotted in Figs. 4.11 and 4.12, respectively. The θ dependence of the dM/dH peak position can be fitted with a function of $H_{\mathrm{m}}(\Delta\theta) = H_{\mathrm{m}}(4.25)/\cos(\Delta\theta + b)$ (dotted line), where $H_{\mathrm{m}}(4.25) = 7.653$ T and $b = 4.25$ are determined by the fitting, suggesting that $H_{\mathrm{m}}(\Delta\theta)$ can be scaled by the [001] component of the magnetic field. In this figure, the data points mirrored at $\Delta\theta = 4.25°$ are also plotted. We have also checked the position of $H_{\mathrm{m}}(\Delta\theta)$ becomes higher with decreasing $\Delta\theta$ from zero. The minimum of $H_{\mathrm{m}}(\Delta\phi)$ locates at $\Delta\theta = 4.25°$, indicating that the position of $\Delta\theta = 4.25°$ is the closest to the b axis. Up to present, that the position of $(\theta, \phi) = (0, 0)$, at which a magnetic field is applied along the the [001] direction, has successfully determined to be $(\Delta\theta, \Delta\phi) = (4.25, 0.6)$. The adjustment error of the angles, which is less than 0.5° in this situation, is depend on the anisotropy of the sample, and the error is larger than the accuracy of this rotation device (0.01°).

Note that the weakening and the broadening of the dM/dH peak with increasing the angles from the origin can be caused not only by the anisotropy of the sample but also by the reasons as follows. The weakening of the dM/dH peak is due to the angular dependence of the sensitivity of the magnetometer as described in section 3.3.2. The sensitivity at $\theta = 6°$ is 1 percent less than that of the horizontal position of $(\theta, \phi) = (0, 0)$. The broadening of the dM/dH peak is owing to the change of [001] component of dH, when the [001] component of the magnetic field is dominant in the metamagnetic jump.

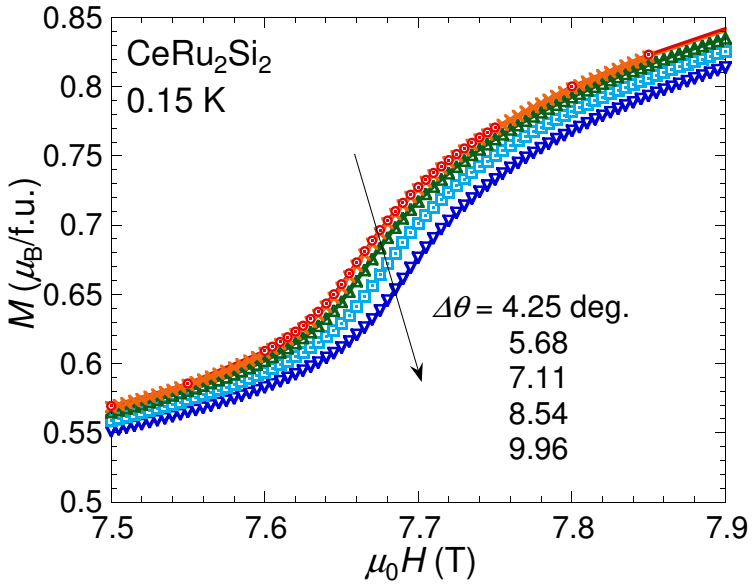

Figure 4.10: θ dependence of the magnetization curve at 0.15 K on $\phi = 0°$ plane, measured at $(\Delta\theta, \Delta\phi) = (4.25, 0.6), (5.68, 0.6), (7.11, 0.6)$, (8.54, 0.6) and (9.96, 0.6).

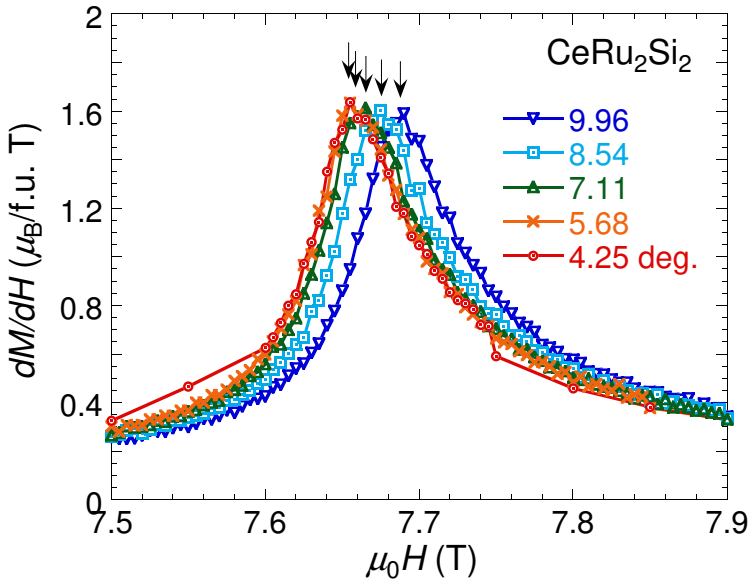

Figure 4.11: θ dependence of the field derivative of the magnetization curves dM/dH. The arrows are the the peak position of dM/dH.

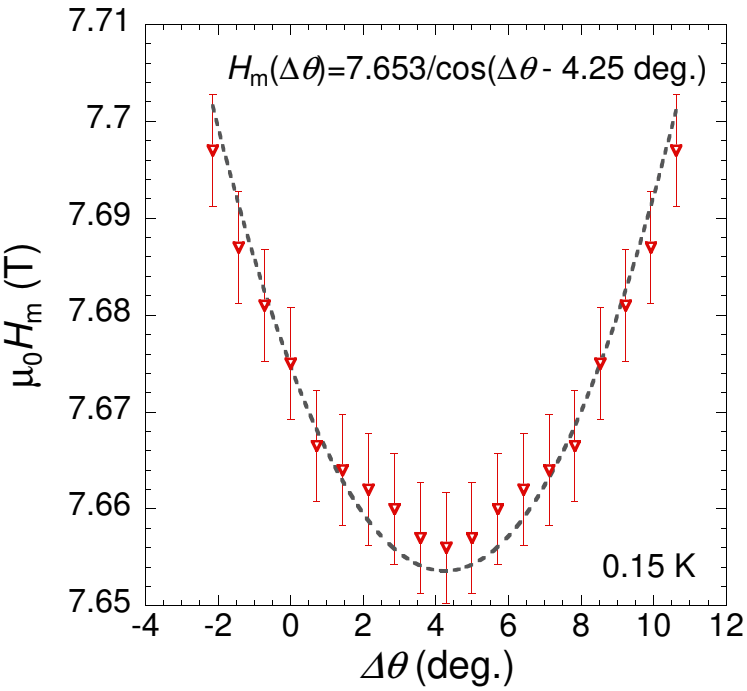

Figure 4.12: θ dependence of the dM/dH peak position can be fitted with a function of $H_m(\Delta\theta) = H_m(4.25)/\cos(\Delta\theta + b)$ (dotted line), where $H_m(4.25) = 7.653$ T and $b = 4.25$ are determined by the fitting. In this figure, the data points mirrored at $\Delta\theta = 4.25°$ are also plotted.

4.4.2 Magnetization of $CeRu_2Si_2$ in magnetic field along the [001] direction with in-situ alignment

The magnetization curves in the magnetic field along the [001] direction with in-situ alignment are measured in several temperatures. Figure 4.13 shows the temperature dependence of the magnetization curves near the metamagnetic transition at $(\theta, \phi) = (0, 0)$, in the magnetic field along the [001] direction, measured at 0.12, 0.4, 0.7, and 1 K. In this figure, only the field-down-sweep traces are plotted for simplicity. Figure 4.14 shows the magnetization curves in the magnetic field along the [001] direction at 0.12 K for both field-up and field-down sweeps, where field-down sweep is also shown in Fig. 4.13. The metamagnetic transition is observed at 7.66 T, and there is no hysteresis even at 0.12 K. The derivative of the magnetization curves dM/dH in Fig. 4.13 is shown in Fig. 4.15, and the position of the metamagnetic transition, which is decided by the dM/dH peak position, is clear in this figure. The temperature dependence of $M(H)$ curves and the derivative are agree with the previous magnetization measurement [66], whose results are already shown in Figs. 4.3 and 4.4. As a result, a nature of the first order transition, i.e. a hysteresis, is not observed even with in-situ alignment of magnetic field along the [001] direction in the present magnetization measurements.

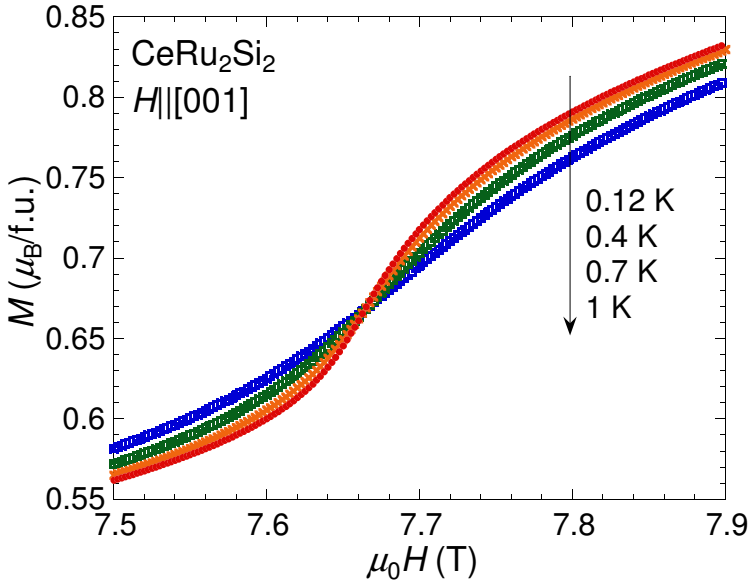

Figure 4.13: Temperature dependence of the magnetization curves near the metamagnetic transition at $(\theta, \phi) = (0, 0)$, in the magnetic field along the [001] direction.

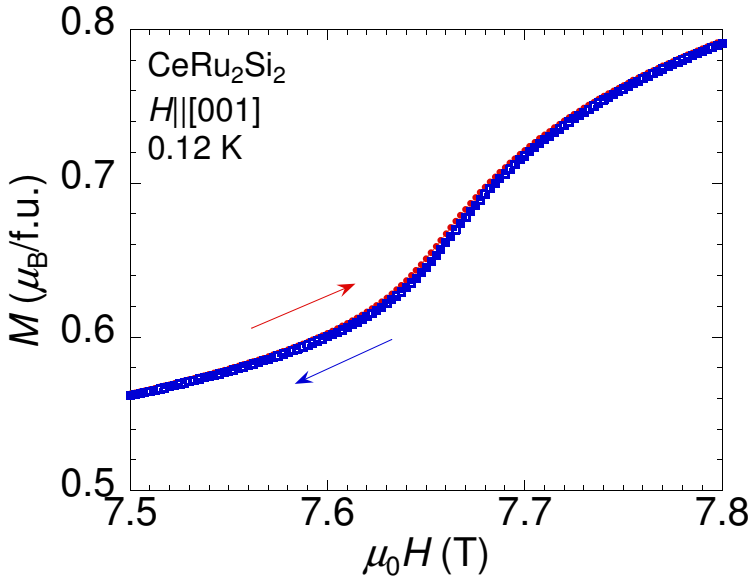

Figure 4.14: The magnetization curves in the magnetic field along the [001] direction at 0.12 K for both up- and down-field sweeps, where down-field sweep is also shown in Fig. 4.13. The metamagnetic transition is observed at 7.66 T, and there is no hysteresis.

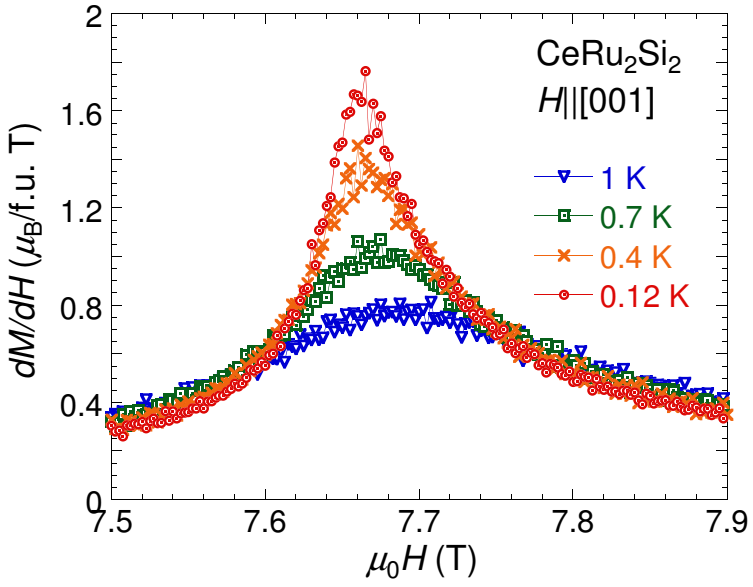

Figure 4.15: The derivative of the magnetization curves dM/dH in Fig. 4.13.

4.5 Summary of the performance evaluation

To measure the magnetization and the magnetization torque under two-angle precisely-controlled magnetic field orientation, we have developed a capacitively-detected Faraday magnetometer installed with two-angle precisely-controlled device. The orientation of the sample is precisely controlled within an accuracy of less than 0.01° using a piezo-stepper-driven goniometer (ϕ rotation) combined with a home-made tilting stage (θ rotation) in the angle range $-3^\circ \leq \phi \leq 3^\circ$ and $-10^\circ \leq \theta \leq 10^\circ$, where the ϕ and θ axes are perpendicular to each other. In order to test the performance of the device, the angular θ and ϕ dependences of the magnetization curves of $CeRu_2Si_2$ have been measured. θ and ϕ are driven by a home-made tilting stage and a piezo stepper goniometer, respectively. In this measurements , a metamagnetic jump is observed at low temperatures, and the angular θ and ϕ dependences of the critical fields are scaled by $1/\cos\theta$ and $1/\cos\phi$, respectively, suggesting that the rotation device works at low temperature below 4 K. We also checked the θ and ϕ position repeatability.

The properties of magnetization curve of $CeRu_2Si_2$ do not change from previous magnetization study even in "in-situ" magnetic field along the [001] axis, supporting a metamagnetic crossover scenario.

Chapter 5

Magnetization measurements in URhGe

Main contents of this chapter have been summarized, and published in S. Nakamura *et al.*, Phys. Rev. B, **96**, 094411 (2017) [67].

5.1 Introduction of URhGe

Coexistence of superconductivity and ferromagnetism has been observed in U-based heavy-fermion superconductors is a very interesting topic. In particular, the heavy-fermion compound URhGe has attracted considerable interest because it shows a re-entrant superconductivity (RSC) in high magnetic field of $\mu_0 H_R \sim 12$ T, which is much larger than the Pauli limit ($\sim$ 1 T in URhGe), along the b axis [41, 68, 69]. Figure 5.1 shows $H-T$ phase diagram of URhGe in the magnetic field along the b axis [41]. Surprisingly, the critical temperature of the RSC ($\sim$ 0.45 K) is higher than the one of the superconducting state at low field ($\sim$ 0.3 K) in this material.

URhGe is known to be an itinerant Ising ferromagnet in which a magnetic moment M of $\sim$ 0.4 μ_B/U aligns along the magnetization easy c axis below $T_C \sim 9.5$ K [68, 69]. Fig. 5.2 shows the crystal structure of the URhGe. This compounds crystallizes in the orthorhombic TiNiSi structure with the space group *Pnma* [70]. The spontaneous moment along the c axis is schematically drawn by the black arrows on the uranium site. The uranium zig-zag chain with the distance of the next nearest neighbor $d_{U-U} \sim 3.5$ Å is formed along the a axis.

Owing to strong anisotropy of URhGe, T_C of this compound can be tuned to zero by applying a magnetic field H along the b axis, perpendicular to the spontaneous

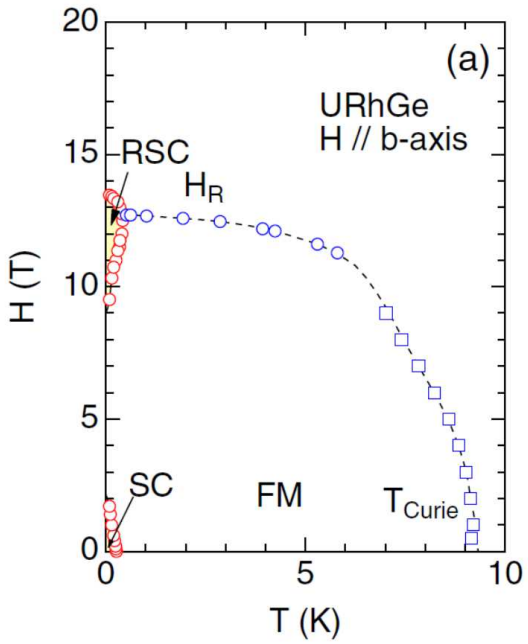

Figure 5.1: $H - T$ phase diagram of URhGe in the magnetic field along the b axis [41].

moment [69]. The situation is analogous to an Ising ferromagnet in a transverse magnetic field [3], for which a quantum phase transition (QPT) accompanying a reorientation of the magnetic moment into a state with $M \parallel H$ can be expected at a finite critical field H_R (Fig. 5.1). Previous studies by transport ($T \geq 0.5$ K), magnetic torque ($T \geq 0.1$ K) and magnetization ($T \geq 2$ K) measurements indicate that the transition occurs at $\mu_0 H_R \sim 12$ T in URhGe for $H \parallel b$ and becomes first order at low temperature [38, 41, 68, 69]. Fig. 5.3 shows the field variation of the magnetization in a $T = 0$ limit, given by a T^2 extrapolation of the M vs. T data measured above 2 K for $H \parallel b$ in previous magnetization measurements above 2 K [69]. In this figure, the field variation of the magnetization in a $T = 0$ limit exhibits the first order metamagnetic transition at $\mu_0 H_R \sim 12$ T.

The nature of the metamagnetic transition changes from second order transition to first order transition at tricritical point (TCP). The location of the TCP is controversial in this system, because the critical field H_R is very close to the field in which the reentrant superconductivity (RSC) appears (Fig. 5.1), and it has been considered that the magnetic fluctuations on the TCP associated with the moment reorientation are expected to play an essential role of the RSC [38, 39, 68].

The location of TCP has been reported to be ~ 2 K and $4-7$ K by thermoelectric

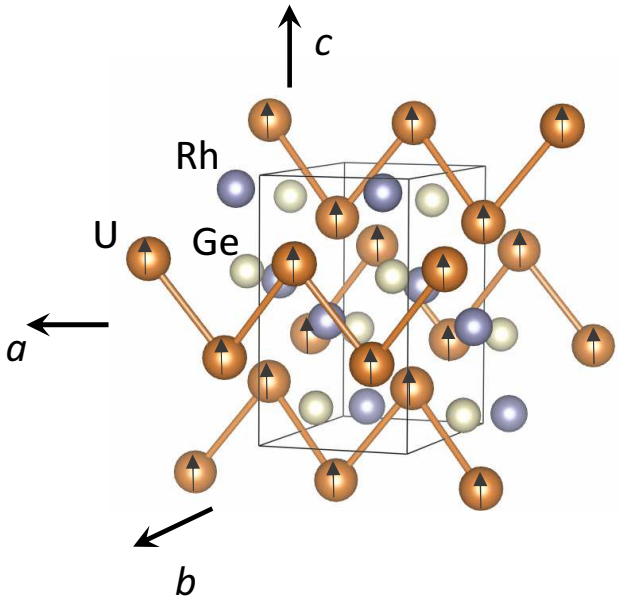

Figure 5.2: Crystal structure of the URhGe.

power [42] and nuclear magnetic resonance (NMR) [43] experiments, respectively. Figure 5.4 shows the schematic phase diagram of URhGe for magnetic fields applied for *bc* plane, given by previous resistivity measurements [71], where T_c is the critical temperature of the RSC. Wing structure, which is planes of ferromagnetic first order transition, appears below the TCP in three dimensional T-H_b-H_c phase diagram [39, 71, 72]. Wing structure is generally observed in clean metal, such as itinerant FM compounds UGe_2 [14–16], $ZrZn_2$ [17], URhAl [19], UCoGa [20], and an itinerant metamagnet UCoAl [24]. However, either high pressure (UGe_2, $ZrZn_2$, URhAl, UCoGa) or negative pressure (UCoAl) is required to tune T_C to zero, making it difficult to observe the magnetization behavior near quantum phase transition. By contrast, URhGe provides a good opportunity to investigate the whole FM phase diagram, i.e. the TCP and the wing structure, because a magnetic field H_b parallel to the *b* axis being the tuning parameter. Remarkably, the zero resistivity region of the RSC at 40 mK exactly overlaps the wing QPT region in the H_b-H_c plane [38, 72], further evidencing the close connection between RSC and the FM QPT. Figure 5.5 shows the field-angle mapping of RSC (black hatched area; zero resistivity area at 40 mK) and first order metamagnetic transition (blue lines with triangles; obtained at 0.5 K) for applied field in the *bc* and *ab* planes, measured by previous resistivity measurements [38]. It should be noticed that the RSC apparently emerges around the first-order FM transition region. Figure 5.6 shows a contour plot of $1/T_2$ at 1.6

K given by previous ^{59}Co NMR measurements in doped system of $URh_{0.9}Co_{0.1}Ge$, and the plot provides a map of the magnetic fluctuation amplitude in the (H_b, H_c) plane around H_R [39]. The result of the previous NMR measurements indicates that FM fluctuations, which caused by a quantum TCP, are enhanced near the wing structure at $\sim$ 1.6 K.

Investigating the location of TCP and the detail of wing structure is very important to reveal the origin of RSC. In phenomenological theory [8], the boundaries of the wing structure, that emerge in a three dimentional phase diagram, have a tangent slope at TCP, suggesting that direct measurements with high precision in-situ alignment of magnetic field are essential to determine the location of TCP and the detail of the wing structure. Up to present, the detail of three dimensional phase diagram of URhGe has not been obtained, and no direct magnetization measurement has been performed in URhGe in the QPT region; field variation of the magnetization in a $T = 0$ limit has been obtained by a T^2 extrapolation of the M vs. T data measured above 2 K for $H \parallel b$ [69]. Note that the further details of the wing structure is already described in Chapter 1.

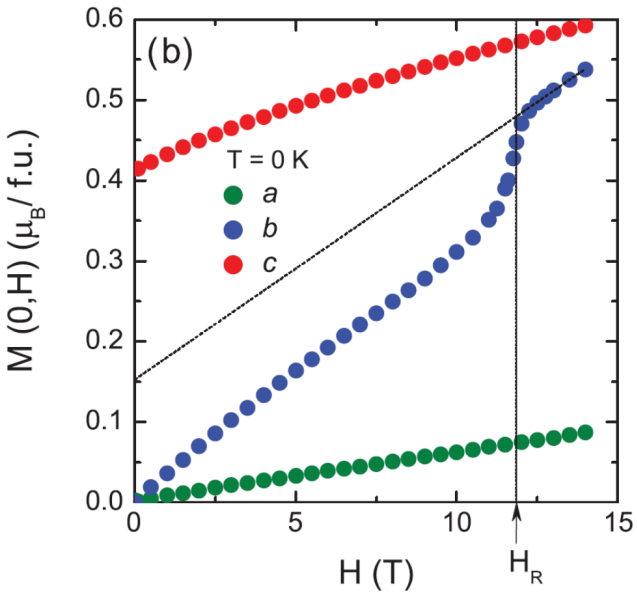

Figure 5.3: The field variation of the magnetization in a $T = 0$ limit has been obtained by a T^2 extrapolation of the M vs. T data measured above 2 K for $H \parallel b$ [69].

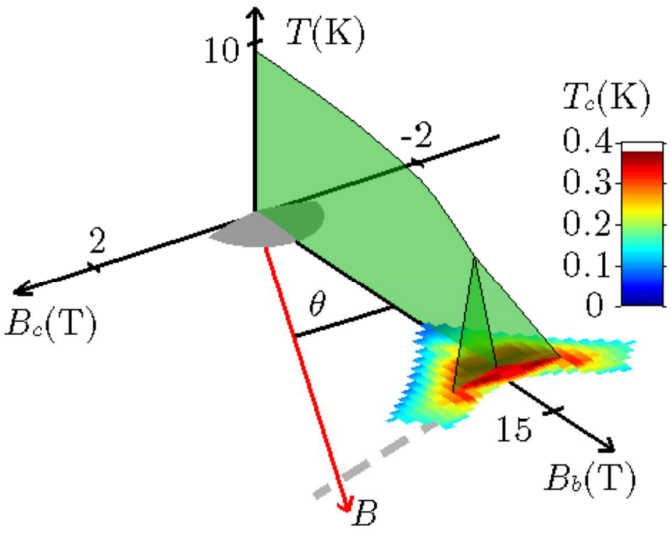

Figure 5.4: The schematic phase diagram of URhGe for magnetic fields applied for *b*-*c* plane, given by previous resistivity measurements [71].

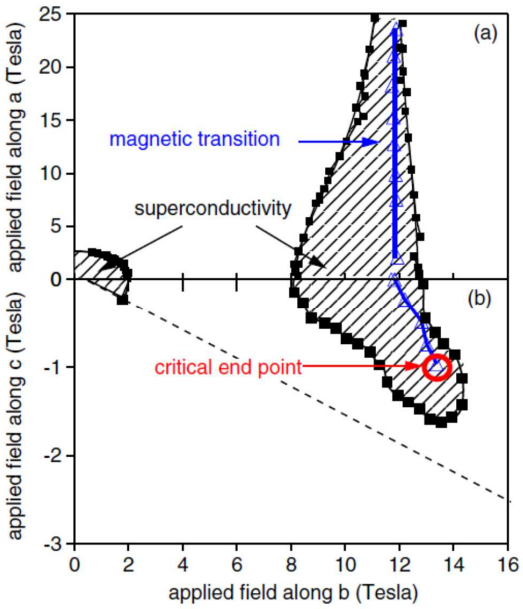

Figure 5.5: The field-angle map of RSC (black hatched area; zero resistivity area at 40 mK) and first order metamagnetic transition (blue lines with triangles; obtained at 0.5 K) for applied field in the *bc* and *ab* planes, measured by previous resistivity measurements [38].

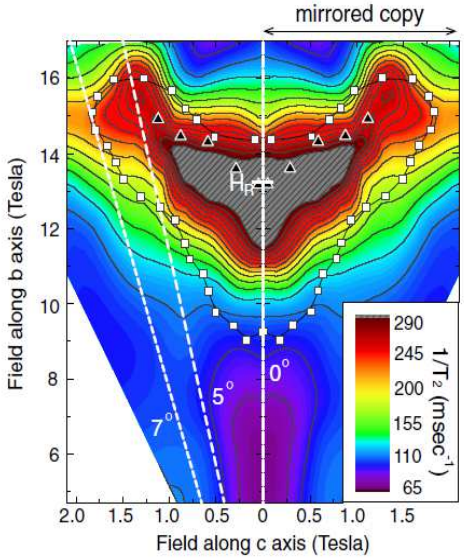

Figure 5.6: Contour plot of $1/T_2$ at 1.6 K given by previous ^{59}Co NMR measurements in $URh_{0.9}Co_{0.1}Ge$, and the plot provides a map of the magnetic fluctuation amplitude in the (H_b, H_c) plane around H_R [39].

5.2 Experimental Procedures

Single-crystalline sample of URhGe was grown and cut into a rectangular shape with dimentions $a \times b \times c = 0.7 \times 1.0 \times 0.5$ mm^3 with 4.4 mg mass at JAEA. The present sample does not exhibit superconductivity. Whereas superconductivity can be observed only in stoichiometric samples of URhGe with a very small residual resistivity [73], the FM transition is much more robust and does not change much even in doped systems $URh_{0.9}Co_{0.1}Ge$ and $URh_xIr_{1-x}Ge$ [39, 74]. It should be noticed, however, that the sample quality might influence the magnetization behavior, in particular at the vicinity of QCPs.

DC magnetization measurements were performed by means of a capacitively-detected Faraday magnetometer [44] (Chapter 2). In this method, we detect a magnetic force ($M_z dH_z/dz$) proportional to the magnetization of the sample situated in an inhomogeneous field as a capacitance change of a capacitive transducer. Here, z denotes the vertical axis, along which the magnetic fields up to 14.5 T were generated by a superconducting solenoid. We applied the field gradient of $G(= dH_z/dz) = 8$ T/m in this experiment. The sample was mounted on the capacitor transducer with varnish (GE7031) so that its b axis is oriented close to the z

direction (Fig. 5.7(a)). The cover of silver foil is also used for strongly fixing the sample as shown in Fig. 5.7(b). In this situation, the b-axis component of the magnetization, M_b, is mainly detected. However, a huge magnetic torque component ($\boldsymbol{M} \times \boldsymbol{H}$) is superposed on the output of the capacitor transducer due to the strong magnetic anisotropy of URhGe. In order to eliminate the torque contribution, we measure the torque back ground with G switched off ($G = 0$), and subtract it from the data with G switched on.

Figure 5.8 shows an example of the data processing, in which the raw capacitance (C) data of URhGe obtained at 0.21 K in magnetic fields tilted by 1.4° from the b axis in the bc plane, are shown (solid circles) with two different field gradient values $G = 8$ T/m and $G = 0$. The magnetization curve (solid squares) can be obtained by taking a difference of the two data. Just at $\theta = 0°$, however, we had a difficulty in subtracting the torque background, as discussed later. The $G = 0$ data is also useful to qualitatively estimate the c-axis component of the magnetization M_c, i.e., the OP of the FM state, under the fields near the b axis.

A ^{3}He-^{4}He dilution refrigerator was used to cool the sample in the temperature range of 0.25 K $\leq T \leq$ 6 K. The orientation of the URhGe crystal was precisely controlled in the bc and ab planes within the experimental accuracy of less than 0.1° using a piezo-stepper-driven goniometer (ϕ rotation) combined with a home-made tilting stage (θ rotation) [54], where ϕ ($-3° \leq \phi \leq 3°$) and θ ($-10° \leq \theta \leq 10°$) are the rotation angle in the ab and the bc planes, respectively (see Chapter 3). Figure 5.9 shows a schematic view of the two-axis rotation device. The two rotation axes, orthogonal to each other, intersect the sample position. The angle of the tilting stage is varied by a screw, which is rotated from the top of the insert with a shaft that is thermally isolated. The full details of the two-axis rotation device will be published elsewhere. In the present study, we measured θ dependence of the magnetic responses in the bc plane ($\phi = 0$ plane). We also checked that the temperature of $T_C \sim 9.5$ K is the same as the present study [69, 75] by using a commercial magnetic properties measurement system (MPMS). Figure 5.10 is $M(T)$ curve of URhGe in a magnetic field of 0.2 T along the b axis obtained by using MPMS.

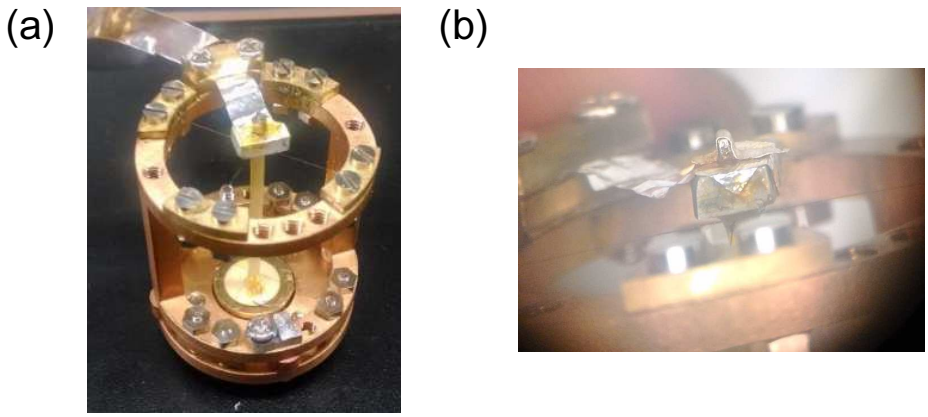

Figure 5.7: Photo of the magnetometer, in which the sample is mounted with varnish (GE7031). The cover of silver foil is also used for fixing the sample as shown in Fig. 5.7(b). The *b* axis of the sample is oriented close to the *z* direction.

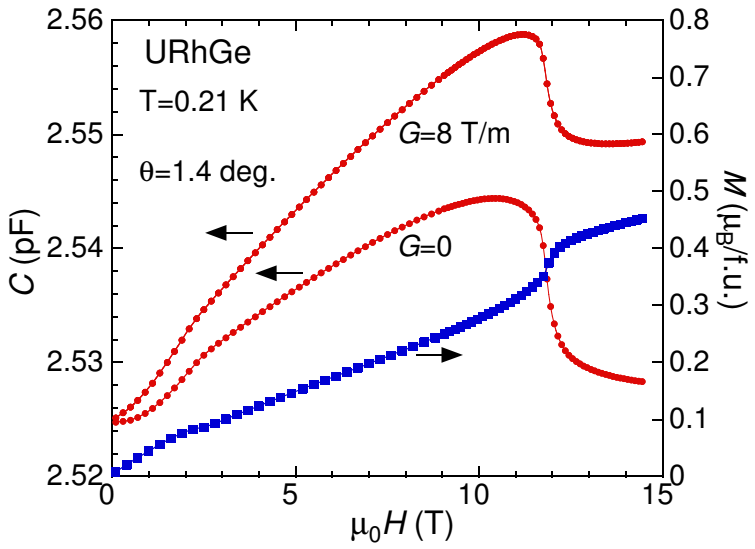

Figure 5.8: Example of the raw capacitance (C) data (solid circles) obtained at 0.21 K in magnetic fields tilted by 1.4° from the *b* axis in the *bc* plane, with the field gradient G = 0 and 8 T/m. Taking a difference of these two yields the magnetization curve (solid squares) [67].

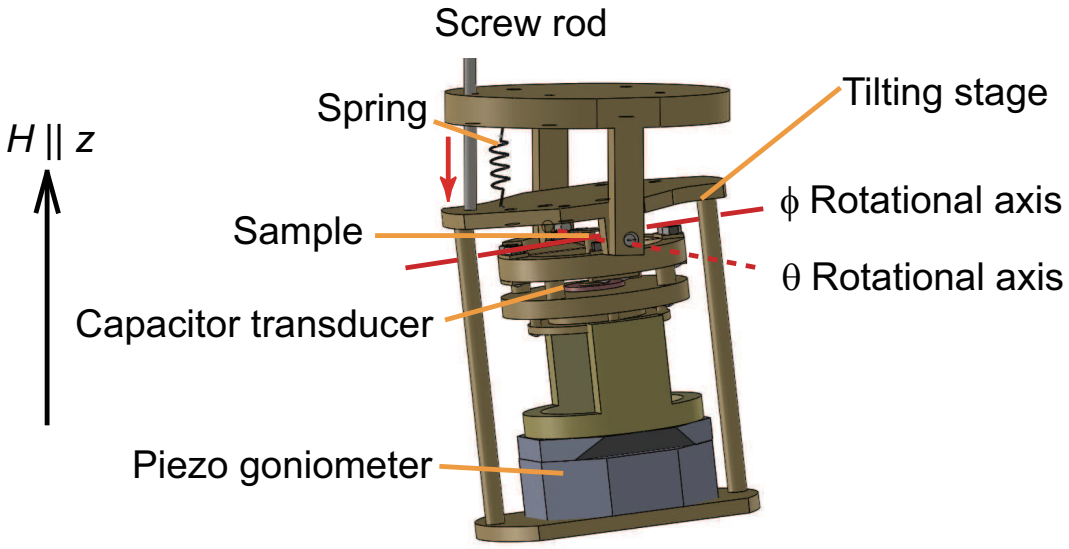

Figure 5.9: Schematic view of the two-axis rotation device. θ and ϕ rotations are performed by a home-made tilting stage and a piezo-stepper-driven goniometer, respectively. The angle of the tilting stage is controlled from the top of the insert by a screw rod that is thermally isolated [67].

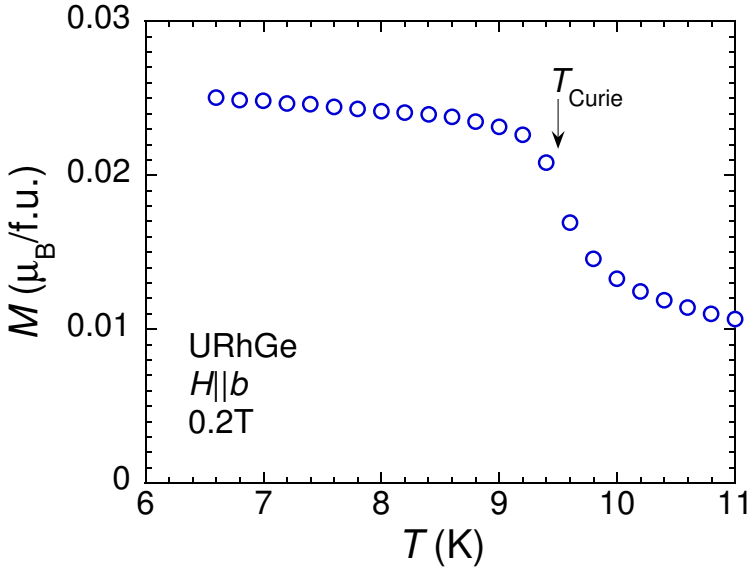

Figure 5.10: $M(T)$ curve of URhGe in a magnetic field of 0.2 T along the b axis obtained by using MPMS. The present value of $T_C \sim 9.5$ K is almost the same as the present study [69, 75].

5.3 Results

5.3.1 Torque component

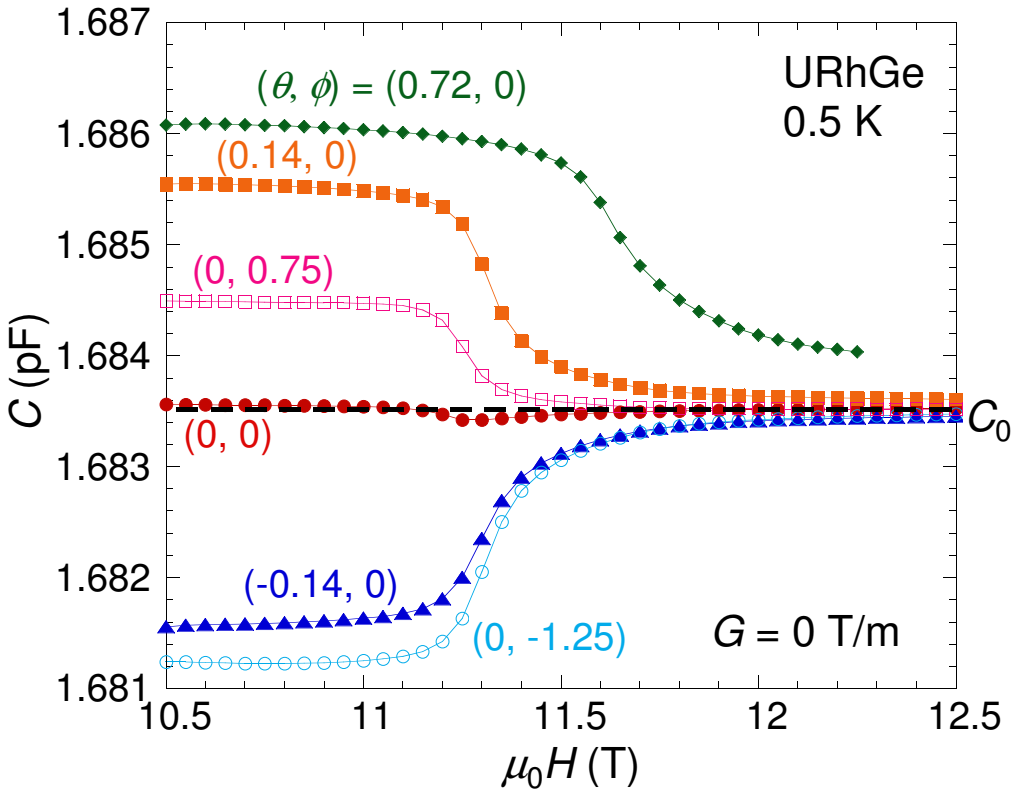

Figure 5.11: The raw capacitance data C of URhGe with field gradient $G = 0$, measured at 0.5 K for the angle $(\theta, \phi) = (0.72, 0), (0.14, 0), (0, 0.75), (0, 0), (-0.14, 0)$, and (0, -1.25), where θ and ϕ are angles (these unit: degree) from the b axis towards the c axis and the a axis, respectively. The black dashed line is the zero torque state, which is realized at $(\theta, \phi) = (0, 0)$. The capacitance value at $H = 0$ is obtained as $C_0 \sim 1.6836$ pF.

In order to precisely adjust the b axis of the sample along the magnetic field direction, we measure the magnetic torque with G switched off, $G = 0$. Figure 5.11 shows the angular dependence of the capacitance C obtained for $G = 0$, measured at 0.5 K for the angle $(\theta, \phi) = (0.72, 0), (0.14, 0), (0, 0.75), (0, 0), (-0.14, 0)$, and (0, -1.25), where the θ and ϕ are angles (in units of degree) from the b axis towards the c axis and the a axis, respectively. The dashed line at $C_0 = 1.6836$ pF indicates the capacitance value at $H = 0$. The capacitance difference $\Delta C_\tau = C - C_0$ is thus proportional to the torque component $\tau = \boldsymbol{M} \times \boldsymbol{H}$. There is a huge torque contribution below the reorientation field $\mu_0 H_R(\theta) \sim$ 12-13 T for $|\theta| \geq 0.14°$ coming from the

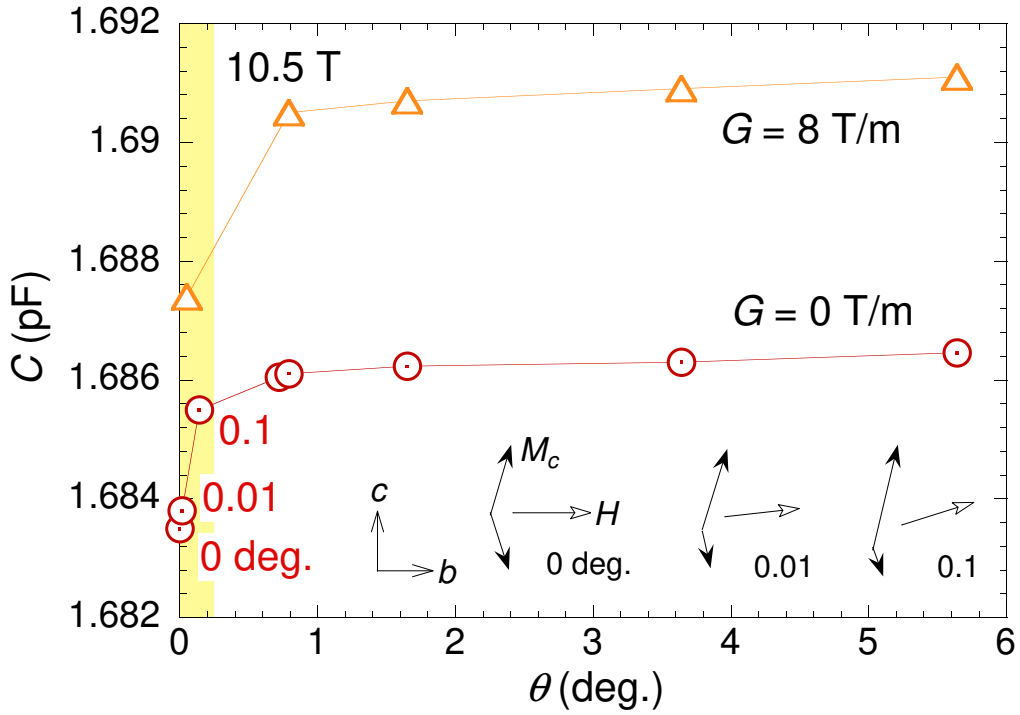

Figure 5.12: The angular θ dependence of the capacitance C with two different field gradient values, $G = 0$ and 8 T/m, obtained at 0.5 K in 10.5 T below H_R. In the yellow hatched region, the torque component changes so dramatically with θ that the precise evaluation of the magnetization becomes difficult. The inset schematically shows the θ-evolution of the FM domains with positive and negative components of M_c (solid arrows) in a magnetic field H (open arrows). There is no bulk magnetization M_c at $\theta = 0°$, and the zero-torque ($\tau = 0$) state persists irrespective of the magnitude of H_b [67].

large M_c component. Interestingly, the $G = 0$ data at $(\theta, \phi) = (0, 0)$, in which the magnetic field direction is precisely adjusted to the b axis, show virtually no torque contribution. This is because a perfect alignment of the magnetic field along the b axis ($H_c = 0$) yields an equal population of the FM domains with M_c pointing along $+c$ and $-c$ directions (the inset of Fig. 5.12), resulting in the zero-torque state even below H_R. The degree of the domain alignment changes with θ, and saturates above 0.79°. Note that the torque changes its sign for a negative θ value, as expected. Above H_R, the torque component almost vanishes for $\theta = 0.14°$, indicating that the magnetic moment becomes almost parallel to the field direction. For $\theta > 0.79°$, on the other hand, a finite torque remains even well above $H_R(\theta)$. This is due to an intrinsic magnetic anisotropy of the system. In Fig. 5.12, we plot the C value at $\mu_0 H = 10.5$ T and $T = 0.5$ K with $G = 0$ (open circles) and $G = 8$ T/m (open

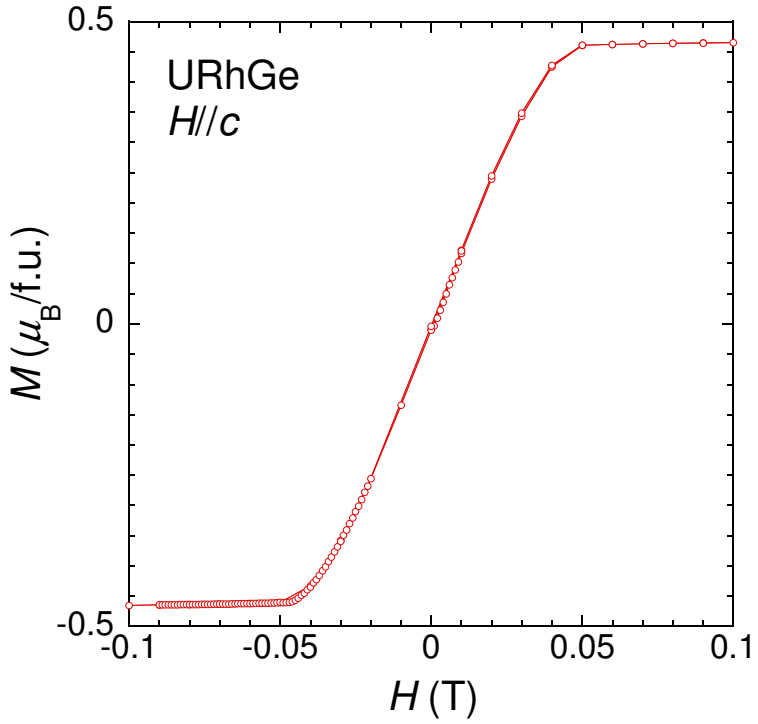

Figure 5.13: M(H) curve in the magnetic field along the c axis. The magnetization saturates above $\mu_0 H_c \sim 0.05$ T.

triangles) for several θ values. The $G = 0$ data represents the domain alignment as a function of the c-axis field $\mu_0 H_c\,[T] = 10.5 \sin\theta$. The data clearly show that the single domain state is reached at $\theta \sim 0.8°$, or $\mu_0 H_c \sim 0.15$ T. Actually, magnetization measurements in the magnetic field along the c axis show that the magnetization saturates above $\mu_0 H_c \sim 0.05$ T (Fig. 5.13) without a hysteresis, suggesting that the single domain state is realized above $\mu_0 H_c \sim 0.05$ T, or $\theta \sim 0.3°$. The value of the magnetic field is almost the same as the one of a demagnetizing field H_d, which is estimated to be ~ 0.03 T by using an equation $H_d = NM/\mu_0$ with $N = 1$. Note that the $M(H)$ curve is obtained by using a commercial magnetic properties measurement system (MPMS), and the residual magnetic field at zero field is much smaller than 0.05 T.

Figure 5.14 shows the field variation of $\Delta C_\tau/H$, the quantity proportional to M_c, measured at (a) 0.25, (b) 3, and (c) 6 K in a field range near H_R for the angles $\theta = 0°$, 0.79°, 1.65°, 3.64°, and 5.64°. The differential curves $d(\Delta C_\tau)/dH$ are also shown in Figs. 5.14(d)-5.14(f). For $\theta = 0°$, the domain state with zero magnetic torque persists up to $\mu_0 H_R(0°) = 11.2$ T, where a small kink appears upon the moment reorientation. For $\theta = 0.79°$ and $T = 0.25$ K, the sudden collapse of $\Delta C_\tau/H$ seen

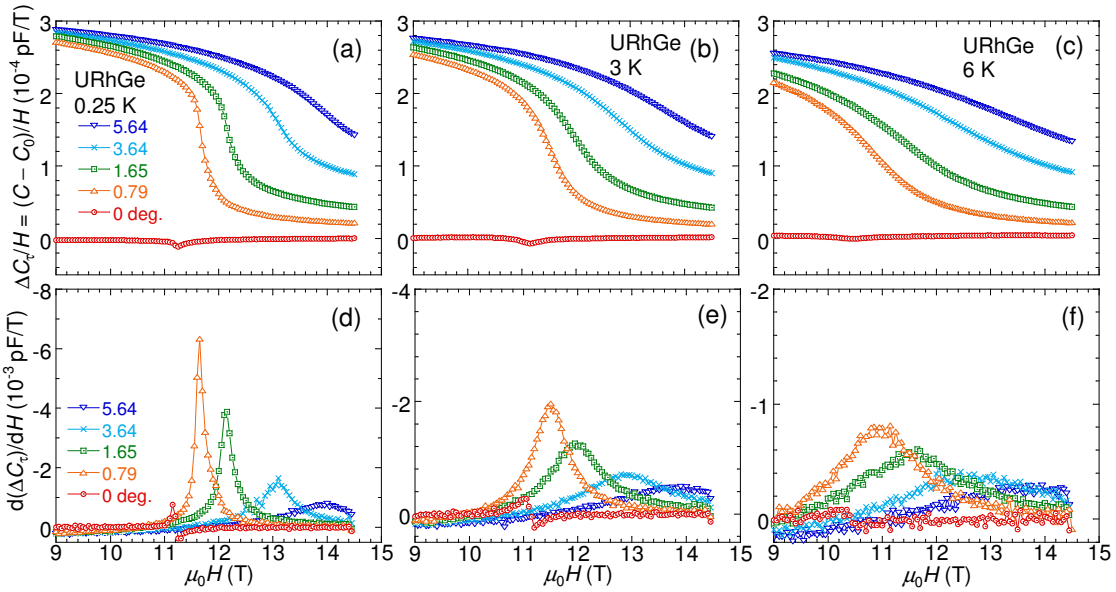

Figure 5.14: Magnetic torque divided by field, $\Delta C_\tau/H$, of URhGe measured at (a) 0.25, (b) 3, and (c) 6 K in fields near $H_R(\theta)$ with θ = 0°, 0.79°, 1.65°, 3.64°, and 5.64°, together with the differential curves $d(\Delta C_\tau)/dH$ ((d)-(f)) [67].

at $H_R(0.79°)$ = 11.7 T indicates a first-order transition. This transition becomes broader and shifts to the higher field side with increasing θ and decreasing T. These features are more clearly seen in the differential data [Figs. 5.14(d)-(f)].

These torque data thus directly probe the behavior of the OP across the transition, and can be used to construct the wing structure phase diagram for $\theta > 0.8°$. As mentioned above, however, the torque component is not so sensitive to the phase transition very close to $\theta = 0°$ because of the domain formation. In order to explore the phase transition for $\theta \approx 0°$, in particular the TCP, we evaluate the field variation of the magnetization in the following.

5.3.2 Magnetization

Magnetization curves for various field angle θ near the b axis can be obtained from the capacitance data with G = 8 T/m by subtracting a torque background (G = 0 data), on the basis of the assumption that the torque contribution is the same for G = 0 and 8 T/m. In most cases, this condition holds with good accuracy. As explained later, however, we found it difficult to fulfill this condition at $|\theta| \lesssim 0.1°$ for a technical problem, and as a consequence some residual torque contribution remains in the magnetization curve at $H \lesssim H_R$ for $\theta \approx 0°$. For this reason, we

denote the magnetization curve at $\theta = 0°$ by $\tilde{M}(H)$, and distinguish it from the $M(H)$ data for $\theta > 0.1°$ for which the torque component is properly subtracted.

Figures 5.15(a) and (b) show $\tilde{M}(H)$ of URhGe and the differential curve $d\tilde{M}/dH$, respectively, obtained at 0.25, 1, 2, 3, 4.2, and 6 K. At 0.25 K, a magnetization jump is observed at $\mu_0 H_R(0) = 11.2$ T. $\tilde{M}(H)$ reaches ~0.46 μ_B/U above H_R, in agreement with the previous result [69]. This magnetization value is very close to the spontaneous magnetization M_c at $H = 0$, in accordance with a simple picture of the moment reorientation from the easy c axis to the b axis at H_R [38, 39, 69]. Just above H_R, there is a small shoulder-like anomaly, which is also seen in $d\tilde{M}/dH$ as a small hump. As shown in the inset of Fig. 5.15(b), a small hysteresis is observed in the transition at 0.25 K, implying the transition to be of first order. With increasing temperature, the magnetization jump becomes broader and weaker, and the critical field shifts to the lower field side. This change of the transition behavior becomes prominent above 2 K. Surprisingly, however, the peak feature in $d\tilde{M}/dH$ can be seen even at 6 K.

In Fig. 5.16, $d\tilde{M}/dH$ at 0.25, 0.5, and 1 K for the increasing- and decreasing-field sweeps are plotted with squares and circles, respectively. A small hysteresis ($\Delta H \sim 30$ mT at 0.25 K) is observed in the two curves, demonstrating a weak nature of the first order phase transition. The hysteresis becomes much smaller with increasing temperature from 0.25 K, and vanishes above 1 K. Figure 5.17(a) shows temperature dependence of $H_R(\theta, T)$ obtained from the present torque and magnetization measurements at $\theta = 0°$, 1.65°, and 3.64°, together with the previous results (dotted line) [24]. Here $H_R(\theta, T)$ is determined by the position of the peak of $d(\Delta C_\tau)/dH$ and $d\tilde{M}/dH$ in Figs. 5.14 and 5.15. The results at $\theta = 0$ is qualitatively the same as the previous reports, and the line of $H_R(\theta, T)$ shifts to the higher field side with increasing the angle θ. More precisely, the critical field of $\mu_0 H_R(0, T < 1 \text{ K}) = 11.2$ T obtained here is slightly lower than the previously reported values [24, 68, 69, 72]. The inset of Fig. 5.17(a) compares the critical field defined in the ascending (open squares) and descending (open circles) fields.

Figures 5.17(b) and 5.17(c) show the temperature evolution of the amplitude of the peak in $d\tilde{M}/dH$ at $H_R(\theta)$ and the transition width defined by the full width at the half maximum, respectively, measured at several θ. A remarkable weakening of the transition is evident above 2 K, the temperature which is close to T_{TCP} reported previously [42]. The transition width for $\theta \geq 0.79°$ shows a significant broadening above 2 K. At $\theta = 0$, by contrast, the transition remains relatively sharp even near 6 K, suggesting that the first-order-like behavior persists up to this temperature.

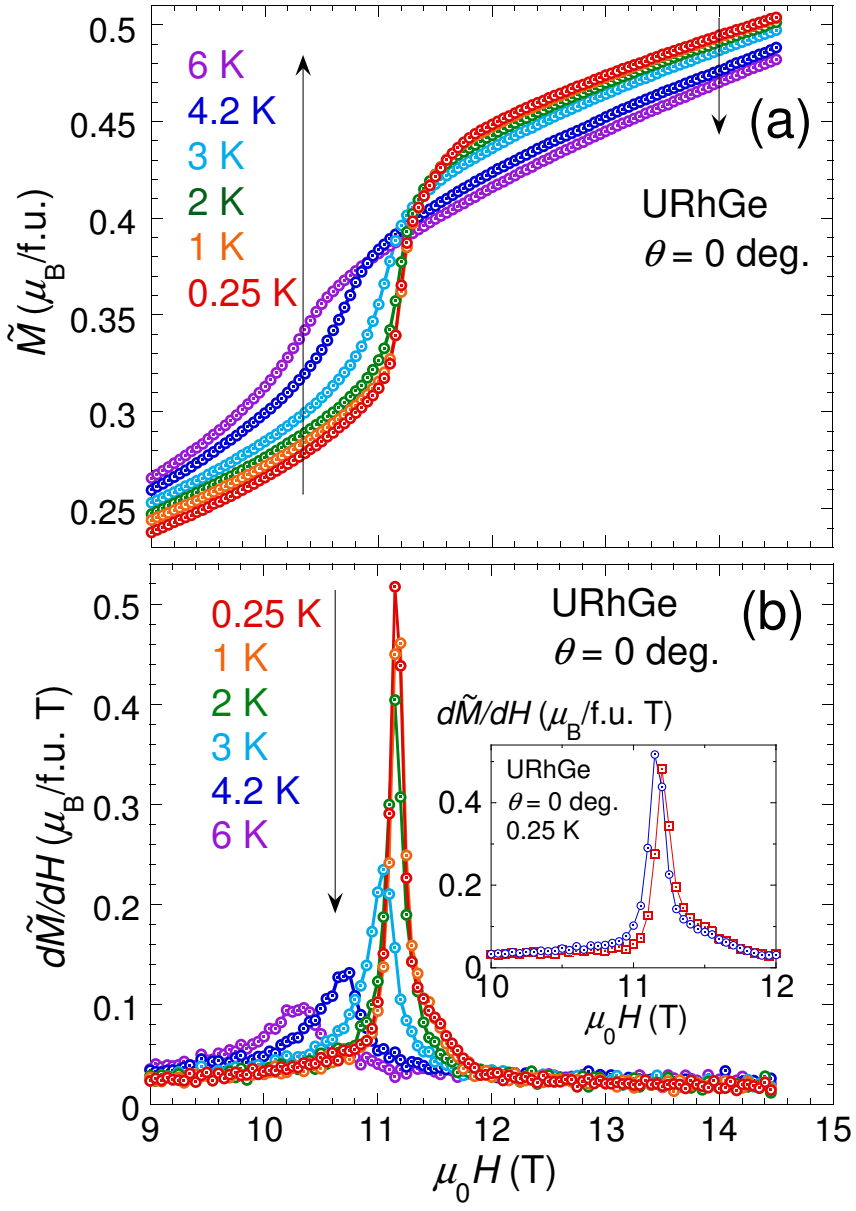

Figure 5.15: (a) $\tilde{M}(H)$ of URhGe measured in the magnetic field along the b axis. (b) The field derivative $d\tilde{M}/dH$ of the magnetization curves in Fig. 5.15(a). In these figures, only the down-sweep traces are plotted for simplicity. The inset of Fig. 5.15(b) shows $d\tilde{M}/dH$ at $T = 0.25$ K and $\theta = 0°$ for both up- and down-field sweeps [67].

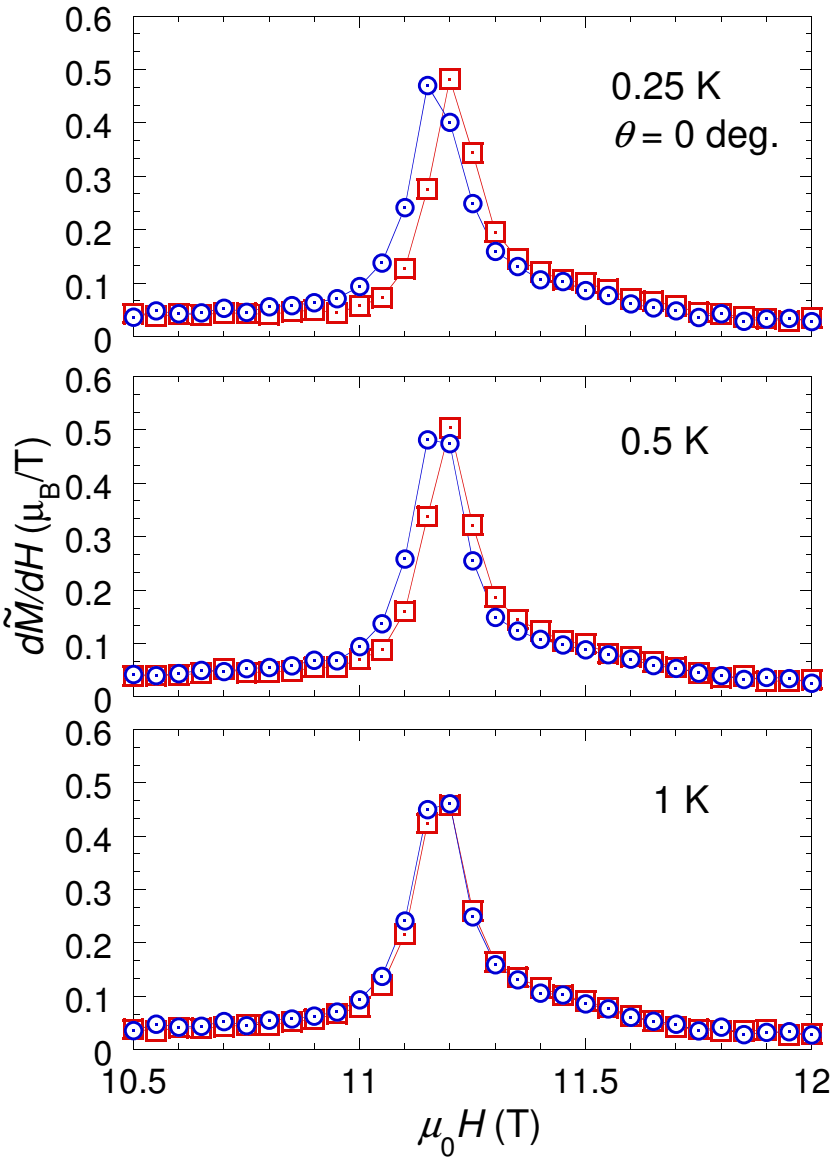

Figure 5.16: The differential curve $d\tilde{M}(H)/dH$ at 0.25, 0.5, and 1 K at $\theta = 0°$, obtained in the magnetic field direction along the b axis. In this figure, both the decreasing-field (circle) and the increasing-field (square) sweeps are plotted, indicating the presence of a small hysteresis at lower temperatures.

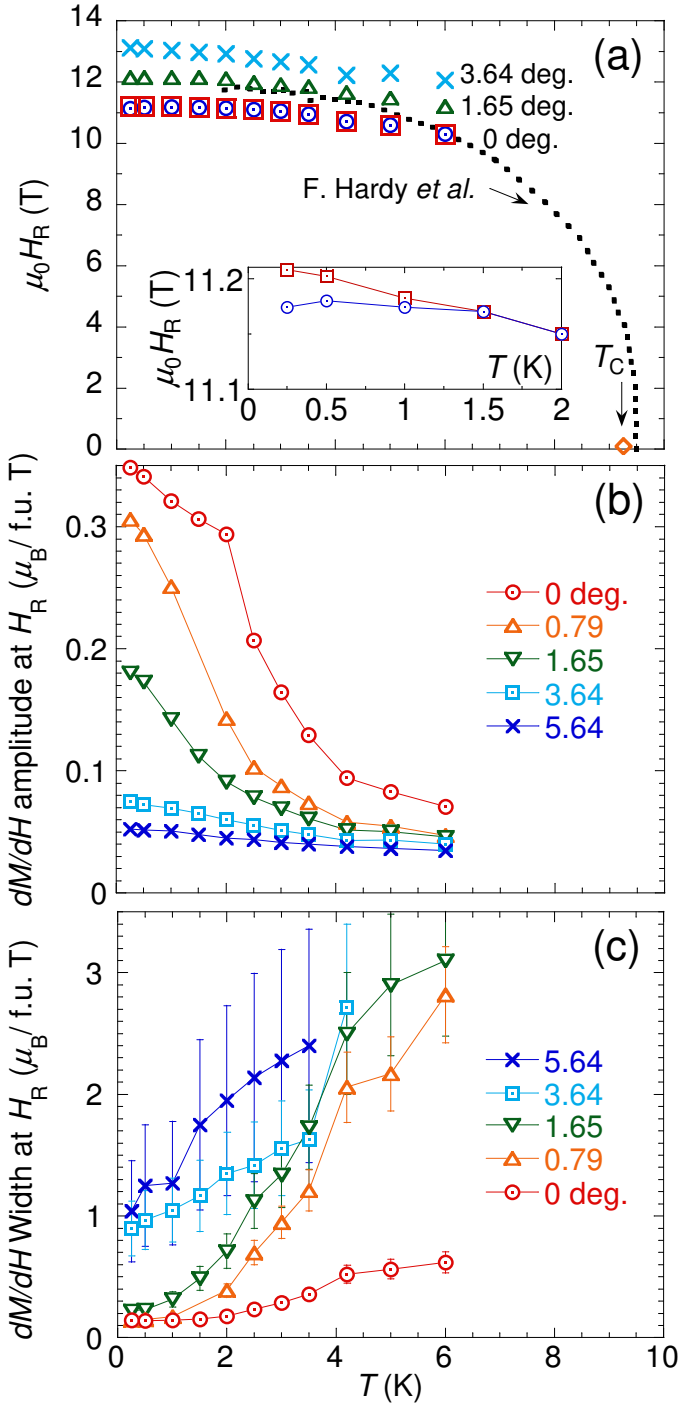

Figure 5.17: (a) Temperature dependence of $H_R(\theta)$ obtained from the present measurements at $\theta = 0°$, 1.65°, and 3.64°, together with the results of the previous study (dashed line) [69]. The inset is an expanded plot for $\theta = 0°$, indicating $H_R(T)$ defined at up-sweep (open squares) and down-sweep (open circles) fields. (b) Temperature evolution of the peak amplitude of $d\tilde{M}/dH$ at H_R, obtained at several θ. (c) Temperature evolution of the transition width, obtained at several θ [67].

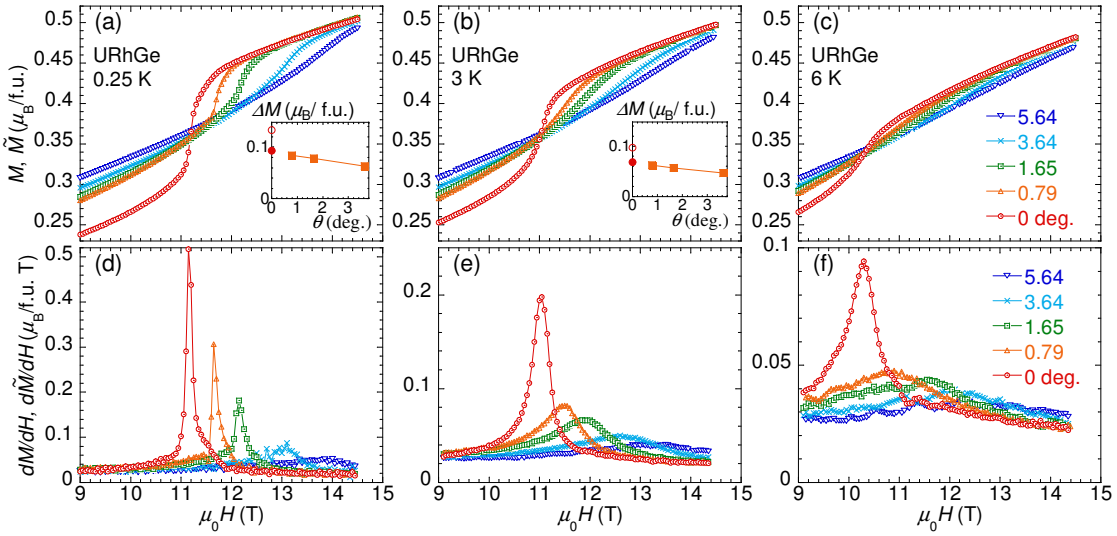

Figure 5.18: The magnetization curves $M(H)$ of URhGe near $H_R(\theta)$ (θ = 0.79°, 1.65°, 3.64°, and 5.64°), measured at (a) 0.25, (b) 3, and (c) 6 K, together with their differential curves dM/dH for (d) 0.25, (e) 3, and (f) 6 K. For comparison, $\tilde{M}(H)$ and $d\tilde{M}/dH$ at $\theta = 0°$ are also plotted. The insets in Figs. 5.18(a) and 5.18 (b) show the angular variation of the magnetization jump ΔM ($\theta \geq 0.79°$, solid squares) measured at 0.25 and 3 K, respectively. The solid circles are the linear extrapolation of ΔM to $\theta = 0°$, which are a factor of 0.7 smaller than $\Delta\tilde{M}$ measured at $\theta = 0°$ [67].

Figure 5.18 shows the magnetization curves $M(H)$ of URhGe near $H_R(\theta)$ for θ values from 0.79° to 5.64° measured at (a) 0.25, (b) 3, and (c) 6 K, together with their differential curves dM/dH for (d) 0.25, (e) 3, and (f) 6 K. Note that the torque component is properly subtracted for the results at $\theta > 0.1°$. Comparing Figs. 5.18(d)-5.18(f) with Figs. 5.14(d-f), one can see that dM/dH shows qualitatively the same behavior with $-d(\Delta C_\tau/H)/dH$; the jump in M_b is correlated to the negative jump in M_c. In particular, both data yield the same critical field $H_R(\theta, T)$.

For comparison, $\tilde{M}(H)$ and $d\tilde{M}/dH$ for $\theta = 0°$ are also plotted in these figures. Whereas $\tilde{M}(H)$ agrees with $M(H)$ for $\theta \geq 0.79°$ at fields above H_R, an apparent disparity is evident below H_R; $\tilde{M}(H)$ appears to be underestimated. We attribute this problem to an incomplete subtraction of the torque component in the $\theta = 0°$ condition. A difficulty is that the vertical field gradient G produces a small c-axis component of the magnetic field on the sample (Chapter 2) and slightly deflects the field angle, accordingly. We estimate the angle shift to be $\sim -0.05°$ at $G = 8$ T/m. Even such a tiny change in θ, however, causes a significant effect at $\theta \approx 0°$ because the torque component for $H < H_R$ shows very strong θ variation there (Fig. 5.12).

As a consequence, the condition of the torque component being independent of G fails, resulting in an incomplete torque subtraction for $H < H_R$ and an overestimate of the magnetization jump.

In order to get a reliable estimation of the magnetization jump for $\theta = 0°$, we plot the metamagnetic jump ΔM for the field direction $\theta = 0.79°$, $1.65°$ and $3.64°$ in the inset of Figs. 5.18(a) and 5.18(b). In both plots, ΔM shows a gradual angular variation, and its linear extrapolation to $\theta = 0°$ gives $\Delta M \sim 0.09\ \mu_B$/f.u. at 0.25 K and $\sim 0.07\ \mu_B$/f.u. at 3 K. One sees that $\Delta\tilde{M}$ for $\theta = 0°$ (open circles) is about 1.5 times overestimated for both $T = 0.25$ and 3 K. In what follows, accordingly, we reduce the peak value of $d\tilde{M}/dH$ by a factor 0.7 in the discussion of the angular variation of the transition. We note that thus corrected amplitude of the magnetization jump at 0.25 K for $\theta = 0°$ is in good agreement with the previous estimate by $T \to 0$ extrapolation of the $M_b(T)$ data [69].

5.4 Discussion

We employ these data of dM/dH and $d(\Delta C_\tau)/dH$ for construction of the URhGe wing structure phase diagram. As $H(\theta)$ passes through the first-order wing plane at a fixed T in the $T - H_b - H_c$ phase diagram (Fig. 5.21(c)), dM/dH as well as $|d(\Delta C_\tau)/dH|$ exhibit a peak. Mapping those peak positions to the $T - H_b - H_c$ space then provides the wing phase diagram. Figure 5.19 shows the contour plot of dM/dH around the FM wing structure of URhGe in the H_b-H_c plane at various temperatures. Dotted lines indicate the traces of the field sweep at fixed angles θ, along which the magnetization data were obtained. Green dots on the contour plots represent the peak position of dM/dH measured at $\theta = 0°$, $0.79°$, $1.65°$, $3.64°$, and $5.64°$, and solid lines are guides to the eye. One can see that the bright arc in Fig. 5.19, i.e., the first-order transition region, becomes narrower as T increases. Above 4.2 K, the bright spot can only be seen at $H_c = 0$, indicating the first-order transition is confined to the narrow region. Similar plots can also be obtained from the $d(\Delta C_\tau)/dH$ data and the results are shown in Fig. 5.20. Note that the data points are absent at $H_c = 0$ in Fig. 5.21(b) because the torque component vanishes there due to a ferromagnetic domain formation. These plots thus represent cuts of the wing plane at various temperatures (Fig. 5.21(c)), indicating that the wing planes are slightly warped.

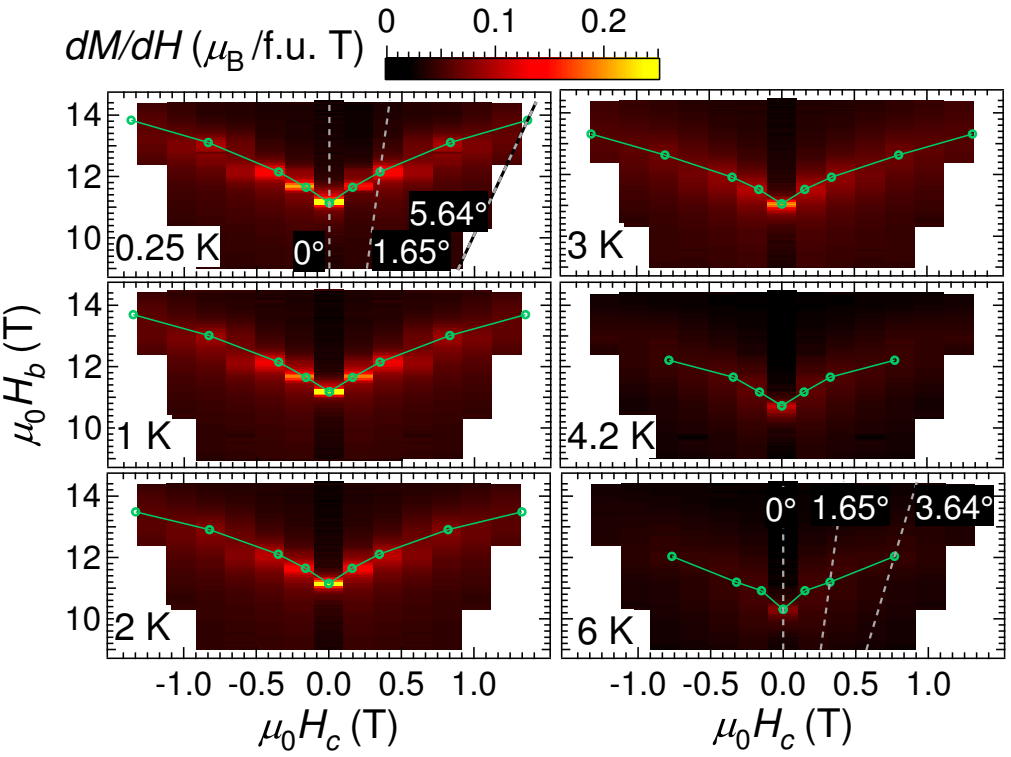

Figure 5.19: The contour plot of dM/dH near the FM wing structure of URhGe in the H_b-H_c plane for various temperatures 0.25, 1, 2, 3, 4.2, and 6 K. Green dots represent the peak position of dM/dH obtained at θ = 0°, 0.79°, 1.65°, 3.64°, and 5.64°, and the green solid lines are guide to the eye. Mirrored copy data are plotted for $\theta < 0°$ [67].

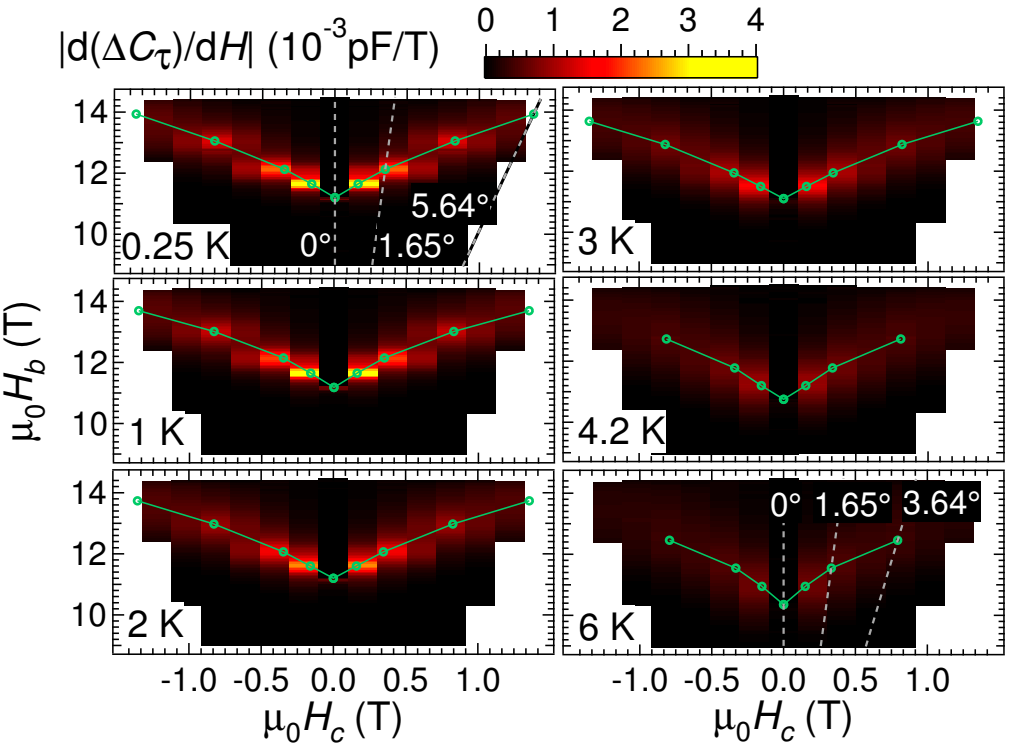

Figure 5.20: The contour plot of $|d(\Delta C_\tau)/dH|$ near the FM wing structure of URhGe in the H_b-H_c plane for various temperatures 0.25, 1, 2, 3, 4.2, and 6 K. Green dots represent the peak position of $|d(\Delta C_\tau)/dH|$ obtained at θ = 0°, 0.79°, 1.65°, 3.64°, and 5.64°, and the green solid lines are guide to the eye. Mirrored copy data are plotted for $\theta < 0°$ [67].

Figure 5.21 shows the color contour plot of the peak amplitude of (a) dM/dH and (b) $|d(\Delta C_\tau)/dH|$, projected on the $T - H_c$ plane. These plots provide imaging of the wing plane viewed from the H_b axis. Overall, the wing plane is bell shaped and steeply extends to higher temperatures above ∼4 K at $H_c = 0$. This feature of the wing plane is in agreement with the phenomenological analysis that three second-order transition lines meet at TCP tangentially [8].

In a prototypical ferromagnet, a first-order transition changes into a second-order one at the edge of the wing plane. One therefore expects that $|d(\Delta C_\tau)/dH(\theta)|$, the field derivative of the OP, becomes divergent on the line connecting TCP and QWCP [8]. Unlike the expectation, however, the peak amplitude of $|d(\Delta C_\tau)/dH(\theta)|$ of URhGe decreases progressively as θ increases, making it somewhat difficult to define the wing edge from these data. This observation, along with the smallness of the hysteresis in H_R, demonstrate the weak nature of the first-order transition in this compound. Nevertheless, from Fig. 5.21(b) we may judge that the wing plane extends to $\mu_0 H_c$ ∼1.1 T at $T \to 0$, because outside this range the landscape of $|d(\Delta C_\tau)/dH(\theta)|$ becomes suddenly flat and low. Thus the location of QWCP is estimated to be $\mu_0 H_c$ ∼1.1 T and $\mu_0 H_b$ ∼13.5 T.

Similar difficulty exists in the determination of TCP. Since $|d(\Delta C_\tau)/dH(\theta)|$ has poor sensitivity to detect TCP at $\theta = 0$ ($H_c = 0$) because of the ferromagnetic domain issue, we inspect the dM_b/dH data. One should keep in mind that M_b is not the OP of the phase transition under consideration. We therefore need some theoretical inputs to discuss the phase transition by the dM/dH data near $\theta = 0°$. Up to now, no established microscopic theory is at hand for the field-induced phase transition in URhGe. We thus rely on the phenomenological model [76] that treats the phase transition of an Ising ferromagnet in a magnetic field perpendicular to the spontaneous magnetization. According to the theory, M_b can be expressed in terms of M_c as

$$M_b = \frac{H_b}{2(\alpha + \beta M_c^2)}, \tag{5.1}$$

where α and β are the coefficients of the M_b^2 and the $M_c^2 M_b^2$ terms in the Landau free energy expansion, respectively. A first-order spin reorientation transition is predicted by this model when β exceeds a certain critical value [76]. As described in the next paragraph, we can see from this equation how dM_b/dH_b at the transition evolves with T in the $T - H_b$ plane; dM_b/dH_b diverges at the transition for $T \leq T_{TCP}$, whereas it does not for $T > T_{TCP}$.

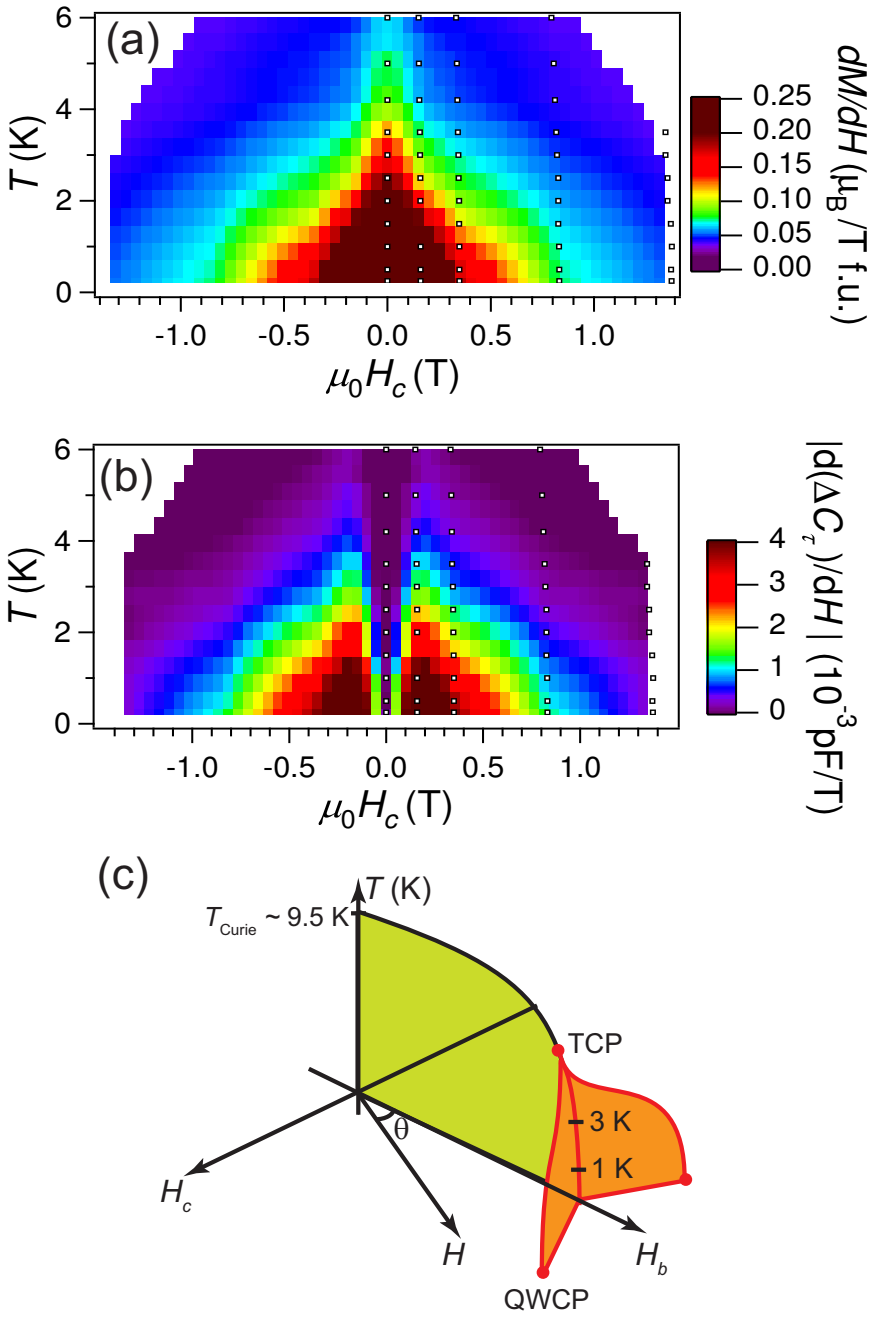

Figure 5.21: The color contour plot of the peak amplitude of (a) dM/dH and (b) $|d(\Delta C_\tau)/dH|$, projected on the $T - H_c$ plane. These plots give imaging of the wing plane, viewed from the H_b axis. These plots are constructed from the data obtained at $T = 0.5$, 1.5, 2.5, 3.5, and 5 K (not shown), in addition to those given in Figs. 5.19 and 5.20. The white dots in these figures show the data points from which the color mappings are generated. A schematic $T - H_b - H_c$ phase diagram is given in (c) [67].

At a second-order transition point above TCP, M_c on the $H_c = 0$ plane develops as $M_c \propto \sqrt{T_C(H_b) - T}$, where $T_C(H_b)$ is given by

$$T_C(H_b) = T_C(0) - A\beta H_b^2, \tag{5.2}$$

with A being a constant [76]. Even though M_c shows an infinite change of slope at $T_C(H_b)$, dM_b/dH_b does not exhibit a strong singularity; from Eqs. (1) and (2), M_b would only exhibit a finite change of slope as a function of T or H_b. This feature of $M_b(T)$ can indeed be seen in the magnetization data measured in various fields H_b [69]. By contrast, just at $T = T_{TCP}$, $M_c \propto (T_C(H_b) - T)^{1/4}$ because the M_c^4 term in the renormalized free energy vanishes. In this case, dM_b/dH_b would diverge as $(T_C(H_b) - T)^{-1/2}$ because a square-root singularity remains in M_b. Below TCP, dM_b/dH_b diverges as well, reflecting a finite jump of M_c at the first-order transition.

By looking at the dM/dH contour plot in Fig. 5.21(a), we find that the peak amplitude for $\theta = 0°$ becomes progressively smaller with increasing T above 2 K. It can be seen, however, that dM_b/dH_b in Fig. 5.18(f) still exhibits a rather sharp peak, i.e. divergent behavior, at 6 K. This fact suggests that the first-order nature of the transition persists up to this temperature. We note that this important feature of the transition is observable only in a very narrow angular window of $|\theta| < 0.8°$.

Up to now, there have been a few reports regarding the location of TCP in URhGe. In the ^{73}Ge NMR spectra study performed in a field of 12 T applied parallel to the b axis, a phase separation of the FM and the paramagnetic states, the fingerprint of the first-order transition, can be seen at least up to 4.3 K, giving rather strong evidence that T_{TCP} is well above this temperature [43]. By contrast, the thermoelectric power experiment claims much lower TCP temperature of 2 K [42]. The wing structure phase diagram (Fig. 5.21) obtained in the present experiment is consistent with the NMR results. It should be noticed that a misalignment of the magnetic field by $\sim 1°$ from the b axis would yield an incorrect estimate of $T_{TCP} \lesssim 3$ K.

Finally, some remarks are made regarding RSC in URhGe. The RSC in this system emerges not only near the quantum wing critical point, but also along the first-order quantum phase transition line of the wing structure at $T = 0$. Indeed, the zero-resistivity state of RSC at 50 mK occurs along the first-order transition line in the $H_b - H_c$ plane, terminating at QWCP [68]. A possible origin of this unusual phenomena has been attributed to longitudinal ($\| b$) magnetic fluctuations, and discussed in relation to a quantum TCP that can be expected when T_{TCP} is very low [38, 39, 68]. The present results reveal, however, that there is a large disparity between $T_{TCP} > 4$ K and $T_{RSC} \approx 0.42$ K; $T_{TCP}/T_{RSC} \gtrsim 10$, indicating that the effect

of the fluctuation of a TCP on RSC may be smaller than expected in Ref. [76]. In this regard, we point out that the first-order transition in this system is very weak in nature, as evidenced by a smallness in the hysteresis of the critical field as well as a rapid broadening of the transition with T. Such a weakness of the first-order transition might host substantial fluctuations even at low temperatures $T \ll T_{\rm TCP}$.

5.5 Summary

We have investigated the quantum phase transition of an Ising ferromagnet URhGe by means of high-precision angle-resolved dc magnetization measurements in magnetic fields applied near the b axis. A first-order spin reorientation transition has been observed at low temperatures, accompanied by a small hysteresis in the critical field. The temperature and angular variations of the transition observed in the magnetization as well as in the magnetic torque allow us to construct the three-dimensional $T - H_c - H_b$ phase diagram, where H_c ($\parallel c$) is the conjugate field parallel to the order parameter and H_b is the b-axis component of the field that tunes $T_{\rm C}$ down to zero. The tricritical point $T_{\rm TCP}$ is estimated to be located above 4 K in the $H_c = 0$ plane. On cooling below $T_{\rm TCP}$, a wing structure develops by increasing $|H_c|$. We have succeeded in directly determining the detailed profiles of the wing structure. The quantum wing critical points exist at $H_c = \pm 1.1$ T and $H_b = 13.5$ T. Three second-order transition lines meet at $T_{\rm TCP}$ tangentially, so that a precise tuning of H along the b axis within 0.8° is needed to correctly determine the position of TCP. The reentrant superconductivity in this system is not due to a quantum TCP [72], but is rather related to unusually weak nature of the first-order transition represented by a smallness of the hysteresis and a broadness of the transition.

Chapter 6

Specific heat and magneto-caloric effect measurements in URhGe

6.1 Motivation

Present angle-resolved magnetization measurements in Chapter 5 suggest that the tricritical point T_{TCP} has been estimated to be located above 4 K on the $H_c = 0$ plane. First order nature (a hysteresis of magnetization curve), however, is observed only below 1 K. The purpose of present angle-resolved specific heat and magneto-caloric effect measurements in URhGe is to decide the location of TCP and to investigate the wing structure in other thermodynamic quantity measurement. In magneto-caloric effect measurements, a first order transition is expected to be clearly distinguished with a second order one.

6.2 Experimental procedure

Single-crystalline sample of URhGe was prepared in JAEA (Tokai) and cut into a rectangular paralelepiped with a weight of 4.4 mg. In this measurements, we used the same sample as the one used in the magnetization measurements in Chapter 5. Vanish (GE7031) is used to mount the sample for the specific-heat cell.

In order to measure angle-resolved specific heat and magneto-caloric effect in URhGe, we improve the two-axis rotation device in Chapter 3. Figures 6.1(b) and 6.1(c) show photos of newly-developed specific heat cell installed to two axis rotation device. For comparison, a photo of the two axis rotation device with magnetometer is shown in Fig. 6.1(a). The magnetometer which surrounded by dotted lines in Fig. 6.1(a) have been easily replaced by the specific-heat cell which con-

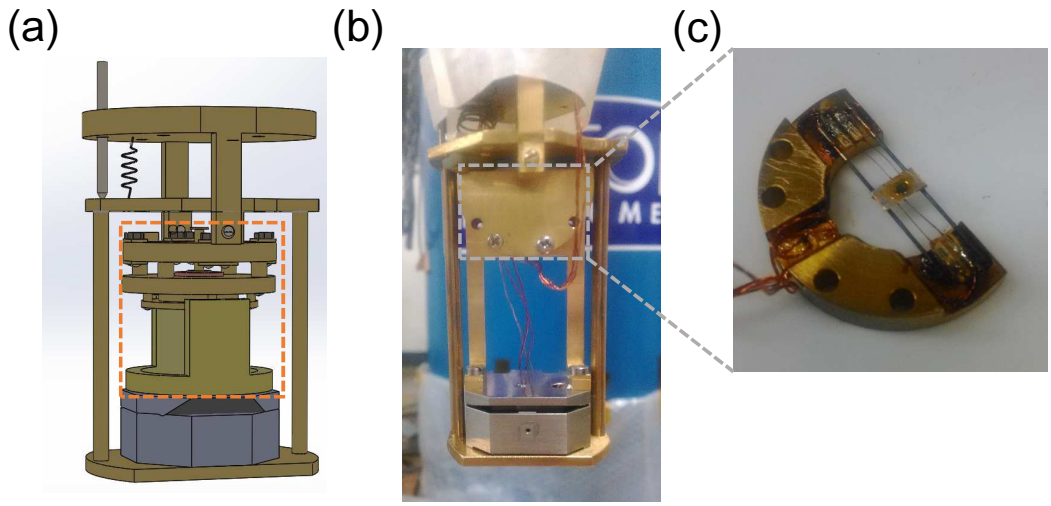

Figure 6.1: (a) Magnetometer (surrounded by dotted lines) installed in the two-axis rotation device. (b) Specific-heat cell (surrounded by dotted lines) installed in the two-axis rotation device. In order to reduce influence of thermal radiation, a cover is attached to the cell. (c) A photo of the newly-developed specific-heat cell. Further detail of the cell is shown in Chapter 2.

nected to piezo-goniometer stage in Fig. 6.1(b). Specific heat and magneto-caloric effect measurements have been performed by using the same setting which shown in Figs. 6.1(b) and 6.1(c), and it is possible to measure these two continuously at low temperatures.

In order to cool the sample in the temperature range of 1 K $\leq T \leq$ 10 K, a ^{3}He-^{4}He dilution refrigerator has been used. The orientation of the URhGe crystal has been precisely controlled in the *bc* and *ab* planes within the experimental accuracy of less than 0.1° using a piezo-stepper-driven goniometer (ϕ rotation) combined with a home-made tilting stage (θ rotation) [54], where ϕ ($-3^\circ \leq \phi \leq 3^\circ$) and θ ($-10^\circ \leq \theta \leq 10^\circ$) are the rotation angle in the *ab* and the *bc* planes, respectively (see Chapter 3).

6.3 Results and Discussion

6.3.1 adjustment of magnetic filed angle

Present magneto-caloric effect (MCE) measurements have been performed under the condition that the resistance value of the resistance thermometer was constant. Monotonous temperature increase and decrease are due to the magnetic field dependence of the resistance thermometer, and the information of the FM spin-reorientation transition appears in non-monotonic temperature change, such as a peak, a dip, and linear bending.

We have adjusted the magnetic field angle by measuring MCE at several θ, where θ is an angle from the b towards the c axes. Figure 6.2 shows θ dependence of MCE of URhGe at 1.5 K, measured at $\theta = 0°, 0.28°, 0.42°$ and $1.01°$. For simplicity, field-up sweeps are only plotted in this figure. The origin of θ ($\theta = 0°$) is decided by the position of the local minimum of a dip. With increasing $|\theta|$, the position of the dip shifts to higher magnetic fields, and it is almost the same as the critical fields which are determined by the present magnetization measurements in Chapter 5.

Field-up and field-down sweeps of MCE, measured at 1.5 K and $\theta = 0°$, are shown in Fig. 6.3(a). The position of local maximum of the peak in field-down sweep is almost the same as the location of local minimum of the dip, suggesting the critical field does not depend on the sweep direction. We assume that MCE can be neglected at a sufficiently high magnetic field than the critical magnetic field, implying that the temperatures of field-up and field-down sweeps match at highest field if the highest field is enough high. In present MCE study, the temperature shift from a temperature $T_{H_{max}}$ at highest field is plotted. The critical magnetic field is determined by the onset of the peak (dip), at which the temperature of field-up and field-down sweeps are separated. In this figure, the critical field is $\mu_0 H \sim 11.6$ T. Figures 6.3(b) and 6.3(c) are calculated MCE results which exhibit first-order and second-order transitions, respectively, where relaxation time $\tau \sim 20$ sec., field-sweep rate $\dot{H} \sim 0.0027$ T/sec. When the transition is of first order, MCE exhibits a peak (a dip) in this situation. By contrast, MCE only shows a linear bending for a second order transition. This calculation clearly shows that all of MCE in Fig. 6.2 exhibit first order transitions.

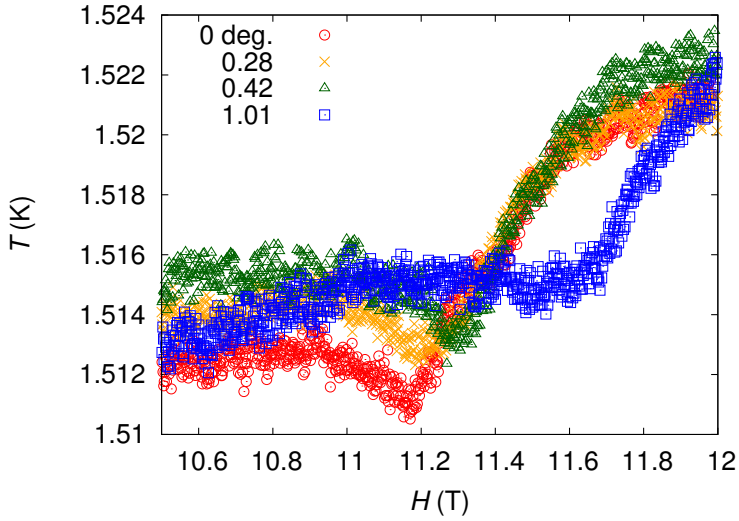

Figure 6.2: θ dependence of MCE of the URhGe at 1.5 K, measured at θ = $0°, 0.28°, 0.42°$ and $1.01°$, where θ is an angle from the b towards the c axes. For simplicity, field-up sweeps are only plotted in this figure.

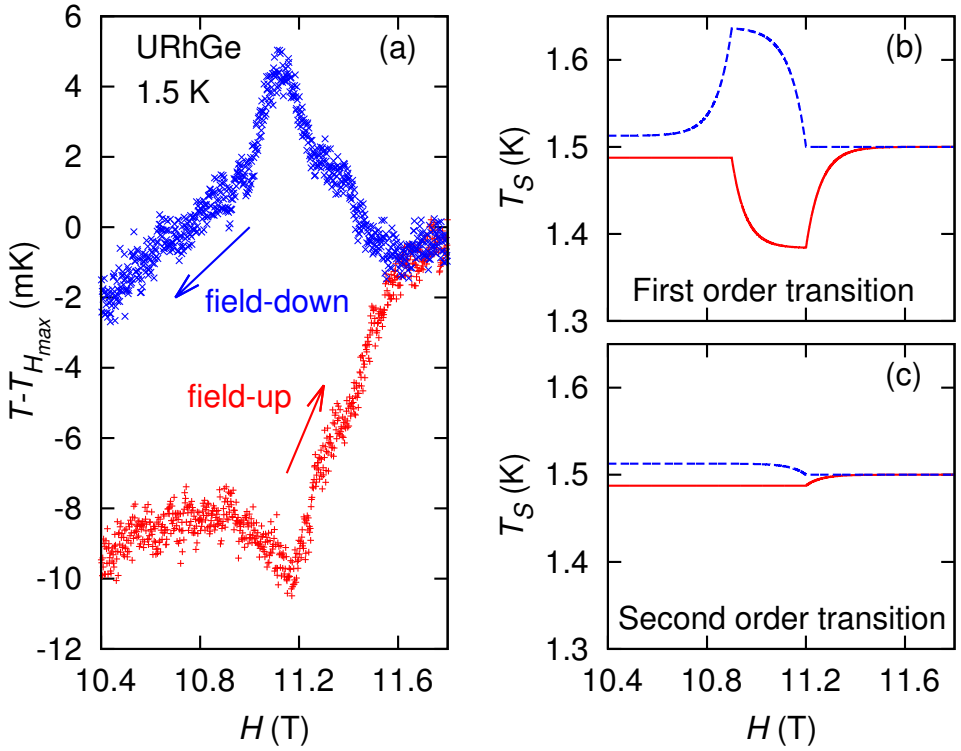

Figure 6.3: MCE measured at 1.5 K and $\theta = 0°$. In this figure, not only a field-up sweep but also a field-down sweep are shown.

6.3.2 specific heat and magneto-caloric effect measurements

Figures 6.4 shows the θ dependence of MCE at 1.5 K, measured at several θ. In this figure, field-up (red) and field-down (blue) sweeps are plotted. The value of resistivity of thermometer is kept constant during a sweep of MCE measurements, and it causes monotonic and linear increase of temperature. First order transition, where MCE exhibits a dip (a peak), can be clearly observed for $|\theta| \leq 1.01^\circ$ in Fig. 6.4. Dotted lines in this figures show the location of the critical field determined by the onset. The transitions in MCE become broader and shift to higher fields with increasing θ, and these behavior is in good agreement with present magnetization measurements in Chapter 5. At $\theta = 3.86^\circ$, the boarding of the transition make it difficult to decide the order of the transition. Note that the rest data of the θ dependence of MCE measured at 1, 2, 2.5, 3 K are shown in Appendix A.

Figure 6.5 shows the θ dependence of specific heat $C(H)/T$ at 1.5 K, measured at several θ. Numbers in parentheses represent offset of C/T. The position of local maximum is almost the same as the one of MCE at all θ. With increasing θ, a peak of C/T becomes broader, and it is a good agreement with present MCE and magnetization measurements.

Temperature variation of MCE at $\theta = 0^\circ$, obtained at 1, 1.5, 2, 2.5, and 3 K. In this figure, field-up (red) and field-down (blue) are plotted. Even at 2-3 K, MCE shows a first order behavior, i.e. a peak (a dip). In present magnetization measurements (Chapter 5), a hysteresis of magnetization curve appears only below 1 K. The first order nature, however, can be observed below 3 K in MCE measurements, suggesting that the transition is of first order even in high temperature region, in which a hysteresis of magnetization curve disappears. This result indicates that TCP locates above 3 K at least. Unfortunately, above 3 K, the signal-to-noise ratio of MCE becomes lower, and it is hard to determine the order of the transition from MCE measurements.

We have also measured the temperature variation of $C(H)/T$ at $\theta = 0^\circ$, measured at 1.5, 3, 4, 5, 6, 6.5, and 7 K (Fig. 6.7). With increasing temperature, the transition shifts to lower fields, and the peak of $C(H)/T$ becomes larger because of increase of lattice specific heat. The shape of the $C(H)/T$ peak does not change at any temperature between 1.5 and 7 K, suggesting that the tricritical point, at which the transition changes from second order transition to first order transition, may locate at higher temperature $T \geq 7$ K. In order to search the tricritical point, we have measured magnetic field variation of $C(T)/T$ at $\theta = 0^\circ$, obtained in the field of 0, 2, 4, 6, and 8 T (Fig. 6.8). Numbers in the parenthesis in this figure mean offsets

of C/T value. The transition remains qualitatively unchanged between 0 and 8 T. $C(H)/T$ and $C(T)/T$ curves suggest that there is no obvious switching point from second order transition to first order transition.

Figure 6.9 shows H-T phase diagram obtained by specific heat measurements of $C(H)/T$ sweep (blue square) and $C(T)/T$ sweep (red circle). These points are determined by the position of the peaks at the transition, and the phase boundaries obtained by $C(H)/T$ and $C(T)/T$ are smoothly connected near 7 K and 8 T. The critical fields and temperatures locate at almost the same place the ones decided by magnetization measurements (Chapter 5). Note that extrapolation values of resistivity is used for resistivity thermometer above 4 K, and it may cause temperature error less than 0.5 K at the highest temperature.

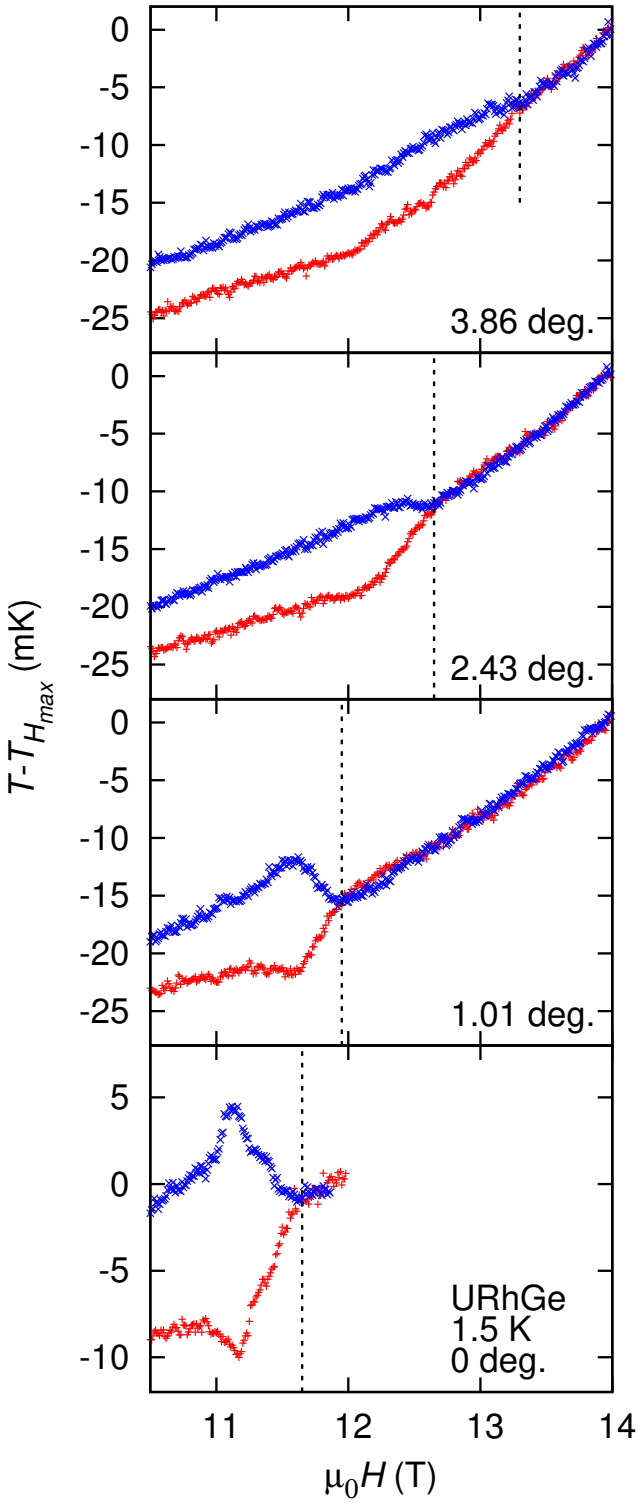

Figure 6.4: θ dependence of MCE of URhGe at 1.5 K, measured at θ = $0°, 0.42°, 1.01°$ and $3.86°$, where θ is an angle from the b towards the c axes. In this figure, not only field-up (red) but also field-down (blue) are plotted.

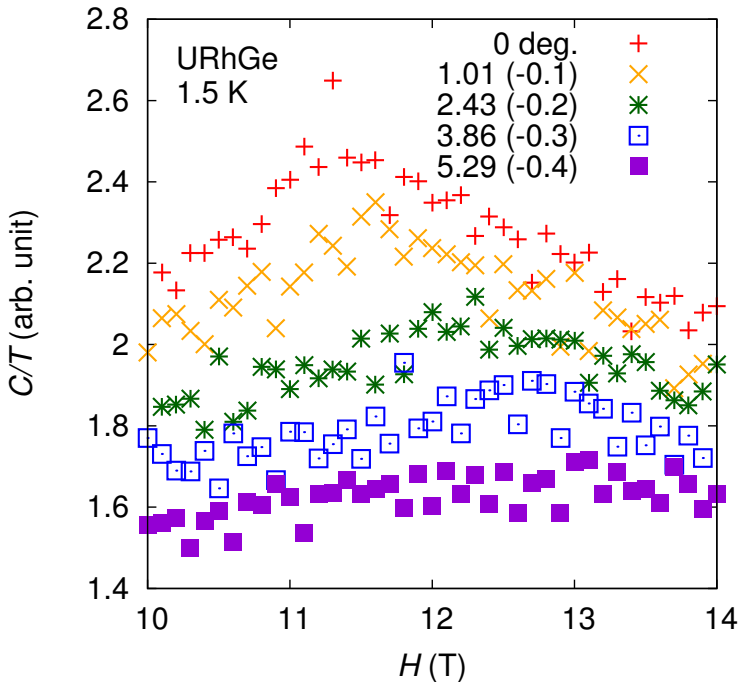

Figure 6.5: θ dependence of specific heat $C(H)/T$ of URhGe at 1.5 K, measured at $\theta = 0°, 1.01°, 2.43°$, 3.86° and 5.29°, where θ is an angle from the b towards the c axes. Numbers in the parenthesis mean offsets of C/T value.

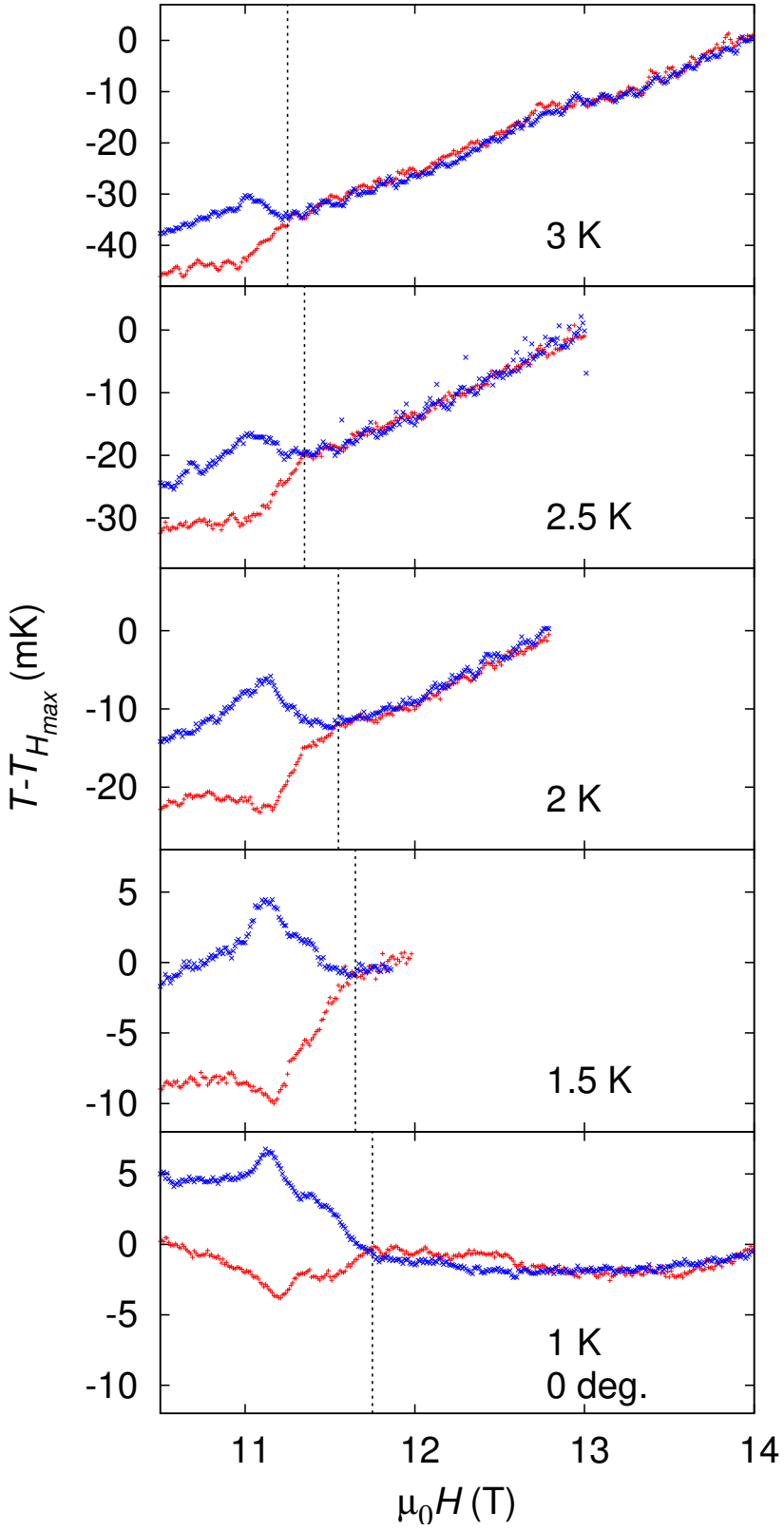

Figure 6.6: Temperature variation of MCE at $\theta = 0°$, obtained at 1, 1.5, 2, 2.5, and 3 K. Even at 2-3 K, MCE shows a first order behavior, i.e. a peak (a dip). In this figure, field-up (red) and field-down (blue) are plotted.

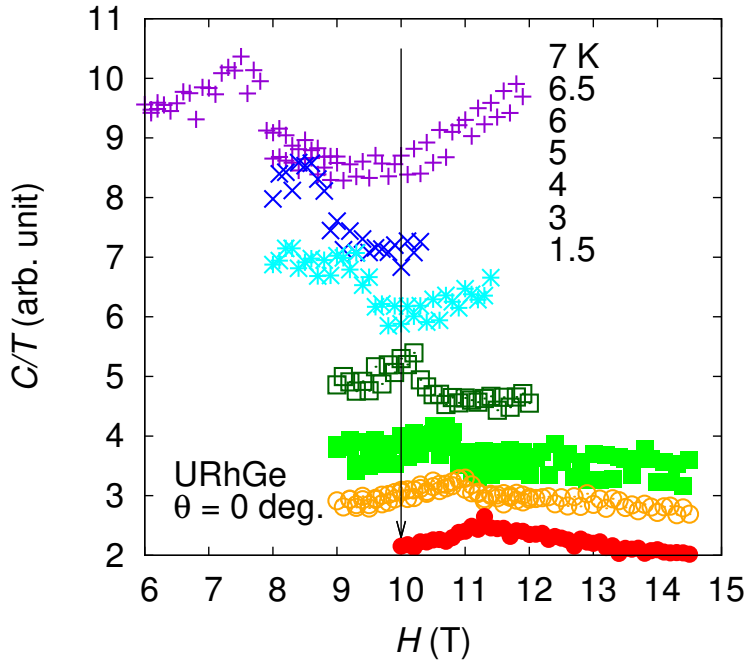

Figure 6.7: Temperature variation of $C(H)/T$ at $\theta = 0°$, measured at 1.5, 3, 4, 5, 6, 6.5, and 7 K.

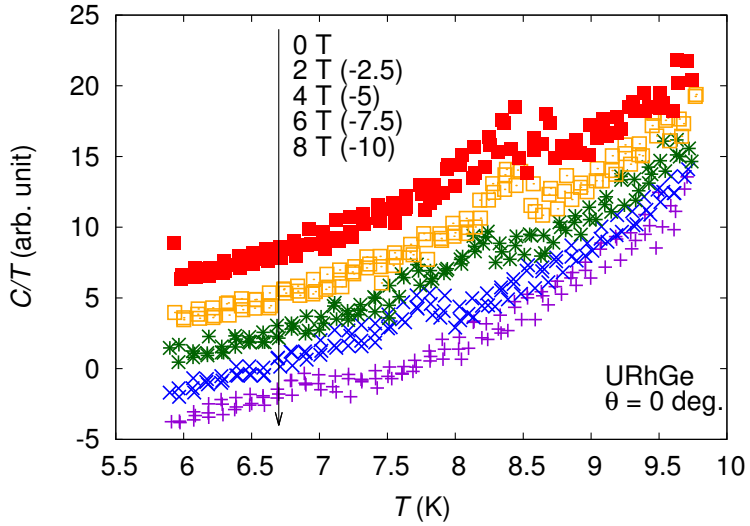

Figure 6.8: Magnetic field variation of $C(T)/T$ at $\theta = 0°$, measured in the field of 0, 2, 4, 6, and 8 T. Numbers in the parenthesis mean offsets of C/T value.

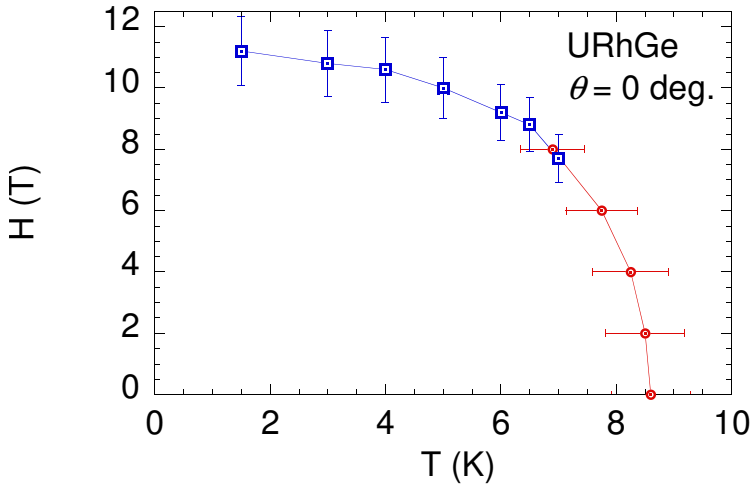

Figure 6.9: H-T phase diagram obtained by specific heat measurements of $C(H)/T$ sweep (blue square) and $C(T)/T$ sweep (red circle).

6.4 Summary

We have performed high-precision field-angle resolved specific heat and magneto-caloric effect (MCE) measurements in magnetic field applied near the b axis, and investigated the quantum phase transition of an Ising ferromagnet URhGe. A feature of a first-order spin reorientation transition is observed by means of MCE measurements even at high temperature up to 2-3 K in the magnetic field along the b axis, even though the hysteresis disappears above 1 K in magnetization measurements (Chapter 5). This fact demonstrates that the first order transition persists ever in the region where the hysteresis of the transition vanishes. This result supports the conclusion that the tricritical point locates above 4 K. On the other hand, no clear qualitative change of the transition is detected in specific heat measurements. With increasing θ (an angle from the b towards the c axes), the transition becomes broader and shifts to higher magnetic fields, and it is good agreement with the magnetization measurements in Chapter 5.

Chapter 7

Conclusion

In order to investigate the wing structure in an Ising ferromagnet URhGe, we have successfully developed high-precision two-axis rotation device, which can move even at low temperatures below 4.2 K. We also make new magnetometer and specific-heat cell for measurements of a high-torque sample. The performance evaluation of the new device has been done in $CeRu_2Si_2$, and after that, we measured the magnetization, magnetization torque, specific heat, and magneto-caloric effect in the temperature and field-angular range of quantum phase transition; i.e. the wing structure, the tricritical point (TCP), and the quantum wing critical points (QWCPs). In this chapter, obtained results are summarized with focusing on the development of the two-axis rotation device and the investigation of the wing structure of URhGe.

In order to measure the magnetization and the magnetization torque under two-angle precisely-controlled magnetic field orientation, we have developed a capacitively-detected Faraday magnetometer installed with two-angle rotation device. The orientation of the sample is precisely controlled within an accuracy of less than 0.01° using a piezo-stepper-driven goniometer (ϕ rotation) combined with a home-made tilting stage (θ rotation). The available angle ranges are $-3^\circ \leq \phi \leq 3^\circ$ and $-10^\circ \leq \theta \leq 10^\circ$, where the ϕ and θ axes are perpendicular to each other. In order to test the performance of two axis rotation device, the angular θ and ϕ dependences of the magnetization curves of $CeRu_2Si_2$ have been measured. θ and ϕ are driven by a home-made tilting stage and a piezo stepper goniometer, respectively. In this measurements, metamagnetic jump is observed at low temperatures, and the angular θ and ϕ dependences of the critical fields are scaled by $1/\cos\theta$ and $1/\cos\phi$, respectively, suggesting that the rotation device works at low temperature below 4 K. We also checked the θ and ϕ position repeatability. The properties of magnetization curve of $CeRu_2Si_2$ do not change from previous magnetization study even

in "in-situ" magnetic field along the [001] axis, suggesting that the nature of the metamagnetic jump is a crossover.

As shown in the above, the two axis rotation device is available for low temperatures high-precision angle-resolved measurements. We have investigated the quantum phase transition of the Ising ferromagnet URhGe by means of high-precision angle-resolved dc magnetization, magnetic torque, specific heat, and magneto-caloric effect (MCE) measurements in magnetic fields applied near the b axis, using this device. A small hysteresis in the critical field, i.e. first order behavior, is observed below 1 K in the magnetization measurements. A feature of of a first-order spin reorientation transition is observed by means of MCE measurements even at high temperature up to 2-3 K in the magnetic field along the b axis, even though the hysteresis disappears above 1 K in magnetization measurements. This fact demonstrates that the first order transition persists ever in the region where the hysteresis of the transition vanishes. The temperature and angular variations of the magnetization and the magnetic torque curves allow us to construct the three-dimensional $T - H_c - H_b$ phase diagram, where H_c ($\parallel c$) is the conjugate field parallel to the order parameter and H_b is the b axis component of the field that tunes $T_{\rm C}$ down to zero. The results of specific heat and MCE also support the three-dimensional phase diagram given by magnetization and magnetic torque measurements. The tricritical point $T_{\rm TCP}$ is estimated to be located above 4 K in the $H_c = 0$ plane by the contour plot obtained by magnetization measurements. No clear qualitative change of the transition is, however, detected above 4 K, indicating difficulty of deciding the position of TCP. On cooling below $T_{\rm TCP}$, a wing structure develops by increasing $|H_c|$. We have succeeded in directly determining the detailed profiles of the wing structure. The quantum wing critical points exist at $H_c = \pm 1.1$ T and $H_b = 13.5$ T. Three second-order transition lines meet at $T_{\rm TCP}$ tangentially, so that a precise tuning of H along the b axis within 0.8° is needed to correctly determine the position of TCP. The reentrant superconductivity (RSC) in this system is not due to a quantum TCP [72], but is rather related to unusually weak nature of the first-order transition represented by a smallness of the hysteresis and a broadness of the transition. Even though it is no doubt that there is the magnetic fluctuations at low temperatures and it may play an essential role of RSC, the origin of the fluctuation is still unclear.

In this thesis, we have developed the two-axis rotation device for the magnetization, the magnetic torque, the specific heat, and the MCE measurements. The device allows us to perform in-situ angle resolved measurements in these physical quantities, and it is expected to greatly contribute to elucidation of physics in heavy electron systems, which usually have strong anisotropy.

Appendix A

A.1 Temperature variation of the magnetization curves of URhGe at several θ

For simply, we show the temperature variation of the magnetization curves only at $\theta = 0°$ in Fig. 5.15 in Chapter 5. The rest of the temperature variation measured at $\theta = 0.79°, 1.65°, 3.64°$ and $5.64°$ is shown in this section, together with the derivative dM/dH. Here, θ is an angle from the b axis towards the c axis.

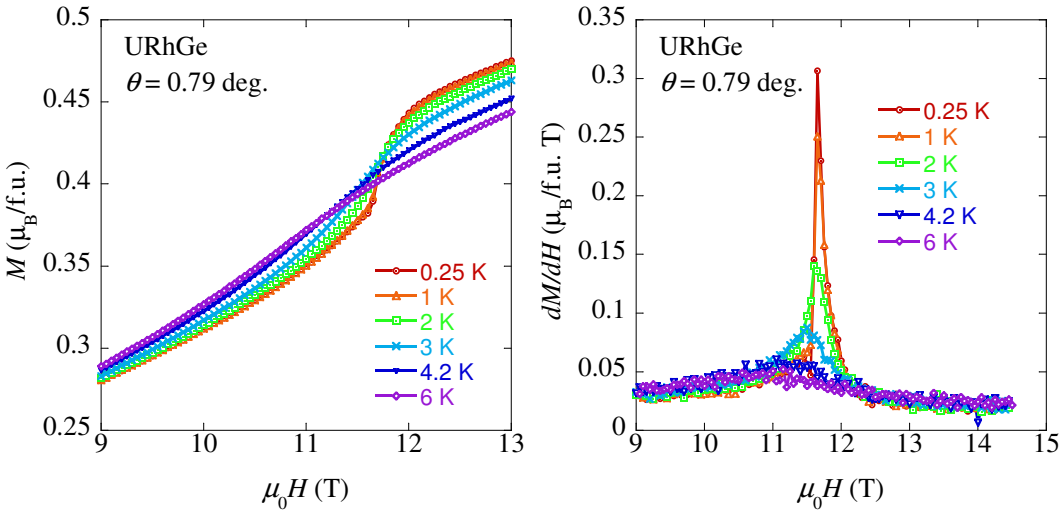

Figure A.1: Temperature variation of the magnetization curves at $\theta = 0.79°$.

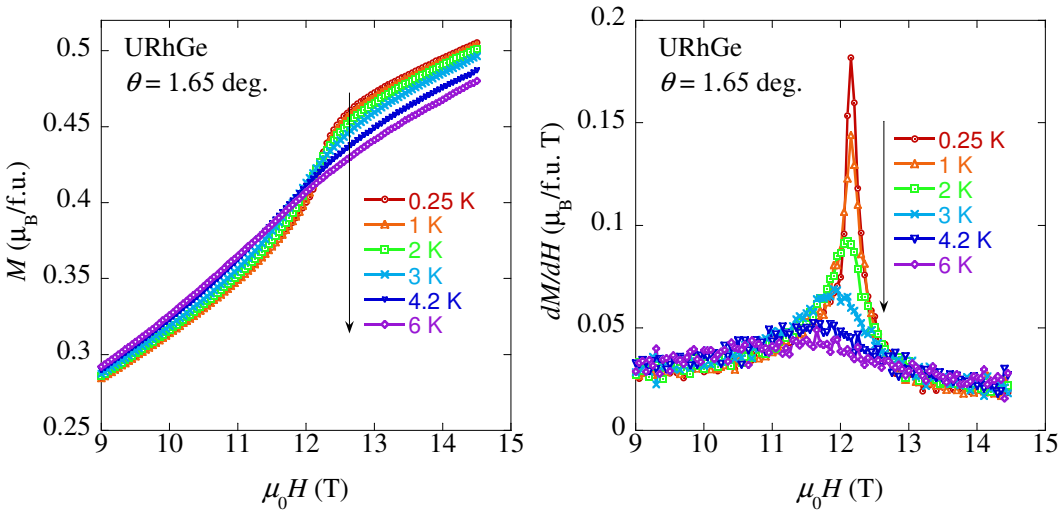

Figure A.2: Temperature variation of the magnetization curves at $\theta = 1.65°$.

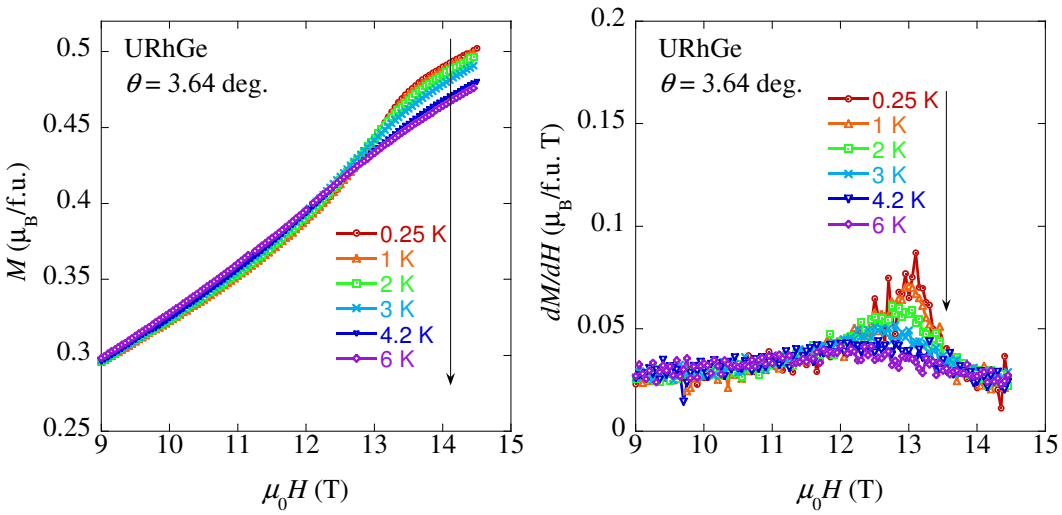

Figure A.3: Temperature variation of the magnetization curves at $\theta = 3.64°$.

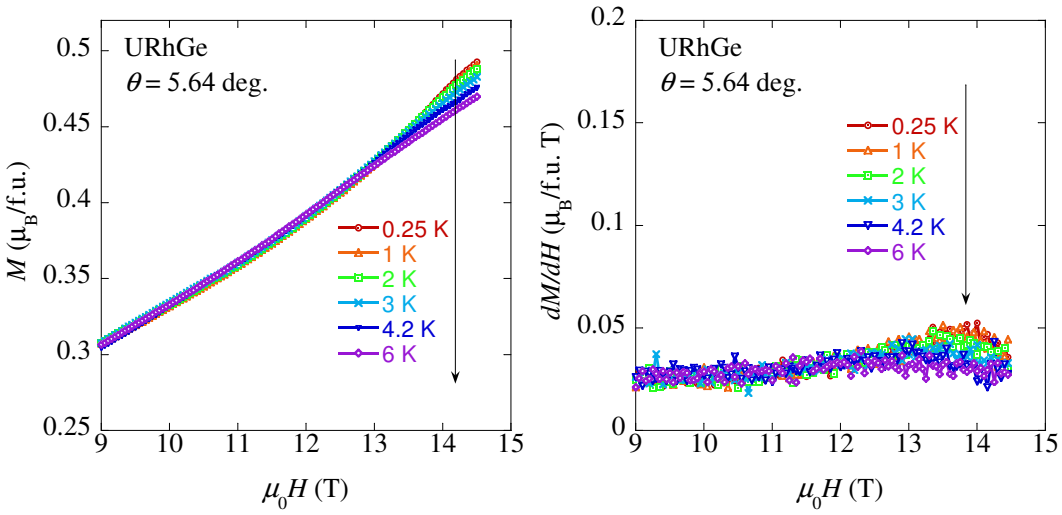

Figure A.4: Temperature variation of the magnetization curves at $\theta = 5.64°$.

A.2 Angular θ variation of the magnetization curves of URhGe at several temperature

For simply, we show the θ variation of the magnetization curves at 0.25, 3 and 6 K in Fig. 5.18 in Chapter 5. The rest of the θ variation measured at 0.5, 1, 1.5, 2, 2.5, 3.5, 4.2 and 5 K is shown in this section, together with the derivative dM/dH. Here, θ is an angle from the b axis towards the c axis. Note that the magnetization curve obtained at $\theta = 0^\circ$ contains some torque contribution, which appears below the critical field H_R.

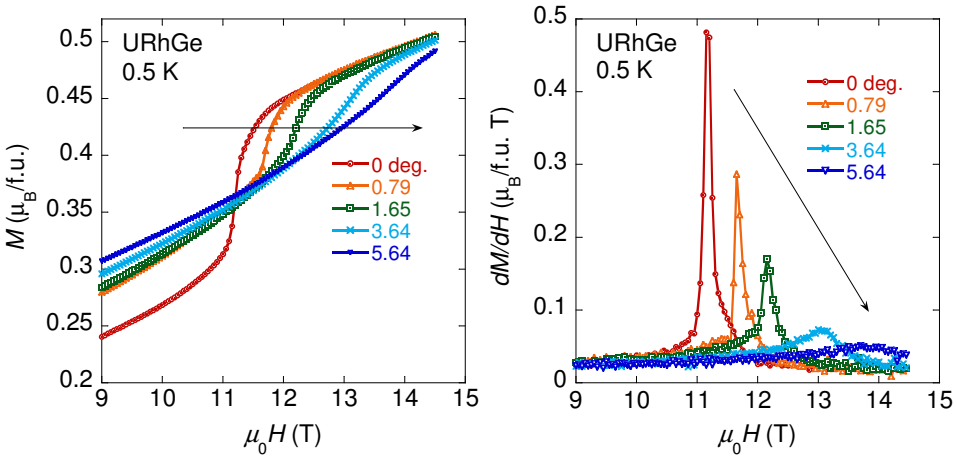

Figure A.5: θ variation of the magnetization curves at 0.5 K.

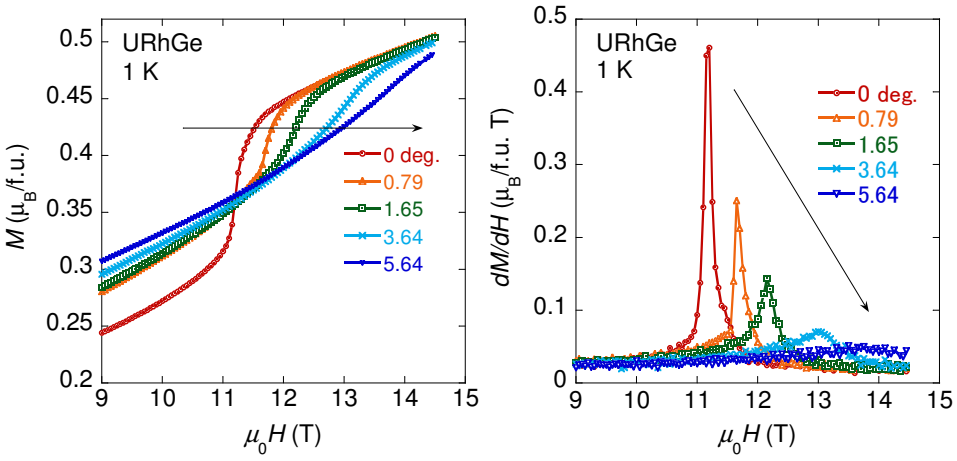

Figure A.6: θ variation of the magnetization curves at 1 K.

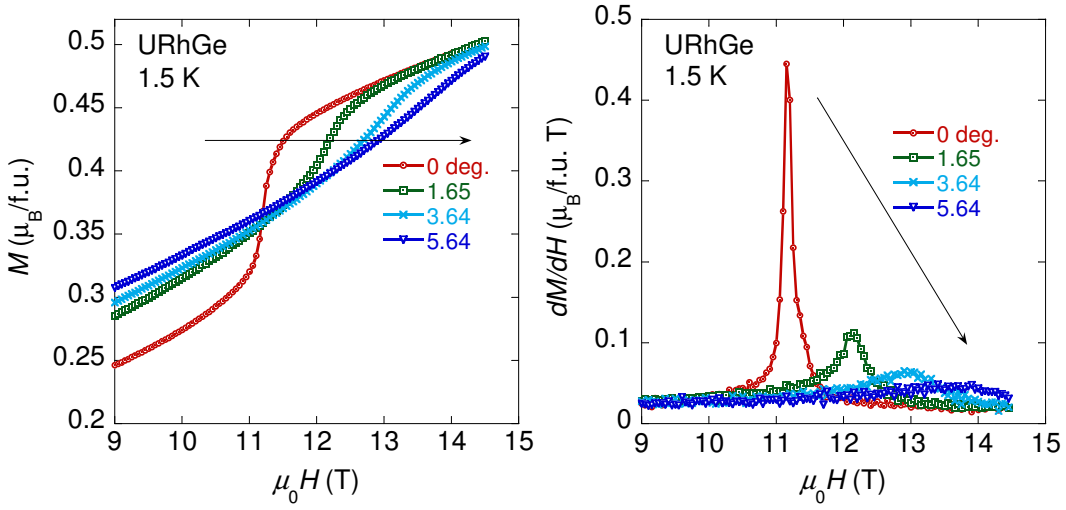

Figure A.7: θ variation of the magnetization curves at 1.5 K.

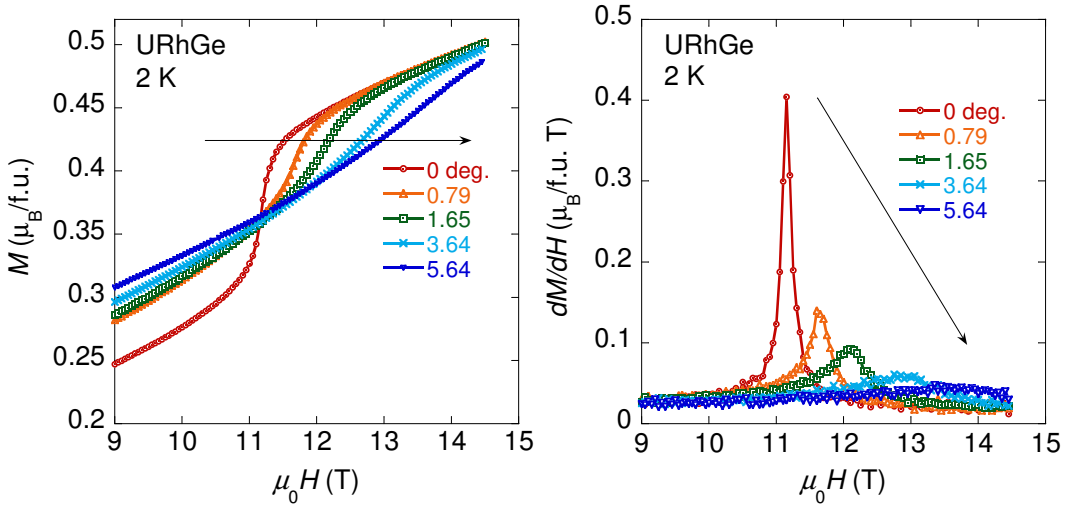

Figure A.8: θ variation of the magnetization curves at 2 K.

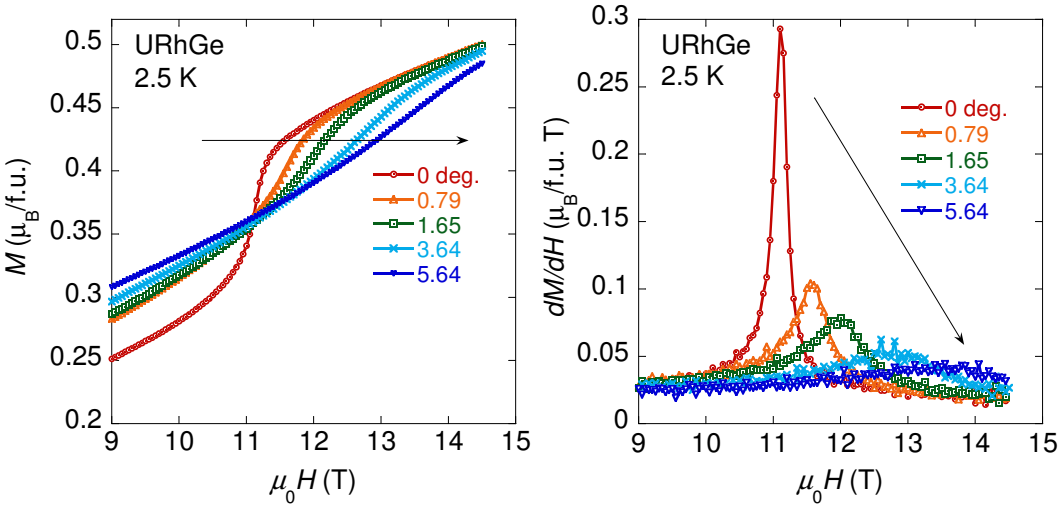

Figure A.9: θ variation of the magnetization curves at 2.5 K.

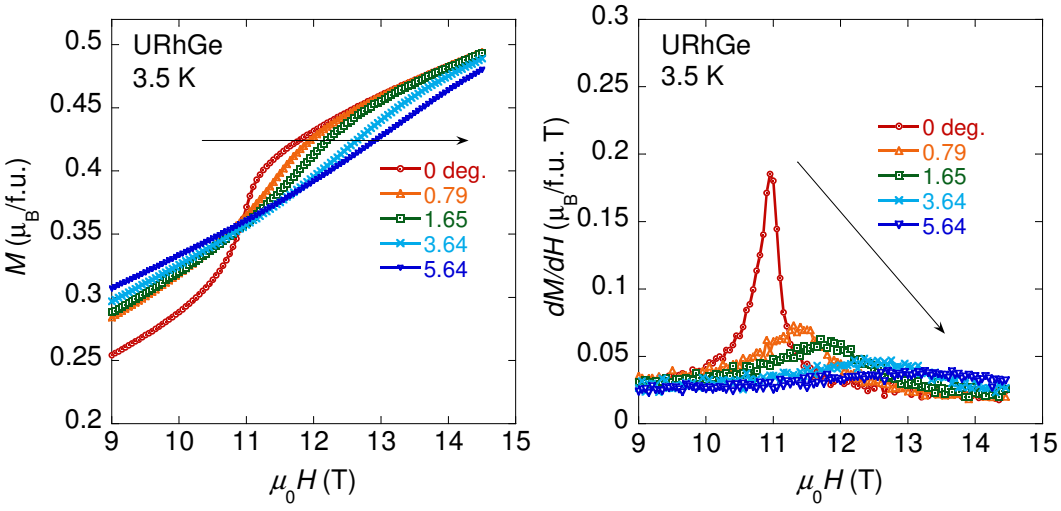

Figure A.10: θ variation of the magnetization curves at 3.5 K.

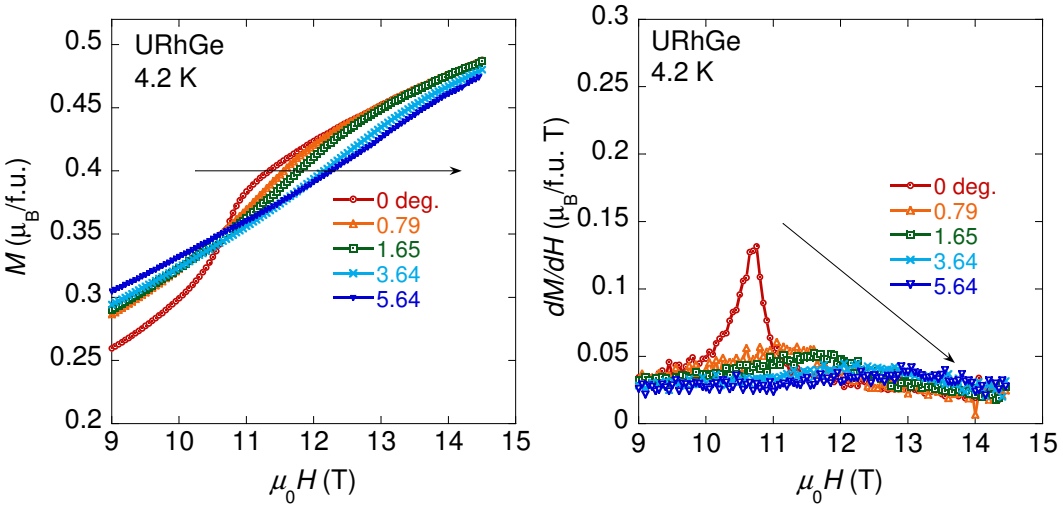

Figure A.11: θ variation of the magnetization curves at 4.2 K.

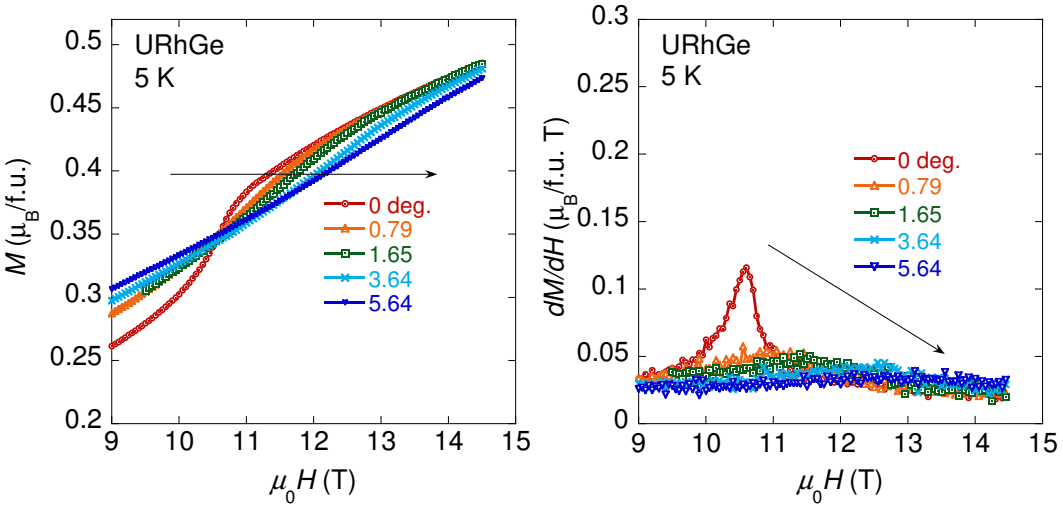

Figure A.12: θ variation of the magnetization curves at 5 K.

A.3 Angular θ variation of the magneto-caloric effect of URhGe at several temperature

For simply, we show the θ variation of the magneto-caloric effect measured at 1.5 K in Fig. 6.4 in Chapter 6. The rest of the θ variations measured at 1, 2, 2.5, 3, 3.5 and 4 K are shown in this section. Angles in these figures denotes θ, which is an angle from the b axis towards the c axis. In these figure, not only field-up (red) and field-down (blue) sweeps are plotted.

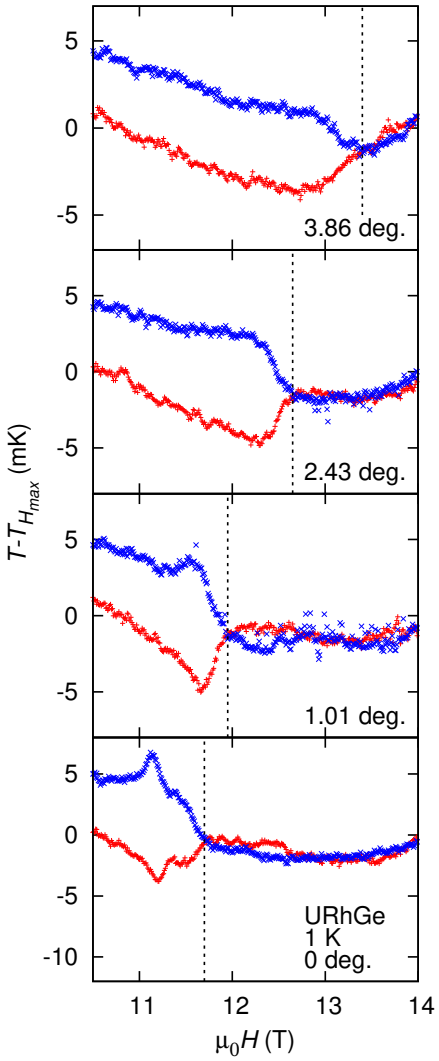

Figure A.13: θ variation of the magneto-caloric effect at 1 K.

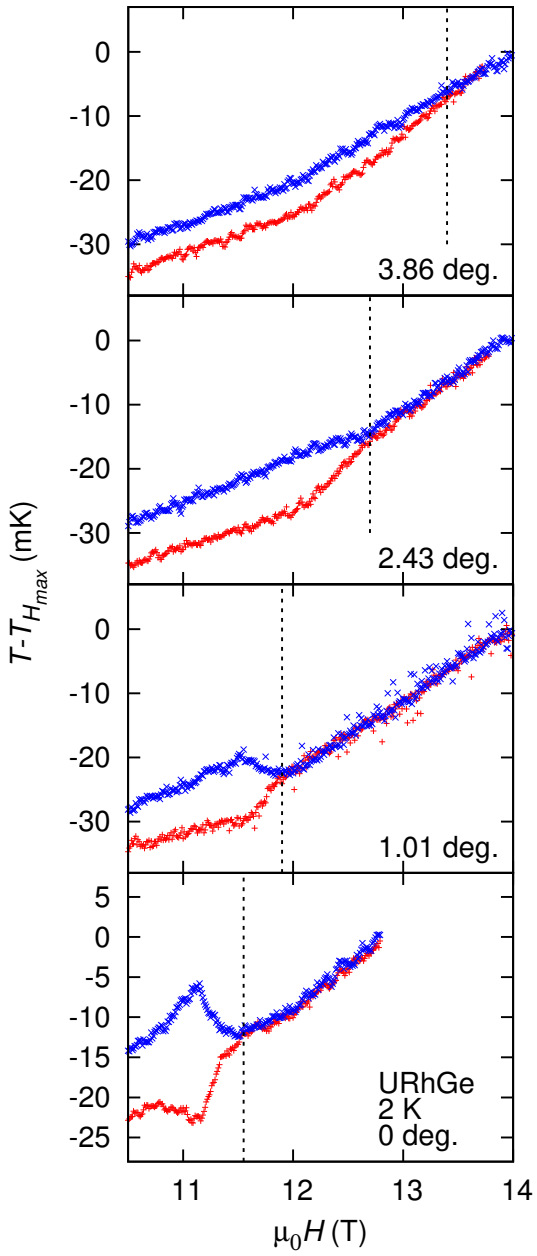

Figure A.14: θ variation of the magneto-caloric effect at 2 K.

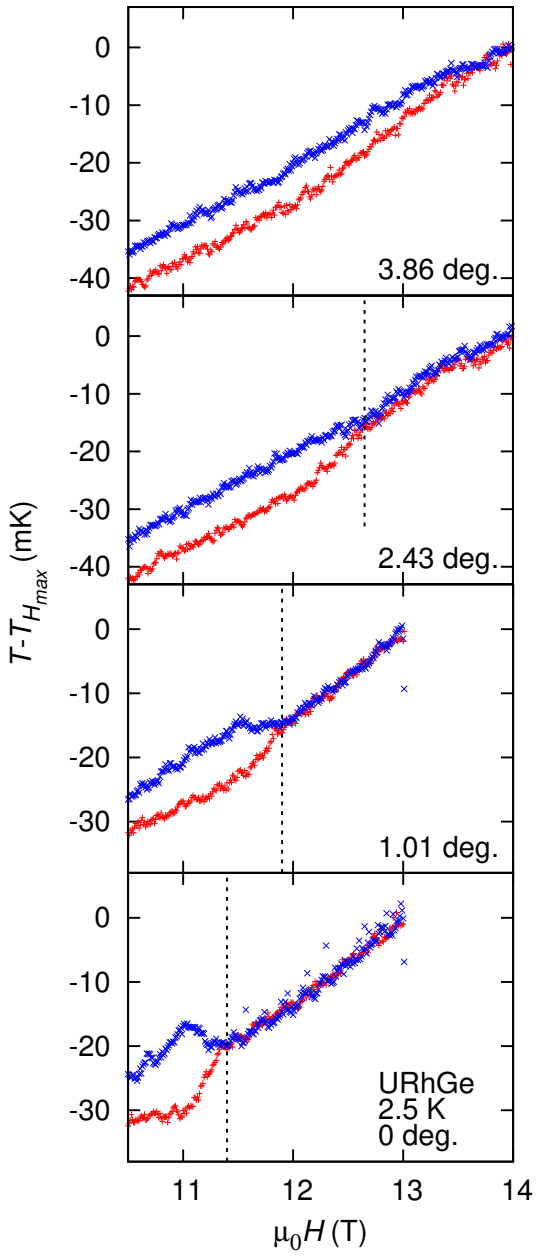

Figure A.15: θ variation of the magneto-caloric effect at 2.5 K.

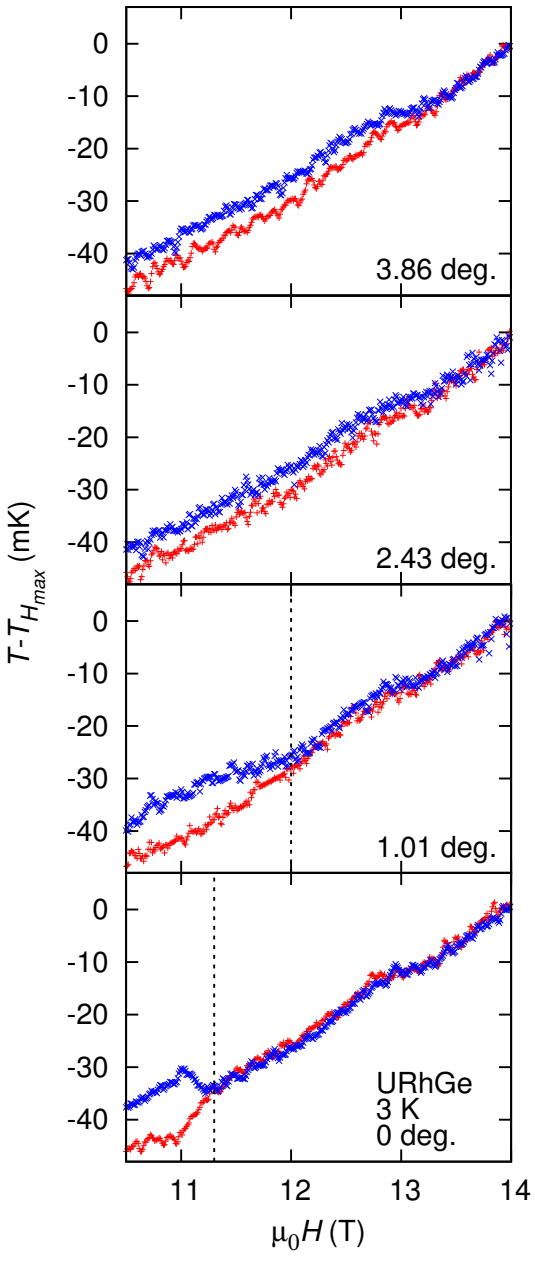

Figure A.16: θ variation of the magneto-caloric effect at 3 K.

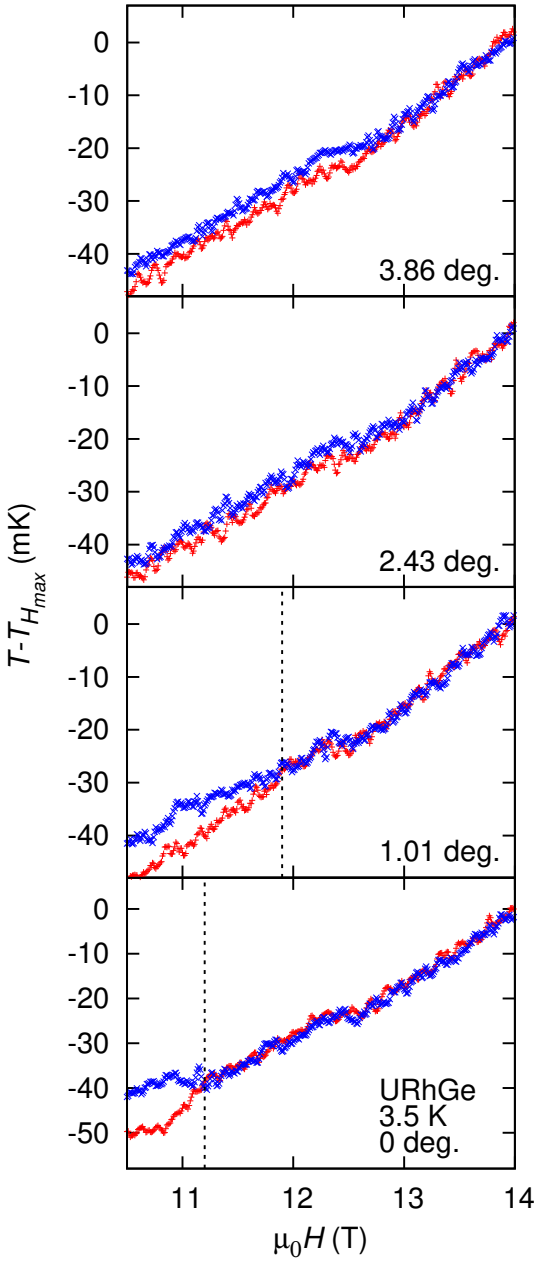

Figure A.17: θ variation of the magneto-caloric effect at 3.5 K.

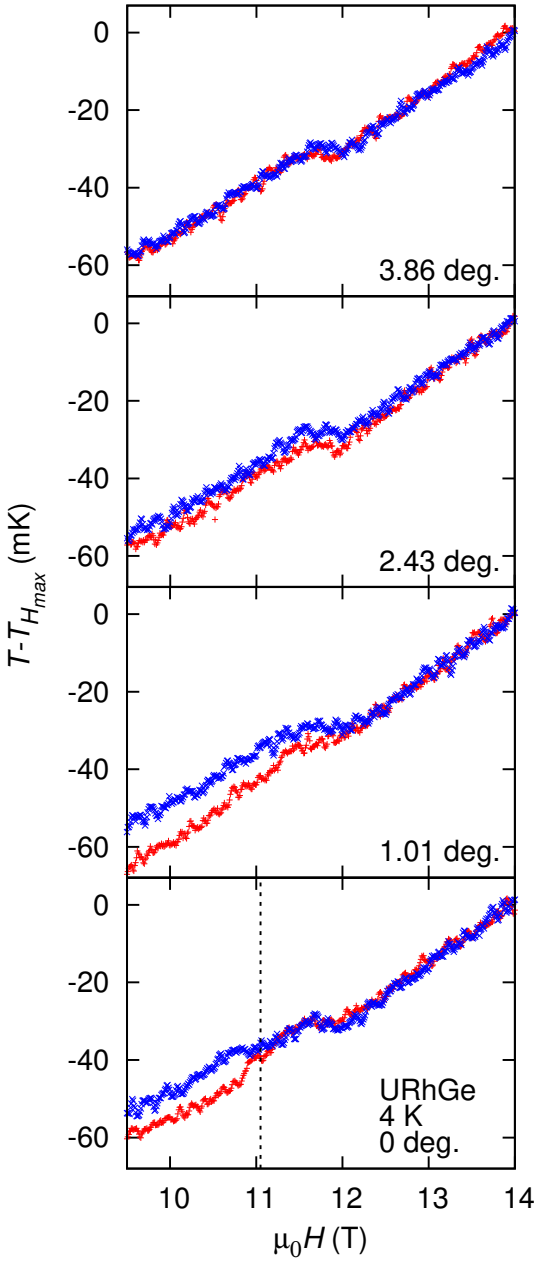

Figure A.18: θ variation of the magneto-caloric effect at 4 K.

Appendix B

B.1 Gnuplot source code for simulating the sample temperature change in magneto-caloric effect measurements

The sample temperature change caused by MCE of URhGe is simulated in Chapter 6. In this chapter, the simulation has been performed by using Gnuplot, and the source code is shown as follows.

```
1  set key noautotitles
2  #x=H
3  set samples 5000
4
5  ######Entropy######
6
7  Hc=11.3#Critical field
8  Hca=10.9#the beginning field of the transition
9  A=0.01#coefficient
10 B=0.1#coefficient
11 S0=0.#origin of entropy
12 C=5e-7#[J]
13 set output
14 set terminal win
15 set xlabel '{/Arial-Italic H} (T)'
16 set ylabel '{/Arial-Italic S}'
17 S1(x)=(x < Hca ? (A*(x-Hca)+B*(Hca-Hc)+S0) : (x < Hc ? (B*(x
       -Hc)+S0) : S0))
18 S2(x)=(x < Hc ? (A*(x-Hc)+S0) : S0)
```

```
19 set xrange [10.4:11.8]
20 set yrange [-0.06:0.01]
21 plot S1(x) ps 2 lc rgb "dark-green"
22
23 set terminal postscript eps color enhanced "Arial" 25
24 set output "Entropy1.eps"
25 pause -1
26 replot
27
28 set output
29 set terminal win
30
31 set xlabel '{/Arial-Italic H} (T)'
32 set ylabel '{/Arial-Italic S}'
33 set xrange [10.4:11.8]
34 set yrange [-0.06:0.01]
35 plot S2(x) ps 2 lc rgb "dark-green"
36
37 set terminal postscript eps color enhanced "Arial" 25
38 set output "Entropy2.eps"
39 pause -1
40 replot
41
42 set output
43 set terminal win
44
45
46 ######Estimation of sample temperature change######
47
48 T0=1.5#T_Bath
49 Hc=11.3#Critical field
50 Hc1=10.9#the beginning field of the transition
51 r=20.#relaxation time
52 C=5e-7#J/K
53 s=0.003#field-sweep rate[T/sec.]@field-up sweep
54 sd=-0.003#field-sweep rate[T/sec.]@field-down sweep
55
56
57 ######2nd_order_transition_feild-up######
```

```
58
59 #coefficient_2nd_order_transition_feild-up
60 A21=7e-8#A21 is equal to value of k below Hc, where S(H)=kH+
       1.
61 A22=-7e-12#A21 is equal to value of k above Hc, where S(H)=
       kH+1.
62 D21=T0*(1-1/(1+A21*r*s/C))#temperature=T0 @ 0 T
63 T21=(D21*exp(-(A21/C+1/s/r)*Hc)+T0/(A21*s*r/C+1))
64 D22=(T21-T0)/exp(-Hc/s/r)#continuation at Hc
65 #Sample temp. @ 2nd_order_field-up
66 Ts21(x)=D21*exp(-(A21/C+1/s/r)*x)+T0/(A21*s*r/C+1)
67 Ts22(x)=D22*exp(-(A22/C+1/s/r)*x)+T0/(A22*s*r/C+1)
68
69
70
71 ######2nd_order_transition_field-down######
72
73 #coefficient_2nd_order_transition_feild-down
74 D22d=exp((A22/C+1/sd/r)*15)*T0*(1-1/(A22*sd*r/C+1))#
       temperature=T0 @15 T
75 D21d=(D22d*exp(-(A22/C+1/sd/r)*Hc)+T0/(A22*sd*r/C+1)-T0/(A21
       *sd*r/C+1))/exp(-(A21/C+1/sd/r)*Hc)#continious at Hc
76 #Sample temp. @ 2nd_order_field-down
77 Ts21d(x)=D21d*exp(-(A21/C+1/sd/r)*x)+T0/(A21*sd*r/C+1)
78 Ts22d(x)=D22d*exp(-(A22/C+1/sd/r)*x)+T0/(A22*sd*r/C+1)
79
80 ######1st_order_transition_field-up######
81
82 #k value at several field ranges, where S(H)=kH+1.
83 A11=7e-8#H<Hc1
84 A12=7e-7#Hc1<H<Hc
85 A13=-7e-12#Hc<H
86 #coefficient_1st_order_transition_feild-up
87 D11=T0*(1-1/(1+A11*r*s/C))#temperature=T0 @ 0 T
88 T11=D11*exp(-(A11/C+1/s/r)*Hc1)+T0/(A11*s*r/C+1)#Sample temp
       . below Hc1
89 D12=(T11-T0/(A12*r*s/C+1))/exp(-(A12/C+1/s/r)*Hc1)#
       continuation at Hc1
90 T12=(D12*exp(-(A12/C+1/s/r)*Hc)+T0/(A12*s*r/C+1))
```

```
91  D13=(T12-T0)/exp(-Hc/s/r)#continuation at Hc
92  #Sample temp. @ 1st_order_field-up
93  Ts11(x)=D11*exp(-(A11/C+1/s/r)*x)+T0/(A11*s*r/C+1)
94  Ts12(x)=D12*exp(-(A12/C+1/s/r)*x)+T0/(A12*s*r/C+1)
95  Ts13(x)=D13*exp(-(A13/C+1/s/r)*x)+T0/(A13*s*r/C+1)
96
97  ######1st_order_transition_field-down######
98
99  #1st_order_transition_field-down
100 D13d=T0*(1-1/(A13*sd*r/C+1))/exp(-(A13/C+1/sd/r)*15)#
        temperature=T0 @ 15 T
101 D12d=(D13d*exp(-(A13/C+1/sd/r)*Hc)+T0/(A13*sd*r/C+1)-T0/(A12
        *sd*r/C+1))/exp(-(A12/C+1/sd/r)*Hc)#continuation at Hc
102 D11d=(D12d*exp(-(A12/C+1/sd/r)*Hc1)+T0/(A12*sd*r/C+1)-T0/(
        A11*sd*r/C+1))/exp(-(A11/C+1/sd/r)*Hc1)#continuation at
        Hc1
103 #Sample temp. @ 1st_order_field-down
104 Ts11d(x)=D11d*exp(-(A11/C+1/sd/r)*x)+T0/(A11*sd*r/C+1)
105 Ts12d(x)=D12d*exp(-(A12/C+1/sd/r)*x)+T0/(A12*sd*r/C+1)
106 Ts13d(x)=D13d*exp(-(A13/C+1/sd/r)*x)+T0/(A13*sd*r/C+1)
107
108 set xrange [10.4:11.8]
109 set yrange [1.35:1.65]
110
111 ######Functions of sample temp.######
112 Ts1(x) = (x < Hc1 ? Ts11(x) : (x < Hc ? Ts12(x) : Ts13(x)))#
        Sample temp. @ 1st_order_field-up
113 Ts1d(x) = (x < Hc1 ? Ts11d(x) : (x < Hc ? Ts12d(x) : Ts13d(x
        )))#Sample temp. @ 1st_order_field-down
114 Ts2(x) = (x < Hc ? Ts21(x) : Ts22(x))#Sample temp. @ 2
        nd_order_field-up
115 Ts2d(x) = (x < Hc ? Ts21d(x) : Ts22d(x))#Sample temp. @ 2
        nd_order_field-down
116 set xlabel '{/Arial-Italic H} (T)'
117 set ylabel '{/Arial-Italic T_S} (K)'
118
119 plot Ts1(x) ps 2 lc rgb "red", Ts1d(x) ps 2 lc rgb "blue"
120
121 set terminal postscript eps color enhanced "Arial" 25
```

```
122 set output "first_MCE_URhGe.eps"
123 pause -1
124 replot
125
126 set output
127 set terminal win
128
129
130 plot Ts2(x) ps 2 lc rgb "red", Ts2d(x) ps 2 lc rgb "blue"
131
132 set terminal postscript eps color enhanced "Arial" 25
133 set output "second_MCE_URhGe.eps"
134 pause -1
135 replot
136
137 #end.
```

Publications

First Author

1. Shota NAKAMURA, Toshiro SAKAKIBARA, Yusei SHIMIZU, Yohei KONO, Shunichiro KITTAKA, Yoshinori HAGA, Jiří POSPÍŠIL, and Etsuji YAMAMOTO, "*Wing structure in the phase diagram of the Ising ferromagnet URhGe close to its tricritical point investigated by angle-resolved magnetization measurements*", Phys. Rev. B. **96**, 094411 (2017). **PRB Editors′ Suggestion**

2. SHOTA NAKAMURA, YUHJI TSUJIMI, "*Broad Doublet Spectra in the Quantum Paraelectric State of* $SrTiO_3$", Ferroelectrics, Taylor & amp; Francis Group, LLC, **485**, 20-26 (2015).

Coauthor

1. Yue Sun, Shunichiro Kittaka, Shota Nakamura, Toshiro Sakakibara, Koki Irie, Takuya Nomoto, Kazushige Machida, Jingting Chen, and Tsuyoshi Tamegai, "*Gap structure of FeSe determined by angle-resolved specific heat measurements in applied rotating magnetic field*", Phys. Rev. B **96**, 220505(R) (2017).

2. Y. Shimizu, S. Kittaka, S. Nakamura, T. Sakakibara, D. Aoki, Y. Homma, A. Nakamura, and K. Machida, "*Quasiparticle Excitations and Evidence for Superconducting Double Transitions in Monocrystalline* $U_{0.97}Th_{0.03}Be_{13}$", Phys. Rev. B **96**, 100505(R) (2017). **PRB Editors′ Suggestion**

3. K. Mochidzuki, Y. Shimizu, A. Kondo, S. Nakamura, S. Kittaka, Y. Kono, T. Sakakibara, Y. Ikeda, Y. Isikawa, and K. Kindo, "*Thermodynamic Investigation of Metamagnetic Transitions and Partial Disorder in the Quasi-Kagome Kondo Lattice CePdAl*", J. Phys. Soc. Jpn. **86**, 034709 (2017).

4. M. Kakihana, K. Nishimura, Y. Ashitomi, T. Yara, D. Aoki, A. Nakamura, F. Honda, M. Nakashima, Y. Amako, Y. Uwatoko, T. Sakakibara, S. Nakamura, T. Takeuchi, Y. Haga, E. Yamamoto, H. Harima, M. Hedo, T. Nakama, Y. Ōnuki, "*Unique Electronic States in Non-centrosymmetric Cubic Compounds*", J. Electron. Mater. **46**, 3572 (2017).

5. R. Otaka, M. Yokoyama, H. Mashiko, T. Hasegawa, Y. Shimizu, Y. Ikeda, K. Tenya, S. Nakamura, D. Ueta, H. Yoshizawa, and T. Sakakibara, "*Superconductivity and Non-Fermi- Liquid Behavior in the Heavy-Fermion Compound* $CeCo_{1-x}Ni_xIn_5$", J. Phys. Soc. Jpn. **85**, 094713 (2016).

6. Makoto Yokoyama, Hiroaki Mashiko, Ryo Otaka, Yoshiki Oshima, Kohei Suzuki, Kenichi Tenya, Yusei Shimizu, Ai Nakamura, Dai Aoki, Akihiro Kondo, Koichi Kindo, Shota Nakamura, and Toshiro Sakakibara, "*Observation of a new field-induced phase transition and its concomitant quantum critical fluctuations in* $CeCo(In_{1-x}Zn_x)_5$", Phys. Rev. B **95**, 224425 (2017).

7. Mate Hartstein, William Toews, Yu -Te Hsu, Bin Zeng, Xiaoye Chen, Monica Ciomaga Hatnean, Qiu Run Zhang, Shota Nakamura, Andrew Padgett, Gilles Rodway-Gant, Joel Berk, Matthew Kingston, Grace Zhang, Mun Chan, Satoshi Yamashita, Toshiro Sakakibara, Yasumasa Takano, Ju-Hyun Park, Luis Balicas, Neil Harrison, Natalya Shitsevalova, Geetha Balakrishnan, Gilbert Lonzarich, Robert Hill, Michael L Sutherland, and Suchitra Sebastian, "*Fermi surface in the absence of a Fermi liquid in the Kondo insulator* SmB_6", Nat. Phys., doi:10.1038/nphys4295, (2017).

8. Shunsuke Suzuki, Toru Mogami, Shota Nakamura, Yuhji Tsujimi & Makoto Iwata, "*Soft-mode behavior in lanthanide-modified bismuth titanates*", Ferroelectrics, Taylor & Francis Group, LLC, **512**, 52-57 (2017).

9. Hiroki Ninomiya, Yuji Matsumoto, Shota Nakamura, Yohei Kono, Shunichiro Kittaka, Toshiro Sakakibara, Katsuya Inoue, and Shigeo Ohara, "*Magnetic Properties and Magnetic Phase Diagrams of Trigonal* $DyNi_3Ga_9$", J. Phys. Soc. Jpn., **86**, 124704 (2017).

10. Masashi Kakihana, Dai Aoki, Ai Nakamura, Fuminori Honda, Miho Nakashima, Yasushi Amako, Shota Nakamura, Toshiro Sakakibara, Masato Hedo, Takao Nakama, and Yoshichika Ōnuki, "*Giant Hall Resistivity and Magnetoresistance in Cubic Chiral Antiferromagnet EuPtSi*", J. Phys. Soc. Jpn., **87**, 023701 (2018).

Bibliography

[1] M. E. Fisher, Journal of Mathematical Physics **4**, 124 (1963).

[2] S. Katsura, Physical Review **127**, 1508 (1962).

[3] P. Pfeuty, Ann. Phys. **57**, 79 (1970).

[4] O. Nagai, Y. Yamada, K. Nishino, and Y. Miyatake, Phys. Rev. B **35**, 3425 (1987).

[5] L. D. Landau and E. M. Lifshitz, Statistical Physics, Vol. 5 (Pergamon Press, 1959).

[6] C. Kittel and H. Kroemer, Thermal Physics (W. H. Freeman, 1980).

[7] M. Brando, D. Belitz, F. M. Grosche, and T. R. Kirkpatrick, Rev. Mod. Phys. **88**, 025006 (2016).

[8] V. Taufour, U. S. Kaluarachchi, and V. G. Kogan, Phys. Rev. B **94**, 060410 (2016).

[9] D. Belitz, T. R. Kirkpatrick, and T. Vojta, Phys. Rev. Lett. **82**, 4707 (1999).

[10] D. Belitz, T. R. Kirkpatrick, and J. Rollbühler, Phys. Rev. Lett. **94**, 247205 (2005).

[11] T. R. Kirkpatrick and D. Belitz, Phys. Rev. Lett. **115**, 020402 (2015).

[12] H. Yamada, Physica B: Condensed Matter **391**, 42 (2007).

[13] Y. Sang, D. Belitz, and T. R. Kirkpatrick, Phys. Rev. Lett. **113**, 207201 (2014).

[14] V. Taufour, D. Aoki, G. Knebel, and J. Flouquet, Phys. Rev. Lett. **105**, 217201 (2010).

[15] C. Pfleiderer and A. D. Huxley, Phys. Rev. Lett. **89**, 147005 (2002).

[16] H. Kotegawa, V. Taufour, D. Aoki, G. Knebel, and J. Flouquet, J. Phys. Soc. Jpn. **80**, 083703 (2011).

[17] M. Uhlarz, C. Pfleiderer, and S. M. Hayden, Phys. Rev. Lett. **93**, 256404 (2004).

[18] N. Kimura, M. Endo, T. Isshiki, S. Minagawa, A. Ochiai, H. Aoki, T. Terashima, S. Uji, T. Matsumoto, and G. G. Lonzarich, Phys. Rev. Lett. **92**, 197002 (2004).

[19] Y. Shimizu, D. Braithwaite, B. Salce, T. Combier, D. Aoki, E. N. Hering, S. M. Ramos, and J. Flouquet, Phys. Rev. B **91**, 125115 (2015).

[20] M. Míšek, J. Prokleška, P. Opletal, P. Proschek, J. Kaštil, J. Kamarád, and V. Sechovskỳ, AIP Advances **7**, 055712 (2017).

[21] W. Wu, A. McCollam, S. A. Grigera, R. S. Perry, A. P. Mackenzie, and S. R. Julian, Phys. Rev. B **83**, 045106 (2011).

[22] T. Goto, K. Fukamichi, and H. Yamada, Physica B: Condensed Matter **300**, 167 (2001).

[23] C. Pfleiderer, S. Julian, and G. Lonzarich, Nature **414**, 427 (2001).

[24] D. Aoki, T. Combier, V. Taufour, T. D. Matsuda, G. Knebel, H. Kotegawa, and J. Flouquet, J. Phys. Soc. Jpn. **80**, 094711 (2011).

[25] Y. Kitaoka, N.-S. Chang, T. Ebisu, M. Matsumura, K. Asayama, and K. ichi Kumagai, J. Phys. Soc. Jpn. **54**, 1543 (1985).

[26] C. Bernhard, J. L. Tallon, C. Niedermayer, T. Blasius, A. Golnik, E. Brücher, R. K. Kremer, D. R. Noakes, C. E. Stronach, and E. J. Ansaldo, Phys. Rev. B **59**, 14099 (1999).

[27] W. A. Fertig, D. C. Johnston, L. E. DeLong, R. W. McCallum, M. B. Maple, and B. T. Matthias, Phys. Rev. Lett. **38**, 987 (1977).

[28] J. Lynn, D. Moncton, W. Thomlinson, G. Shirane, and R. Shelton, Solid State Communications **26**, 493 (1978).

[29] S. Saxena, P. Agarwal, K. Ahilan, F. Grosche, R. Haselwimmer, M. Steiner, E. Pugh, I. Walker, S. Julian, P. Monthoux, et al., Nature **406**, 587 (2000).

[30] D. Aoki, A. Huxley, E. Ressouche, D. Braithwaite, J. Flouquet, J.-P. Brison, E. Lhotel, and C. Paulsen, Nature **413**, 613 (2001).

[31] N. Huy, A. Gasparini, D. De Nijs, Y. Huang, J. Klaasse, T. Gortenmulder, A. de Visser, A. Hamann, T. Görlach, and H. v. Löhneysen, Phys. Rev. Lett. **99**, 067006 (2007).

[32] T. Hattori, Y. Ihara, Y. Nakai, K. Ishida, Y. Tada, S. Fujimoto, N. Kawakami, E. Osaki, K. Deguchi, N. Sato, et al., Phys. Rev. Lett. **108**, 066403 (2012).

[33] T. Ohta, T. Hattori, K. Ishida, Y. Nakai, E. Osaki, K. Deguchi, N. K. Sato, and I. Satoh, J. Phys. Soc. Jpn. **79**, 023707 (2010).

[34] A. de Visser, N. T. Huy, A. Gasparini, D. E. de Nijs, D. Andreica, C. Baines, and A. Amato, Phys. Rev. Lett. **102**, 167003 (2009).

[35] H. Kotegawa, A. Harada, S. Kawasaki, Y. Kawasaki, Y. Kitaoka, Y. Haga, E. Yamamoto, Y. Onuki, K. M. Itoh, E. Haller, et al., J. Phys. Soc. Jpn. **74**, 705 (2005).

[36] I. Sheikin, A. Huxley, D. Braithwaite, J. P. Brison, S. Watanabe, K. Miyake, and J. Flouquet, Phys. Rev. B **64**, 220503 (2001).

[37] D. Aoki, T. D. Matsuda, V. Taufour, E. Hassinger, G. Knebel, and J. Flouquet, J. Phys. Soc. Jpn. **78**, 113709 (2009).

[38] F. Lévy, I. Sheikin, B. Grenier, C. Marcenat, and A. Huxley, J. Phys.: Condens. Matter **21**, 164211 (2009).

[39] Y. Tokunaga, D. Aoki, H. Mayaffre, S. Krämer, M.-H. Julien, C. Berthier, M. Horvatić, H. Sakai, S. Kambe, and S. Araki, Phys. Rev. Lett. **114**, 216401 (2015).

[40] V. Taufour, A. Villaume, D. Aoki, G. Knebel, and J. Flouquet, J. Phys. Conf. Ser. **273**, 012017 (2011).

[41] D. Aoki and J. Flouquet, J. Phys. Soc. Jpn. **83**, 061011 (2014).

[42] A. Gourgout, A. Pourret, G. Knebel, D. Aoki, G. Seyfarth, and J. Flouquet, Phys. Rev. Lett. **117**, 046401 (2016).

[43] H. Kotegawa, K. Fukumoto, T. Toyama, H. Tou, H. Harima, A. Harada, Y. Kitaoka, Y. Haga, E. Yamamoto, Y. Ōnuki, et al., J. Phys. Soc. Jpn. **84**, 054710 (2015).

[44] T. Sakakibara, H. Mitamura, T. Tayama, and H. Amitsuka, Jpn. J. Appl. Phys. **33**, 5067 (1994).

[45] NINS, National Astronomical Observatory of Japan, ed., *Chronological Scientific Tables* (MARUZEN, Tokyo, Japan, 2016), http://www.rikanenpyo.jp/, [in Japanese].

[46] Y. Kono, Ph.D. thesis, The University of Tokyo, Tokyo, Japan (2017).

[47] Scientific Instruments, Inc., http://www.scientificinstruments.com/product-detail/model-ro-6001k-ruthenium-oxide-rtd/, (December 2017).

[48] S. Kittaka, *Textbook of J-Physics Summer School* (J-Physics: Physics of Conductive Multipole Systems, Koyasan Univ., Japan, 2016), p. 67, [unpublished, in Japanese].

[49] S. Yonezawa, T. Kajikawa, and Y. Maeno, Phys. Rev. Lett. **110**, 077003 (2013), Supplemental Material.

[50] KOA, Inc., https://www.koaglobal.com/~/media/Files/KOA/product/catalogs/rk73b.ashx, (December 2017).

[51] ENTROPY, Inc., http://www.rockgateco.com/product/ruox_tempsensor/, (Web page of ROCKGATE, Inc., December 2017).

[52] Attocube, Inc., http://www.attocube.com/attomotion/premium-line/angt101/, (December 2017).

[53] A. Kasahara, Master's thesis, The University of Tokyo, Tokyo, Japan (2015), [in Japanese].

[54] S. Kittaka, A. Kasahara, T. Sakakibara, D. Shibata, S. Yonezawa, Y. Maeno, K. Tenya, and K. Machida, Phys. Rev. B **90**, 220502 (2014), Supplemental Material.

[55] M. Besnus, J. Kappler, P. Lehmann, and A. Meyer, Solid State Communications **55**, 779 (1985), ISSN 0038-1098.

[56] P. Haen, J. Flouquet, F. Lapierre, P. Lejay, J.-M. Mignot, A. Ponchet, and J. Voiron, Journal of Magnetism and Magnetic Materials **63-64**, 320 (1987), ISSN 0304-8853.

[57] C. Paulsen, A. Lacerda, L. Puech, P. Haen, P. Lejay, J. L. Tholence, J. Flouquet, and A. de Visser, Journal of Low Temperature Physics **81**, 317 (1990).

[58] G. Bruls, D. Weber, B. Lüthi, J. Flouquet, and P. Lejay, Phys. Rev. B **42**, 4329 (1990).

[59] S. Holtmeier, P. Haen, A. de Visser, A. Lacerda, P. Lejay, and J. Flouquet, Physica B: Condensed Matter **186-188**, 521 (1993), ISSN 0921-4526.

[60] S. Holtmeier, P. Haen, A. Lacerda, P. Lejay, J. Tholence, J. Voiron, and J. Flouquet, Physica B: Condensed Matter **204**, 250 (1995), ISSN 0921-4526.

[61] H. Aoki, S. Uji, A. K. Albessard, and Y. Ōnuki, J. Phys. Soc. Jpn. **62**, 3157 (1993).

[62] H. Aoki, S. Uji, A. K. Albessard, and Y. Ōnuki, Phys. Rev. Lett. **71**, 2110 (1993).

[63] S. Julian, F. Tautz, G. McMullan, and G. Lonzarich, Physica B: Condensed Matter **199-200**, 63 (1994), ISSN 0921-4526.

[64] L. P. Regnault, W. A. C. Erkelens, J. Rossat-Mignod, P. Lejay, and J. Flouquet, Phys. Rev. B **38**, 4481 (1988).

[65] H. Kadowaki, M. Sato, and S. Kawarazaki, Phys. Rev. Lett. **92**, 097204 (2004).

[66] T. Sakakibara, T. Tayama, K. Matsuhira, H. Mitamura, H. Amitsuka, K. Maezawa, and Y. Ōnuki, Phys. Rev. B **51**, 12030 (1995).

[67] S. Nakamura, T. Sakakibara, Y. Shimizu, S. Kittaka, Y. Kono, Y. Haga, J. c. v. Pospíšil, and E. Yamamoto, Phys. Rev. B **96**, 094411 (2017).

[68] F. Lévy, I. Sheikin, B. Grenier, and A. D. Huxley, Science **309**, 1343 (2005).

[69] F. Hardy, D. Aoki, C. Meingast, P. Schweiss, P. Burger, H. v. Löhneysen, and J. Flouquet, Phys. Rev. B **83**, 195107 (2011).

[70] V. Tran, R. Tro, and G. Andr, J. Magn. Magn. Mater. **186**, 81 (1998).

[71] E. Yelland, J. Barraclough, W. Wang, K. Kamenev, and A. Huxley, Nat. Phys. **7**, 890 (2011).

[72] F. Lévy, I. Sheikin, and A. Huxley, Nat. Phys. **3**, 460 (2007).

[73] A. Miyake, D. Aoki, and J. Flouquet, J. Phys. Soc. Jpn. **77**, 094709 (2008).

[74] J. Pospíšil, Y. Haga, S. Kambe, Y. Tokunaga, N. Tateiwa, D. Aoki, F. Honda, A. Nakamura, Y. Homma, E. Yamamoto, et al., Phys. Rev. B **95**, 155138 (2017).

[75] D. Aoki, F. Hardy, A. Miyake, V. Taufour, T. D. Matsuda, and J. Flouquet, C. R. Physique **12**, 573 (2011).

[76] V. P. Mineev, Phys. Rev. B **91**, 014506 (2015).

Acknowledgments

First of all, I am deeply grateful to Prof. Sakakibara for his invaluable support and guidance of experiment, writing paper, and discussion of physics through the hard moments of graduate school. I am sure that his kind support is essential to my Ph. D study. I would like a maximum of gratitude for him.

I am grateful to Prof. Y. Uwatoko for insightful suggestions and kind support as the chief examiner of my dissertation. I sincerely thank Prof. M. Ogata, Prof. C. Furusawa, Prof. M. Tokunaga, and Prof. K. Kitagawa as sub-chief examiner for helpful comments and suggestions.

I would like to show my appreciation to all the collaborators of this work. I would like to thank Dr. J Pospíšil, Dr. Y. Haga and Dr. E. Yamamoto (Japan Atomic Energy Agency) for providing me with single crystal of URhGe. I sincerely appreciate Dr. Y. Shimizu (Tohoku University) for stimulating discussions in many aspects, and kind support for writing paper. I would also like to thank Prof. D. Aoki (Tohoku University) for valuable discussion about uranium-based ferromagnets.

I would like to offer my special thanks to the members of Sakakibara lab. I am deeply grateful to Dr. S. Kittaka for teaching experimental techniques of the specific heat and the magneto-caloric effect measurements, kind support for writing paper, and stimulating discussions in many aspects. I sincerely appreciate Ms. Y. Hisinuma and Ms. Pudding for clerical and moral supports. I woukd like to thank Dr. Y. Sun for valuable discussion. I would like to show my appreciation to Dr. Y. Kono for teaching experimental techniques of the magnetization measurements, kind support for how to use PC softwares, and invaluable discussions in many aspects. I would like to thank the former members of Sakakibara lab., Dr. H. Mitamura, Dr. N. Kase, Dr. Y. Shimura, and Mr. A. Kasahara for invaluable discussion and kind help. Including Prof. M. Yokoyama (Ibaraki University) and Dr. Y. Matsumoto (Toyama University), I greatly thank many people, who have visited Sakakibara lab. for joint reaserch program.

Lastly, I would like to greatly thank my parents for giving me a chance to study in doctor course.